university of groningen

Study of cosmic-ray composition with Imaging Atmospheric Cherenkov Telescopes

PhD thesis

to obtain the degree of PhD at the
University of Groningen
on the authority of the
Rector Magnificus Prof. J.M.A. Scherpen
and in accordance with
the decision by the College of Deans

and

to obtain the degree of PhD at the
University of São Paulo
on the authority of the
Rector Magnificus Prof. Dr. Carlos Gilberto Carlotti Jr.
and in accordance with
the decision by the College of Deans.

Double PhD degree

This thesis will be defended in public on

Tuesday 23 January 2024 at 14.30 hours

by

Andres Gabriel Delgado Giler

born on 17 June 1993
in Guayaquil, Ecuador

Supervisors
Prof. L. V. de Souza
Prof. R. F. Peletier

Examining Committee
Prof. R. M. Mendez
Prof. C. W. J. P. Timmermans
Prof. C. van Eldik
Prof. E. Moura Santos
Prof. F. F. S. van der Tak
Prof. K. Egberts
Prof. R. Nemmen da Silva
Prof. L. V. E. Koopmans

UNIVERSIDADE DE SÃO PAULO
INSTITUTO DE FÍSICA DE SÃO CARLOS

Andres Gabriel Delgado Giler

Study of cosmic-ray composition with Imaging Atmospheric Cherenkov Telescopes

Thesis presented to the Graduate Program in Physics at the Instituto de Física de São Carlos, Universidade de São Paulo, Brazil and Institute of Physics, University of Groningen, The Netherlands to obtain the double degree of Doctor of Science.

Concentration area: Theoretical and Experimental Physics

Supervisors:

Prof. Dr. Luiz Vitor de Souza Filho

Prof. Dr. Reynier Peletier

Original Version

São Carlos

2023

Giler, Andres Gabriel Delgado

Study of cosmic-ray composition with Imaging Atmospheric Cherenkov Telescopes / Andres Gabriel Delgado Giler; advisor Luiz Vitor de Souza Filho; Reynier F. Peletier. - São Carlos/ Groningen, 2023.

187 p.

Thesis (Doctorate - Graduate Program in Theoretical and Experimental Physics) -- Instituto de Física de São Carlos, Universidade de São Paulo - Brasil University of Groningen/ The Netherlands, 2023.

1. Air Shower. 2. Imaging Atmospheric Cherenkov Telescope. 3. Shower maximum. 4. Convolutional neural network. 5. Machine learning. I. Souza Filho, Luiz Vitor de, advisor. II. Peletier, Reynier F., adv. III. Title.

FOLHA DE APROVAÇÃO

Andres Gabriel Delgado Giler

Tese apresentada ao Instituto de Física de São Carlos da Universidade de São Paulo para obtenção do título de Doutor em Ciências. Área de Concentração: Física Teórica e Experimental.

Aprovado (a) em: 23/01/2024

Comissão Julgadora

Dr(a).: Luitje Vincent Ewoud Koopmans

Instituição: (Rijksuniversiteit Groningen/Holanda)

Dr(a).: Edivaldo Moura Santos

Instituição: (IF/USP)

Dr(a).: Raúl Mariano Méndez

Instituição: (Rijksuniversiteit Groningen/Holanda)

Dr(a).: Rodrigo Nemmen da Silva

Instituição: (IAG/USP)

Dr(a).: Floris Frits Sebastiaan van der Tak

Instituição: (Rijksuniversiteit Groningen/Holanda)

Dr(a).: Charles Wilhelmus Johannes Petrus Timmermans

Instituição: (Radboud University Nijmegen/Holanda)

Dr(a).: Katrin Egberts

Instituição: (Universität Potsdam/Alemanha)

Dr(a).: Christopher van Eldik

Instituição: (Friedrich-Alexander-Universität/Alemanha)

We make our world significant
by the courage of our questions
and the depth of our answers.

Carl Sagan – *Cosmos*

Printed by: Ipskamp Printing on recycled paper

Contents

1. Introduction

1.1 Research intentions

Cosmic rays (CRs) are particles of non-terrestrial origin that reach the Earth. Although there are several questions in the study of these particles, there are two central topics of interest: What is their origin (production, acceleration, and propagation), and what is their importance in the total energy balance of the universe?

The difficulty in studying CRs lies in the fact that their flux drops many orders of magnitude for energies between 10^9 eV and 10^{20} eV. Therefore, the experimental techniques used for particle detection change significantly in this energy range. For energies lower than $\sim 10^{14}$ eV, the flux is high enough to directly measure the primary particles with spectrometers or calorimeters through balloons in the upper atmosphere or on satellites and space stations. For higher energies, the traditional technique is to take advantage of the interaction of cosmic primaries with the atmosphere.

When penetrating the atmosphere, CRs interact with the nuclei of atoms and initiate a cascade process called an *extensive air shower*. Several experimental techniques have been developed to measure different components of atmospheric showers. For energies between 10^9 eV and 10^{15} eV, one measurement technique is using *Imaging Atmospheric Cherenkov Telescopes (IACTs)* for the study of gamma-ray sources through the detection of gamma-initiated air showers. Each IACT can measure the Cherenkov light produced by the particles of an atmospheric shower. The signals measured in each IACT have to be reconstructed to extract from the measured information the properties of the primary cosmic particles. Data analysis is optimized to select gamma rays and study astrophysical sources by measuring the energy spectrum and mapping the emitting object. However, through the measurements of these telescopes, it is also possible to reconstruct fundamental information about the cosmic ray composition as a function of energy. To study the possibility of determining the type of primary particle using Cherenkov telescopes, this thesis proposes to:

P.1 CR mass identification by reconstructing the shower maximum X_{max} with novel methods using IACTs in the energy range from 1 TeV to 300 TeV.

P.2 Develop a convolutional neural network to separate proton-like and iron-like events in the energy range from 1 TeV to 300 TeV.

To achieve **P.1**, we presented two methods. The first method reconstructs a new mass-sensitive observable for telescopes located at distances $\geqslant 150$

m with respect to the shower impact on the ground and is explained in chapter 2. The second method reconstructs the shower profile of electrons and the depth of the shower maximum, considering telescopes at any distance from the shower axis, and is presented in chapter 3. For **P.2**, we reconstructed the longitudinal profiles of CR showers and separated the proton and iron based on the shower maximum, presented in chapter 4. In chapter 5, a deep learning algorithm that takes the image, the shower maximum, and the energy as inputs is shown and used to separate iron and proton events.

This chapter is structured as follows. In **Section** 1.2, an overview of the historical introduction of CR, the CR spectrum, and mass composition measurements are described. The overview of gamma-ray astronomy and the Imaging Atmospheric Cherenkov Telescopes, and in particular of the upcoming Cherenkov Telescope Array (CTA) observatory, which is one of the main focuses of this thesis, are given in **Section** 1.3. A description of the main methods and techniques used in air shower analysis is also included. In **Section** 1.4, the components and development of extensive air showers in the atmosphere are described. In **Section** 1.5, concepts and definitions of artificial neural networks are summarized. Finally, the thesis outline describing the subsequent chapters is presented in **Section** 1.6.

1.2 Overview of cosmic-rays

CRs are relativistic charged particles made up of protons, helium, electrons, and heavier charged nuclei, carrying enough energy to propagate from distant sources to Earth. These particles cover a vast energy range up to $\sim 10^{20}$ eV. The main problem in CR research is understanding the origin of these particles that lead to the acceleration to such high energies and the propagation through the galactic and extra-galactic environments. The fundamental quantities that help to address this problem are the spectrum, the arrival direction, and the mass composition. This chapter provides an overview of CR science as follows: Section 1.2.1 presents a historical perspective, describing the discovery of cosmic radiation and the evolution of experimental techniques; Section 1.2.2 summarises the measurements of CR spectrum and composition; Section 1.2.3 discusses the importance of the mass composition and section 1.2.4 describes some techniques to study the composition with ground-based observatories.

1.2.1 Historical introduction

In 1912, the radiation of cosmic origin was conclusively discovered by Victor Hess when he realized that the discharge speed of electroscopes mounted on atmospheric balloons increased with altitude (up to 5 km) [1, 2]. He explained this phenomenon with radiation of high penetrating power coming from outer space and entering the atmosphere. This discovery led to research on the origin and nature of this radiation. In 1913 and 1914, Kolhorster confirmed these measurements at 6 km and 9 km of altitude [3, 4, 5]. However, Millikan was initially not convinced about the evidence of such penetrating radiation, motivating him to carry out additional experiments [6]. Some doubts appeared in 1922, when Milikan and Bowen Ballons's flight indicated much less ionization above 5 km than Kolhorsters's observations, concluding that there was no cosmic radiation of the characteristics described in those results [7, 8]. But later, in 1925, Millikan and Cameron measured the ionization in snow-fed lakes to clear up the inconsistencies in measurements of the absorption coefficient of the cosmic radiation [9]. On this occasion, their results removed all doubts, indicating radiation travelling downwards with no local contamination, to which he referred with the name of *cosmic rays* (CRs). The noun *rays* was a misnomer because the nature of CR was not yet known.

Hereafter CRs opened the opportunity to discover new particles such as the positron, discovered by Anderson in 1933 using cloud chambers [10], the muon [11, 12] and the pion [13]. In the same year, Blacket also

reported tracks in cloud chambers, revealing traces of the electron-positron pair production [14].

A vital contribution came from Pierre Auger and his group in 1939. They found that sensors, separated by a maximum distance of 300 m, detected particle events simultaneously at sea level [15]. Their research revealed that these simultaneous events were related to the same primary particle of CRs. The conclusion was that a particle of CR induced an extensive air shower of secondaries in the upper atmosphere. They also concluded that the necessary energy for CR to produce these showers was at least of the order $\sim 10^{15}$ eV [15]. In this sense, a breakthrough was the work of John Linsley, who pioneered ground-based array detectors and was the first to detect an air shower initiated by a particle of 10^{20} eV [16]. This result extended the CR spectrum by several orders of magnitude including ultra-high energy cosmic rays (UHECR) [17].

Important implications in the physics of UHECR came with the discovery of Cosmic Microwave Background (CMB) radiation in 1965. Greisen [18] and independently Zatsepin and Kuzmin [19], predicted that protons with energies higher than 4×10^{19} eV would interact with CMB photons, producing pions. This phenomenon is known as the GZK effect. It was noted that the GZK effect would suppress the incoming CR flux at Earth even in scenarios where heavier nuclei dominate the flux. Initially, there was controversy about the results measured by the AGASA detector suggesting the absence of such suppression in the energy spectrum [20]. Later, evidence for a spectrum cutoff was presented by the Fly's Eye Observatory [21]. The debate created by both collaborations was an extra motivation for the construction of ground-based observatories such as the HiRes experiment [22] and the Pierre Auger Observatory [23], whose measurements resolved the controversy confirming the existence of the suppression.

Despite the controversy, the tension was a further incentive to create giant observatories with large collecting areas producing enough statistics, such as Telescope Array (which is about one-fourth of the area covered by the Pierre Auger Observatory) [24]. Both Pierre Auger and Telescope Array observatories allowed full sky coverage for UHECR measurements, taking advantage of previous technical developments in the surface and fluorescence technique. Nowadays, many advances have been made concerning UHECR. Studies about the mass composition have been performed [25, 26, 27, 28, 29] using the depth in which the shower reached the maximum number of particles, as will be discussed in detail later.

1.2.2 Spectrum and Composition

The energy spectrum of CRs, that is, the number of particles per unit area, unit time, solid angle, and unit energy, has been well studied up to around 10^{20} eV, as seen in Figure 1.1. The spectrum can be described using a power law that falls rapidly with the energy, dN/dE $\sim$ $E^{-\alpha}$, where α is the spectral index. There is a steepening from α=2.7 to α=3.0 at the so-called "knee" around 10^{15} eV. A second steepening occurs at about 5 $\times$ 10^{17} eV with α=3.3, which forms the second knee. Finally, the so-called "ankle" corresponds to the region above 5 $\times$ 10^{18} eV with a spectral index of α=2.7.

These changes in the energy spectrum are believed to carry essential information about the fundamental questions of the origin, acceleration and propagation of CRs. For energies below the knee (from 10^8 to 10^{15} eV), most CRs are believed to be originated from supernova remnants[1] inside our galaxy [30]. In this energy range, the detection of CR particles is performed directly by space-based experiments indicating a composition of 98% nuclei and 2% for electrons [31]. Of the cosmic ray nuclei, 87% are protons, 12% are helium nuclei and 1% for heavier nuclei. A tiny component is antimatter, such as positrons and antiprotons.

A possible explanation of the steepening of the spectrum is given by the effect of a magnetic field on the motion of the charged particles. The gyro-radius r_g of a charged particle of rigidity R[2] in a magnetic field of strength B (assuming particle velocity orthogonal to B) is [32]:

$$r_g = 1.1 \times 10^{-6} \frac{R(\mathrm{GV})}{B(\mu\mathrm{G})} \mathrm{pc}. \tag{1.1}$$

Assuming the magnetic field strength of our galaxy $\sim$ 3 μG [33] and protons of 10^{15} eV, the gyro-radius is $r_g \approx$ 0.37 pc. In the case of protons of 10^{18} eV, $r_g \approx$ 370 pc. Considering that our Galaxy has a radius of about 15 kpc and a thickness of $2h \approx$ 400 pc, we can conclude that particles up to 10^{15} eV are well confined within the Galaxy. On the other hand, CRs at higher energies start to escape more freely from the Galaxy, providing a possible reason for the steepening of the spectrum at the *knee*. Since the flux decreases with the energy, the detection of direct CRs particles is a challenging task. For energies larger than $\sim$ 10^{15} eV, CRs are detected

[1] A supernova is a catastrophic explosion that occurs at the end of the life of a massive star, emitting immense energy and ejecting heavy elements into space.

[2] The rigidity is defined as $R = pc/q$, where q is the particle charge, p is the particle momentum, and c is the speed of light. It can also be referred to as simply $R = Br_g$, where B is the magnetic field, r_g is the gyro-radius of the particle due to this field.

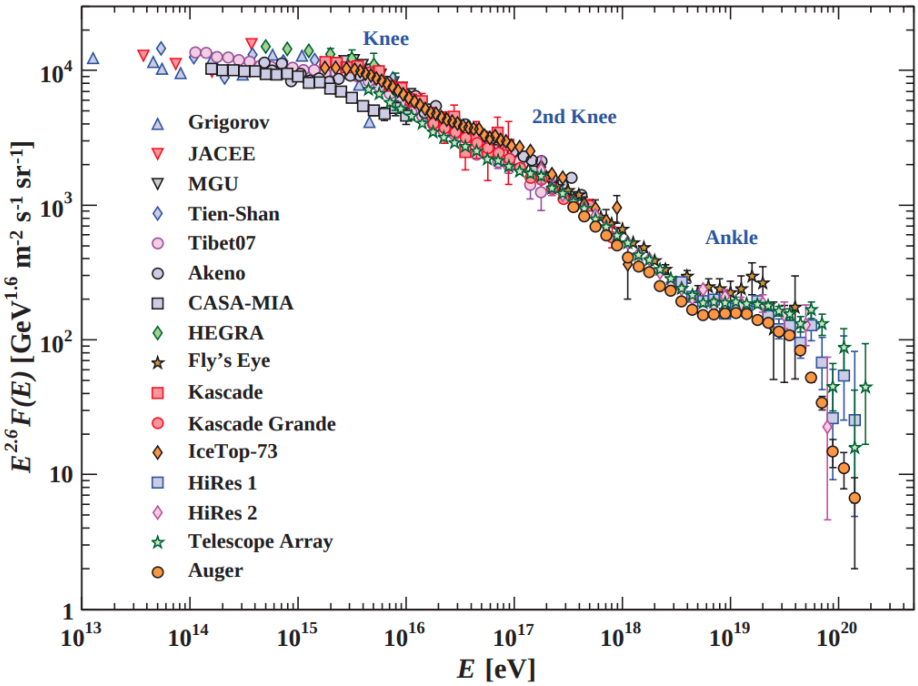

Figure 1.1: The all-particle spectrum of CRs as a function of energy, measured by several air shower experiments. The data points are scaled to visualize better the spectral index changes. Taken from reference [34].

indirectly by measuring secondary particles that reach the ground, using the so-called *extensive air shower*, which will be discussed in the following section.

1.2.3 Astrophysical models and mass composition importance

Some astrophysical explanations have been proposed for the CR flux depending on the energy regime. For instance, around the knee ($\sim$ PeV), there are (i) models linking the knee to the properties of CR sources and (ii) models linking the knee to the cosmic ray propagation [35]. In the first case, the models require two types of populations, one dominating the energies below the knee and another for energies above the knee. Different types of supernova sources would fulfil this requirement [36, 37]. In the second case, the knee could result from turbulent diffusion and drift in the Galatic magnetic field [38, 39]. Therefore, the precise measurement of the CR spectrum is an essential task for high-energy physics because it provides crucial information about their sources and propagation properties within

the Galaxy. For instance, additional softening in the CR proton spectrum could have consequences in studying the spectra of atmospheric neutrinos in the TeV energy range [40].

Fig. 1.2a shows that the CR proton flux (scaled by $E^{2.7}$) deviates from a simple power law and exhibits two features. The plot shows a hardening at around 1TeV, first discovered by PAMELA [41] and confirmed with high precision by AMS02 [42] and later by several other calorimeter detectors [43, 44, 45, 46, 47]. A second feature, a softening, is observed at about 10 TeV by direct measurements from DAMPE [46], with first hints provided earlier by CREAM [44] and NUCLEON [47] with lower precision. In addition, the CR proton spectra at high energies obtained by the ground-based KASKADE and IceTop/IceCube (indirect measurements) are not in good agreement, which means there is no unique way to extrapolate the flux at PeV energies (see Fig. 1.2b). The estimate of the proton flux performed by KASCADE and IceTop differs by a factor larger than three at around 2 PeV. These discrepancies do not allow us to establish whether additional spectral features exist. Future air shower observatories with capabilities for measuring many components (Cherenkov light, electromagnetic) of the shower (such as CTA [48]) will have the potential to reduce uncertainties in the spectra measurement for different primary particles.

In air shower analysis, a helpful quantity to describe the CR mass composition above 1 PeV is the mean logarithm mass given by [49]:

$$\langle \ln A \rangle = \sum_i f_i \ln A_i, \tag{1.2}$$

where f_i is the relative fraction of nuclei of mass A_i. Multiple experiments release observable quantities from which the average logarithmic mass can be derived. The typical observable is the average *depth of the shower maximum (X_{max})*, using Cherenkov and fluorescence light detected by air shower arrays. This is a unique study of the Pierre Auger Collaboration [50] in which the moments of ln A distributions are performed from the conversion of the moments of X_{max} distributions. These quantities are illustrated in Fig 1.3 for three different interaction models. Depending on the interaction model, the ln A values vary from 0 (pure composition of protons) to ~ 4 (pure composition of irons), indicating that composition goes from light to heavy along the energy.

Measuring the mass composition is needed to test models of suppression in the full-particle spectrum around the knee and ankle because a change from heavier to lighter composition would be evidence of a transition from galactic to extra-galactic sources.

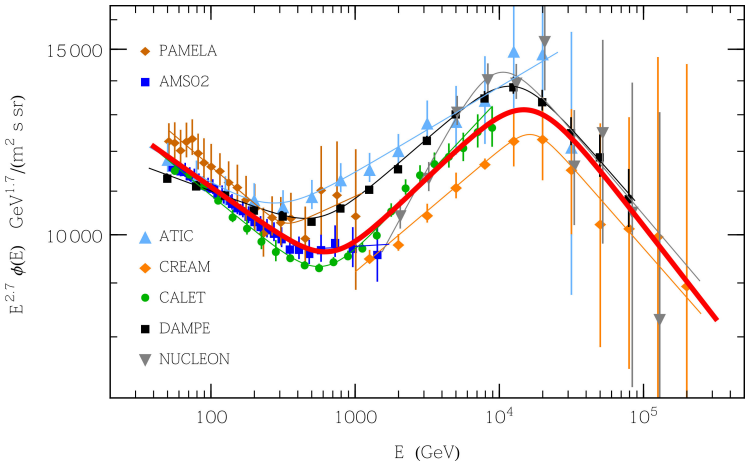

(a)

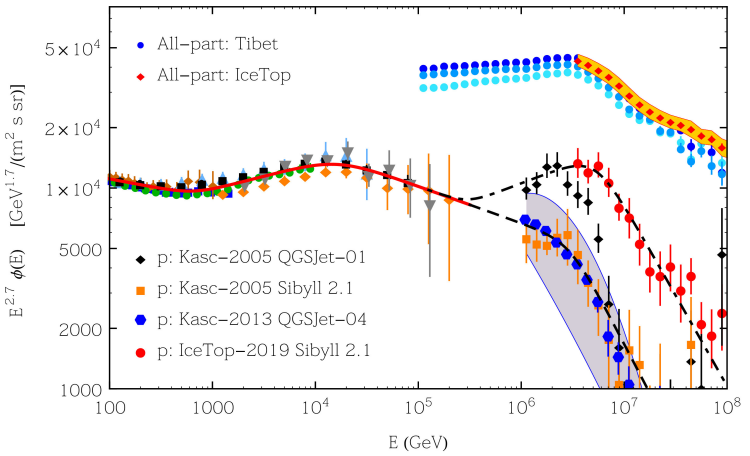

(b)

Figure 1.2: (a) Direct measurements of the CR proton spectrum from many experiments. (b) All–particle and proton spectra from direct measurements and air shower observations (KASKADE and IceTop). Images taken from [40]

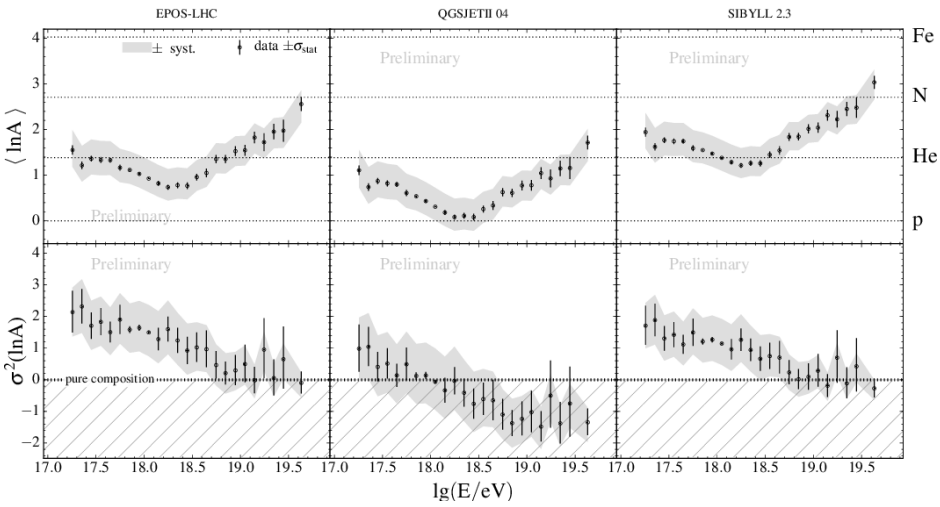

Figure 1.3: Moments of ln A distributions calculated from converting the moments of X_{max} distributions with EPOS-LHC, QGSJetII-04, Sibyll 2.3c. Image is taken from [50].

1.2.4 Measurements of the mass composition

In ground-based CR experiments, the energy E_0 and the mass A of a nucleus that originates an air shower are parameters we try to reconstruct because of the correlation with the accelerating astrophysical sources. Two independent observables must be measured to estimate the energy and mass of the CR that generated the air shower. The energy E is proportional to the shower size N_e, which is the total number of electrons measured at the detection level. Along with the shower size, the muon size and the depth of the shower maximum are usually reconstructed. It is difficult to determine the energy and mass on a shower-to-shower basis because of fluctuations on X_{xmax} and N_μ at fixed N_e. These fluctuations come from experimental limitations and the stochastic nature of the interaction processes in the air shower, specifically related to the position of the first interaction.

1.2.4.1 Depth of the shower maximum

The depth of the shower maximum is the position (in g/cm^2) where the number of secondary particles reaches a maximum. For instance, in the Pierre Auger observatory, the X_{max} is obtained from the longitudinal deposit energy profile reconstructed from fluorescence telescopes. Fig. 1.4 shows simulated shower profiles superimposed on the measured profile.

One can see that even on a shower-to-shower basis, it is possible to make a rough distinction between light and heavy primaries by comparing the position of the X_{max}.

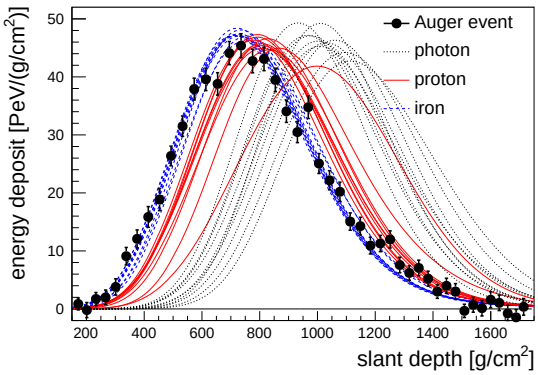

Figure 1.4: Data points of a longitudinal profile measured by fluorescence telescopes from Auger observatory. The data is compared with ten profiles from three different simulated air showers. Image is taken from [51].

The most relevant aspect of measuring the X_{max} is its relation with the CR composition because the average $\langle X_{max} \rangle$ and variance $\sigma^2(X_{max})$ of the shower maximum are sensitive [52, 51] to the distribution of the primary masses. Measuring mass composition is needed to test models of suppression in the full-particle spectrum around the knee and ankle because a change from heavier to lighter composition would be evidence of a transition from galactic to extragalactic sources. In a first approximation, a nucleus of mass A and energy E is equivalent to A protons with energy E/A. In principle, the average shower maximum for showers with similar energy offers a measure of how heavier or lighter the composition is in a given energy bin, as shown in Fig. 1.5. Measurements from several ground-based experiments indicate a change in composition, going from light to heavier for energies between 10^{15} eV and 10^{20} eV.

The average logarithm mass of CRs given in equation (1.2), $\langle \ln A \rangle = \sum f_i \ln A_i$, is used for CR experiments where elemental groups of mass A_i is adjusted with several flux fractions f_i. In the case of experiments that measured $\langle X_{max}^{data} \rangle$, the mean logarithm mass can be obtained from the average depth of shower maximum of protons X_{max}^{p} and iron nuclei X_{max}^{Fe} simulations using [49]:

$$\langle \ln A \rangle = \frac{\langle X_{max}^{p} \rangle - \langle X_{max}^{data} \rangle}{\langle X_{max}^{p} \rangle - \langle X_{max}^{Fe} \rangle} \times \ln A_{Fe}, \tag{1.3}$$

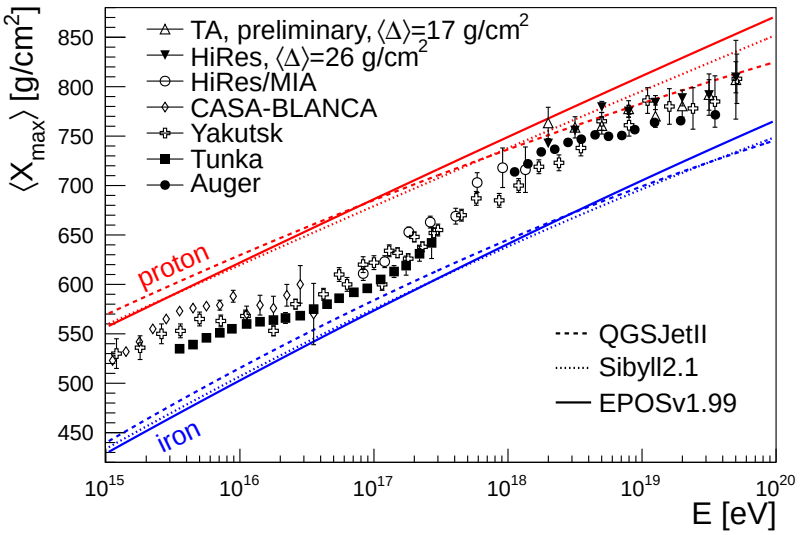

Figure 1.5: Measurements of X_{max} with non-imaging Cherenkov detectors (Tunka, Yakutsk, CASA-BLANCA) and fluorescence detectors (HiRes/MIA, HiRes, Pierre Auger and TA). Three different hadronic interaction models (QGSJET, Sybyll, EPOS) for the pure composition of proton and iron nuclei are shown. Image taken from [51].

where A_{Fe} is the mass of the iron. Some measurements of $\langle \ln A \rangle$ from the Pierre Auger Observatory are plotted in previous Fig. 1.3. As shown in Fig. 1.5, not many measurements have been performed below the PeV energy range using this analysis, which is an extra motivation for the future perspective of ground-based observatories.

1.2.4.2 Resolution of the reconstruction of the shower maximum

The reconstruction of the air shower parameters (primary energy, arrival direction, altitude/depth of the shower maximum) is essential in air shower array detectors. Mainly, the resolution in reconstructing the depth of the shower maximum is the first step before any analysis of CR composition or method based on the X_{max} [53, 54]. The validation consists of calculating the spread of the distributions between the simulated and the reconstructed values. In the case of fluorescence detectors for detecting ultra-high energy (from 10^{17} to 10^{20}) cosmic rays showers, typical values of X_{max} resolution are lower than 30 g/cm^2, reaching values of 12 g/cm^2, as seen in Table 1.1. In the case of the non-imaging Cherenkov detectors, the resolution is about 20 g/cm^2. At lower energies (around TeV), *Imaging Atmospheric*

Cherenkov Telescopes (IACTs) offer a resolution of about 30 g/cm^2.

Experiment	**Detection technique**	**Energy (eV)**	**Xmax resolution (g/cm^2)**
TA	Fluorescence light	$10^{18.4}$ - 10^{20}	17.2
HiRes	Fluorescence light	$> 10^{17}$	30.05
PAO	Fluorescence light	$10^{17.8}$ - 10^{20}	25 - 12
Yakutsk	Non-imaging Ch. det.	$\sim 10^{18}$	38
HESS	IAC technique	$> 10^{12}$	30
LOFAR	radio signal	$10^{16.8}$ - $10^{18.3}$	19

Table 1.1: Resolutions values in reconstructing the depth of shower maximum for different ground-based experiments and techniques. Values taken from Telescope Array (TA) [55], High Resolution Fly's Eye experiment (HiRes) [56], Pierre Auger Observatory (PAO) [53], Yakutsk [57], LOFAR [58].

1.2.5 Conclusion

This section provided an overview of CR research, focusing on detecting cosmic rays. Throughout history, we review the study of cosmic rays around the fundamental quest to understand the origin and nature of these particles. While precise measurements have yielded valuable insights into the energy spectrum, determining the composition of cosmic rays remains challenging. Unravelling their mass composition is crucial for constraining theoretical models of cosmic-ray acceleration and propagation. It is clear that estimating and analyzing mass composition measurements is not solely a technical limitation but is also constrained by interpreting observable quantities derived from air showers. In this sense, this thesis makes contributions in Chapters 2, 3, and 4, aiming to enhance the interpretation of X_{max} measurements and improve the reconstruction of this parameter. Given the crucial role of X_{max} in determining the mass composition of cosmic rays, the findings presented in this thesis ultimately contribute to resolving the challenge of determining cosmic ray mass composition.

1.3 Overview of gamma-ray astronomy

Gamma-ray astronomy detects and studies photons as they arrive at Earth from distant sources. The gamma-ray photons could have energies above $\sim$ 1 MeV and are classified depending on their energy domains (see Table 1.2). Gamma rays can be observed directly by space-based experiments such as the Fermi Gamma-ray Space Telescope for low and high-energy domains [59]. On the other hand, the detection of *Very High Energy (VHE)* and *Ultra High Energy (UHE)* gamma rays requires ground-based observatories performing indirect detection since the Earth's atmosphere is opaque to such high-energy radiation.

Since the atmosphere is not transparent to the gamma rays, they must be detected from satellites or indirectly using ground-based telescopes. Satellite detectors typically detect gamma rays with energies below a few hundred GeV and have an excellent γ/hadron separation. On the other hand, the flux of VHE sources is so low that the area available on satellite detectors does not allow to pile up a sufficient number of photons.

The *imaging atmospheric Cherenkov technique* based on the Cherenkov light emitted by the air shower initiated by the gamma rays is used to detect such low fluxes. Using arrays of telescopes provide several order of collection area larger than satellites. A disadvantage is that they are sensitive to contamination, such as CR-initiated showers or night sky backgrounds that limit the observation during clean moonless nights. In this sense, the present section is focused on reviewing aspects related to VHE gamma-ray astronomy with attention to experimental techniques rather than the astrophysical aspects.

Domain	Abreviation	**Energy Range**	
		min	max
Low energy	LE	1 MeV	30 MeV
High energy	HE	30 MeV	50 GeV
Very-high energy	VHE	50 GeV	100 TeV
Ultra-high energy	UHE	100 TeV	100 PeV
Extremely-high energy	EHE	$>$ 100 PeV	

Table 1.2: Energy domains in gamma-ray astronomy. Table modified from [60].

1.3.1 Historical introduction

Gamma-ray astronomy has been closely related to the history of cosmic rays. It was understood that cosmic rays, composed mostly of protons and a small fraction of heavier nuclei, could not be traced back to their sources due to the deflections by magnetic fields. By the early 1950s, several authors already suggested that cosmic ray electrons in the trapping field of a star would generate radio emission [61, 62]. These results gave support to previous studies that proposed supernovae as cosmic accelerators in the Galaxy [63]. In addition, it was believed that the interaction of CRs with interstellar gas and supernova would result in gamma-ray emission, motivating the development of space experiments to observe high-energy gamma rays from cosmic sources. In 1972, the OSO-3 satellite was the first to detect significant gamma-ray emission with energies above 50 MeV [64], revealing the existence of a galactic component concentrated around the galactic equator. From 1974 to 1991, more gamma-ray emissions collected by SAS-2 [65], COS B [66] and CGRO [67] were published. A big improvement in the sensitivity and field of view came with the AGILE satellite [68] launched in 2007, and the Large Area Telescope on the Fermi Gamma-Ray Space Telescope mission (Fermi-LAT) [69] launched in 2008. These two experiments detected several sources in the energy regime, from some MeV to many hundreds of GeV.

The extremely low gamma-ray flux at high energies required larger effective detector areas, which was possible to achieve with ground-based observatories through the imaging technique. The first idea came in 1948 with Blackett, who estimated that a fraction of 10^{-4} of the night-sky background corresponds to Cherenkov radiation produced by cosmic rays traversing the atmosphere [70]. Based on this effect, in 1953, Galbraith and Jelley proposed the detection of light Cherenkov pulses at the ground using photomultipliers, which revealed pulses of short duration correlated with the cosmic radiation [71].

The concept of a Cherenkov telescope with a small field of view occurs because Cherenkov light is emitted 1.5° around the shower axis, allowing the search of point-like sources. The Fred Lawrence Whipple Observatory at Mt. Hopkins in the USA, led by T. Weekes, was the first project to construct a ground-based telescope for detecting high energy gamma ray [72]. The observatory consisted of a 10-m reflector telescope with a single 12.5 cm photomultiplier at the focus, offering a field of view of 1° [73]. Over the period 1971 to 1972, many observations reported a 4 σ excess from the direction of the Crab Nebula.

By this time, Hillas had made essential contributions to the physics of air showers. He showed that each Cherenkov image of the Whipple telescope could be parameterized with an ellipse revealing the width, length, and orientation of the shower image. This method was used to distinguish between background hadronic showers and TeV gamma-ray showers from a point source [74]. After this, the imaging technique, based on the *Hillas parameters*, established ground-based gamma-ray astronomy. Nowadays, there are three stereoscopic systems fully operational: MAGIC (two telescopes), VERITAS (four telescopes), and HESS (five telescopes), shown in Fig 1.6.

The number of sources detected over the last 60 years is indicated in Fig. 1.7 for VHE gamma-rays with ground-based observatories (red), high-energy gamma rays with satellite instruments (blue), and X-rays sources (green). As can be seen, the number of sources went from 10 to more than 200 only in 20 years. Most VHE sources are located along the galactic plane, as shown in Fig. 1.8, which was possible by the 3rd generation of IACTs offering precise information about the spectrum and their morphology. With this current operation, the TeVCat [78, 79] lists 252 TeV gamma-ray sources as of June 2023.

The new era of gamma-ray astronomy includes a broad range of topics, such as the search for dark matter signals [80], measurement of extra-galactic background [81], and fundamental physics with gamma-ray propagation [82, 83]. In addition, developing methods for other studies, such as measuring cosmic ray flux and its mass composition, would offer the synergy between ground-based observatories and satellite experiments [84, 85]. To achieve these objectives, the new generation of observatories would provide better sensitivity than the current generation [86, 87]. In that sense, *The Cherenkov Telescope Array (CTA)* will lead the next generation of gamma-ray detections in the range from 30 GeV to 300 TeV using different sizes of telescopes.

1.3.2 The Imaging atmospheric Cherenkov technique

The direct detection of VHE γ-rays is impossible at the ground because of the atmosphere. Satellite experiments, used to direct detections outside the atmosphere, have an effective area A_{eff} of approximately some square meters. The differential particle rate, $\frac{dR}{dE}$, is related to the differential flux, $\frac{d\Phi}{dE}$, through

$$\frac{dR}{dE}(E) = \frac{d\Phi}{dE}(E) \times A_{eff}(E). \tag{1.4}$$

(a) MAGIC.

(b) HESS.

(c) VERITAS.

Figure 1.6: Current generation of observatories: (a) MAGIC [75], (b) HESS [76] and (c) VERITAS [77].

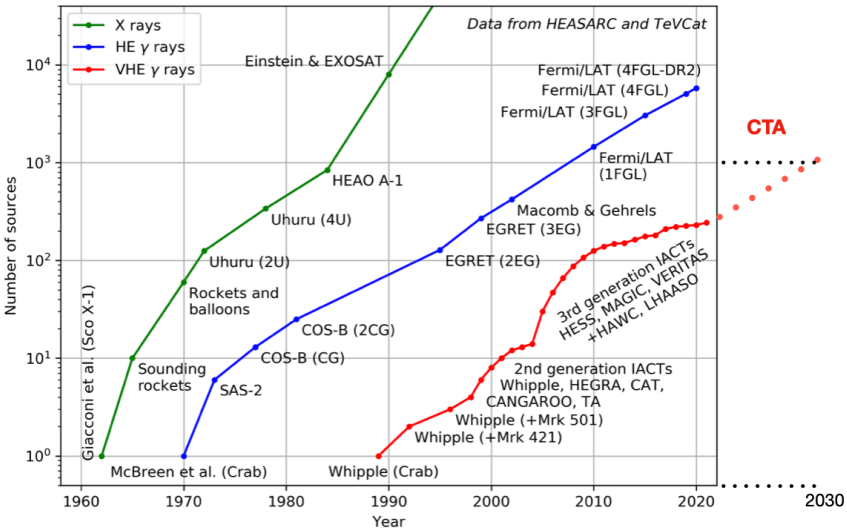

Figure 1.7: Kifune plot showing the number of sources detected over the years in X-ray, HE, and VHE gamma-rays. Image taken from [88].

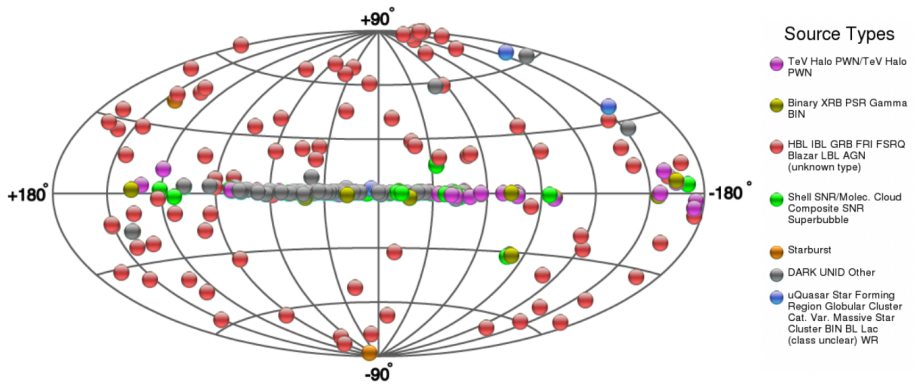

Figure 1.8: Sky map of VHE gamma-ray sources by ground-based observatories. Image taken from [88].

If the differential flux is small, the effective area should be big enough to have an acceptable particle rate in an acceptable time. Therefore, ground-based telescopes are necessary since they provide an effective area in the order of $> 10^5$ m. When the γ-ray hits the atmosphere, it creates a particle cascade. As a result, some of the particles generate Cherenkov light, which is detected by *Cherenkov telescopes* (CT), and the method is known as *imaging atmospheric Cherenkov technique*. The primary gamma rays can be detected using ground-based telescopes that collect the Cherenkov light emitted by the particles in the cascade.

The imaging of the Cherenkov light from the air shower is sketched in Fig. 1.9. The shower initially grows in size as it penetrates deep in the atmosphere, reaches a maximum between 8 and 10 km altitude, and then decreases, losing all its energy. As the air shower emits Cherenkov light, the emitted photons reach unique positions in the camera in order to form the image. Therefore, the form of the image is the result of the charged particle distribution, which is different from shower to shower and depends on the primary particle energy and type. Gamma-ray events produce images of approximately elliptical shapes, while most hadron events produce irregular and asymmetric shapes in the camera, as illustrated in Fig. 1.10.

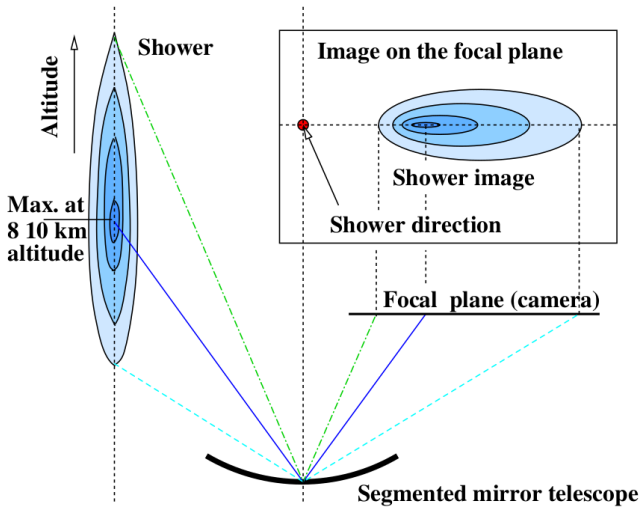

Figure 1.9: Distribution of Cherenkov light in the camera. [89]

The topology of a shower image is a consequence of the distribution of charged particles, which varies from shower to shower and depends on the properties of the primary particle. Notably, images from gamma-ray showers differ from hadronic showers, as illustrated in Fig 1.10. Notably, the gamma-induced shower is elliptical, which reflects symmetry around

the shower axis, contrary to hadron-induced showers, which produce erratic patterns in the camera.

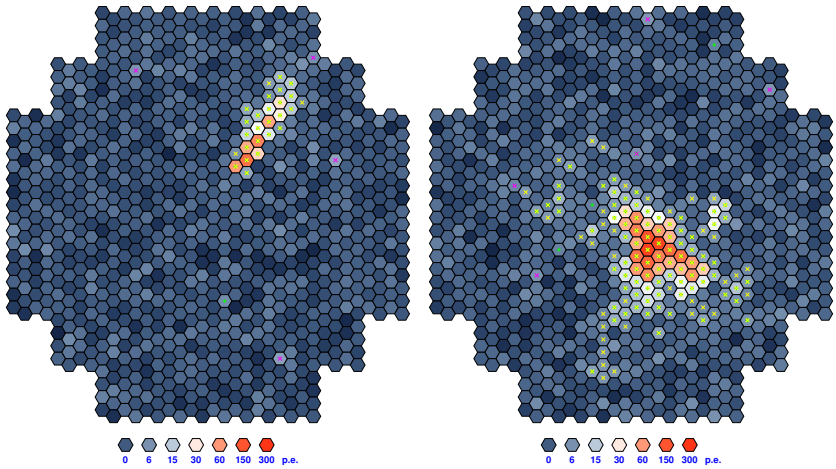

1.0 TeV gamma shower 2.6 TeV proton shower

Figure 1.10: Difference between the images of gamma-induced and hadron-induced showers in a simulated IACT camera. Image taken from [89]

1.3.3 Methods for air shower reconstruction

The most crucial goal of studying air showers is reconstructing the primary particle energy, arrival direction, and mass (for CRs). Different techniques are used to solve these tasks depending on the type of air shower experiment. While in CRs ground-based observatories, the particle identification is estimated by measuring the depth of the shower maximum, in γ ray astronomy, the traditional methods are based on the parametrization of the shower image with an ellipse. The state-of-the-art of current techniques is also based on deep learning algorithms, which are used to improve mainly the gamma/hadron separation [90, 91, 92, 93, 94] and will be discussed later.

There are three traditional techniques in gamma rays analysis: Hillas parameter-based analysis, Model analysis, and 3D model analysis. The model analysis is a more elaborated analysis technique based on the image pixel-wise fit. It is based on a pixel-per-pixel comparison of camera pixel amplitudes with an expected image template. The reconstruction uses a maximum likelihood fit to find the best-fit shower parameters [95]. The 3D model analysis [96] is a kind of 3-dimensional generalization of the Hillas-parameter-based analysis.

1.3.3.1 Hillas-parameter based analysis

In 1985 [97] M Hillas proposed an analysis method to distinguish between hadronic showers (background) and gamma-ray showers in the TeV energy range. This method relies on the fact that gamma-ray shower images in the camera focal plane are in a good approximation of elliptical shape. Then, by modelling the shower footprint by an ellipse, it is possible to obtain the following parameters:

- *Lenght* and *width* of the ellipse,
- *size* as the total image amplitude,
- *distance d*: angular distance between the centre of the camera and the centre of the image,
- Φ: angle between the line connecting the centre of the ellipse with the centre of the camera and the x-axis,
- Ψ: angle between the ellipse's major axis and the x-axis.

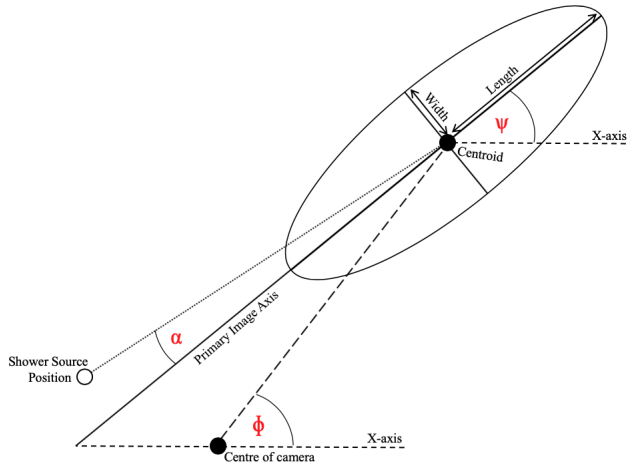

Figure 1.11: Geometrical definition of the Hillas parameters. Image taken from [98].

There are two types of reconstruction: single and stereoscopic reconstruction. In the single telescope approach, the shower direction is estimated mainly using length and size parameters, either with lookup tables or analytical functions [99]. The shower energy is estimated using the shower *size* and the angular distance *d*. On the other hand, the stereoscopic approach provides a geometric reconstruction of the shower. The intersection of the main axis of the shower image gives the shower direction and the shower impact. The shower energy is calculated from the weighted average of the individual telescopes. The Hillas parameters can

also provide a way to discriminate between candidate gamma-ray events and numerous background hadrons (for example, based on the length and width distribution cuts).

A more elaborated analysis technique is based on the image pixel-wise fit. This method is based on a pixel-per-pixel comparison of camera pixel amplitudes with an expected image template. The reconstruction uses a maximum likelihood fit to find the best-fit shower parameters [95]. A third technique, 3D model analysis [96], is a kind of 3-dimensional generalization of the Hillas-parameter-based analysis.

1.3.3.2 Model analysis

The *Model analysis* was introduced by the CAT collaboration [100] and improved by the HESS collaboration [95]. It is based on an image pixel-wise comparison between the actual camera image with an expected image template. They simulate a full set of image templates for the range of possible shower parameters. The expected and measured images are compared based on a maximum likelihood function. The likelihood function of observing a signal S in a given pixel, given an expected amplitude μ, a width of the pedestal σ_p (is the charge distribution from night sky background light and electronic noise) and the width of the single photo-electron distribution σ_s is given by:

$$P(S|\mu,\sigma_p,\sigma_s) = \sum_{n=0}^{\infty} \frac{e^{-\mu}\mu^n}{n!\sqrt{2\pi(\sigma_p^2+n\sigma_s^2)}} \exp\left(-\frac{(S-n)^2}{2(\sigma_p^2+n\sigma_s^2)}\right) \quad (1.5)$$

The log-likelihood function $\ln L = 2\sum_{pixel_i} \ln\left(P_i(S_i|\mu,\sigma_p,\sigma_s)\right)$ is maximized to obtain primary energy, direction, shower impact, and shower maximum.

1.3.3.3 3D-Model Analysis

The *3D-Model Analysis* is a 2-dimensional generalization of the Hillas-based analysis. The shower is modelled as a Gaussian sphere around the maximum in the atmosphere, which is used to predict the Cherenkov light measured in the camera. This model also assumes that the angular distribution of the Cherenkov photons is independent of the position of the emission point and the energy of the primary gamma rays. The 3D model gives the expected number of Cherenkov photons q_{th} detected by a given pixel of a given telescope as a function of the following shower parameters: direction, shower impact, shower maximum, 3D length and width of the

Gaussian distribution, and the total number of Cherenkov photons emitted by the shower. For a given pixel, the probability of measuring a charge q_{th} with fixed parameters q and σ is given by [96]:

$$P(q_{th}|q,\sigma) = \sum_{n=0}^{\infty} \frac{q_{th}^{n} e^{-q_{th}}}{n!\sqrt{2\pi\sigma}} \exp\left(\frac{(q-n)^2}{2\sigma^2}\right) \tag{1.6}$$

The likelihood function for an event takes the form $L = \prod_i P_i(q_{th}^i|q,\sigma)$, where the product is taken over all the triggered pixels of the images produced by a given shower.

1.3.4 The Cherenkov Telescope Array

The Cherenkov Telescope Array (CTA) is an international project that aims to be the next-generation ground-based observatory for gamma-ray astronomy from 30 GeV to 300 TeV. CTA will be located in two sites: one in the Southern hemisphere in Paranal Chile and another in La Palma, Spain in the North hemisphere [48]. With several tens of telescopes, CTA will provide better sensitivity for an extended field of view than the current generation. The arrays will be composed of three types of telescopes illustrated in Fig. 1.12:

- *Large Size Telescope (LST)*: They will have a 23 m diameter reflector with a 27.8 m f focal length. Its design is optimized for the lowest energy band.
- *Medium Size Telescope (MST)*: These telescopes are optimized to improve the sensitivity in the medium energy band. They will have 12 m reflectors and a 17m focal length.
- *Small Size Telescope (SST):* Their purpose is to extend the collection area of the array to capture the gamma rays at the highest energies. They will be located only in the Southern hemisphere.

1.3.4.1 CTA key characteristics and capabilities

The objective of CTA is to establish an observatory consisting of arrays of IACTs in two locations, with the aim of:

- **Improve the sensitivity** of current instruments by an order of magnitude at 1 TeV. Fig. 1.13 illustrates the notable increase in flux sensitivity compared to existing observatories.

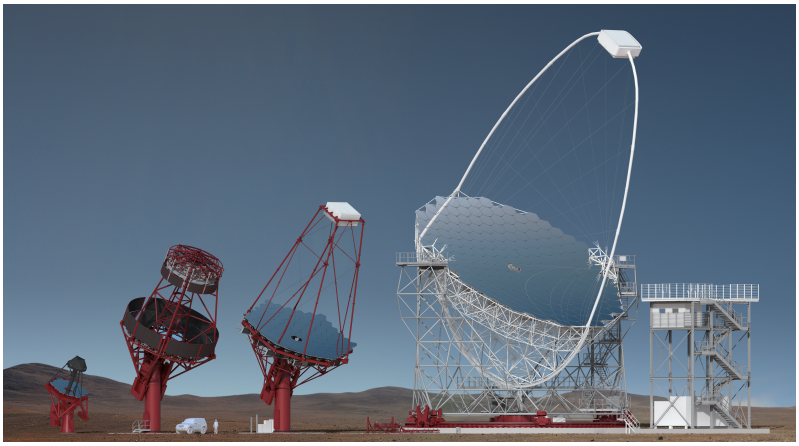

Figure 1.12: CTA telescope types: SST (left), two different MST structures, and LST (right). The figure is taken from [101].

- **Increase the detection area**, resulting in a higher photon rate and enabling the observation of phenomena occurring on the shortest timescales.

- **Achieve a significant enhancement in angular resolution and field of view**, thereby improving its capability to image extended sources with greater precision.

- **Achieve energy coverage** spanning from 20 GeV to a minimum of 300 TeV. This extensive energy range will enable CTA to explore high-redshift phenomena and study extreme particle accelerators in the universe.

- **Substantial enhancement in surveying capability, monitoring capability, and operational flexibility**. This will enable CTA to observe objects in multiple fields simultaneously, expanding its observational scope and efficiency.

- **Open observatory** for a broad user community by providing accessible data products and user-friendly tools suitable for non-expert users. This approach ensures diverse researchers can effectively utilize CTA data and contribute to scientific discoveries.

- **Offer full-sky coverage** through its two observatory sites in the southern and northern hemispheres.

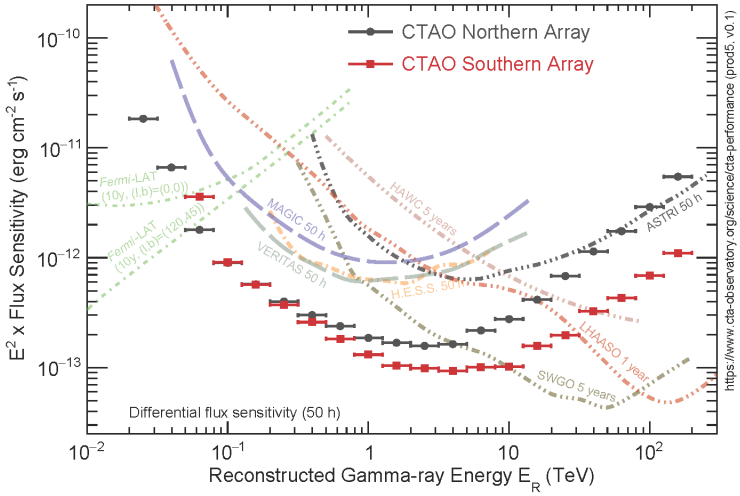

Figure 1.13: The expected differential sensitivity curves for the Alpha Configuration of CTA-South and CTA-North, obtained from 50 hours of observation time, are compared to the sensitivity of current observatories [102].

1.3.4.2 CTA science

The primary scientific questions and subjects addressed by CTA are focused on three themes [48]:

Understanding the Origin and Role of Relativistic Cosmic Particles: Relativistic particles are crucial in various astrophysical systems, such as pulsars, supernova remnants, active galactic nuclei, and galaxy clusters. CTA will provide the first high angular resolution measurements of cosmic-ray protons and nuclei, offering valuable insights into the processes of acceleration, transport, and the cosmic ray-mode feedback mechanisms in these systems.

Probing Extreme Environments: Particle acceleration to extremely high energies is typically associated with extreme astrophysical environments like neutron stars and black holes. VHE emission from these accelerated particles is a valuable tool to probe these environments, allowing access to time and distance scales beyond the reach of other wavebands. By observing gamma-gamma pair production signatures, CTA will enable measurements of the UV-IR background's redshift evolution, revealing the universe's star-formation history and investigating magnetic fields in

cosmic voids at significantly lower values than other methods. CTA will also investigate whether VHE photons heat the gas in these under-dense regions, potentially suppressing the formation of dwarf satellite galaxies. The three key areas within this theme are black holes and jets, neutron stars and relativistic outflows, and cosmic voids.

Exploring Frontiers in Physics: CTA offers a vast potential for significant discoveries in fundamental physics. It will explore the thermal relic cross-section for self-annihilating dark matter over a wide range of masses, including those beyond the reach of the Large Hadron Collider (LHC). With the combination of long travel times and short wavelengths, gamma rays from extragalactic sources serve as a sensitive probe for variations in the speed of light at different energies, potentially originating from quantum-gravity-induced fluctuations. CTA's sensitivity allows it to detect these effects on the Planck scale, representing a substantial discovery. Additionally, on their cosmic journey, gamma rays may interact with axion-like particles (ALPs) under the influence of intergalactic magnetic fields, leading to photon-ALP oscillations. Each of these phenomena would be a groundbreaking discovery in its own right, justifying the construction and operation of CTA. CTA's enhanced sensitivity and extended energy coverage bring these effects within reach, opening doors to further investigations in fundamental physics.

1.3.5 Conclusion

This section provided an overview of various aspects of very-high-energy gamma-ray astronomy. This field of study has advanced since ground-based detectors' first detection of a gamma-ray source in 1989. Over time, both the science itself and the instrumental techniques have advanced significantly. The current generation of Imaging Atmospheric Cherenkov Telescopes (IACTs) has reached a level of maturity, revealing the need for multiple sophisticated analysis techniques to explore their full potential. With the future Cherenkov Telescope Array (CTA) observatory and its complex structure, it is essential to focus on studies related to detecting and reconstructing extensive air showers using Cherenkov light. The results presented in this thesis are motivated by detecting Cherenkov light from air showers in IACT systems. Chapters 3 and 4 investigate the reconstruction of the longitudinal profile by using parametrized angular distributions of Cherenkov light in air showers. Chapter 5 explores the capabilities of IACTs in measuring the mass composition of cosmic rays using deep learning algorithms.

1.4 Extensive air showers

In 1939, Pierre Auger found that sensors, separated by a maximum distance of 300 m, detected particle events simultaneously at sea level [15]. His research revealed that these simultaneous events were related to the same primary particle of CRs.[3] The formation of an air shower is depicted in figure 1.14. When a photon or CR particle hits the atmosphere, it interacts with nuclei in the Earth's atmosphere (made of nitrogen, oxygen, and argon) at a typical height between 15 and 35 km, producing a shower of secondary particles such as electrons, positrons, muons, antimuons, gammas, hadrons, etc. The most abundant generated hadrons are neutral and charged pions. They form the hadronic shower component together with baryons and kaons. The photons from the neutral pion decay are the primary source of the electromagnetic (EM) component. Additionally, 90% of muons in the hadronic cascade are produced due to the decay of pions and kaons [103].

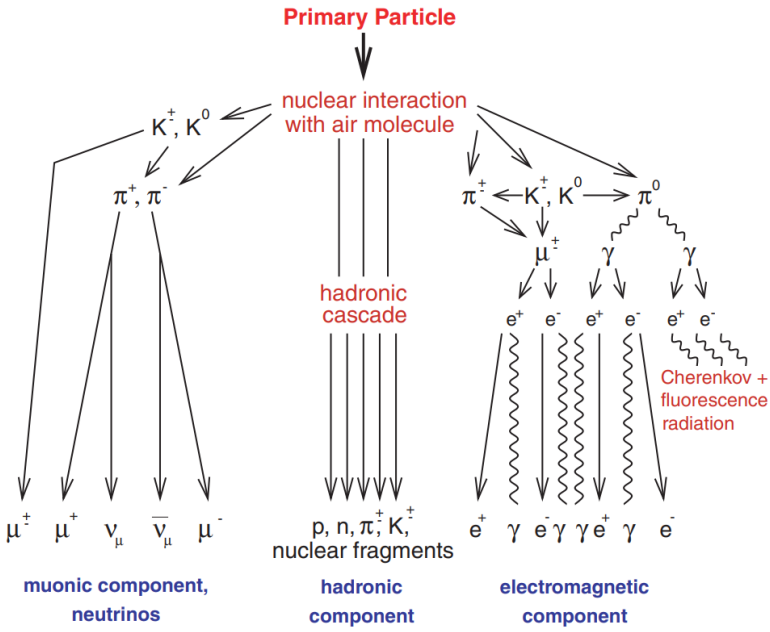

Figure 1.14: Formation of the air shower in the atmosphere, showing the different components. Taken from reference [104].

[3] Hereafter, the term *primary CR* will be considered the charged particle that arrives and hits the atmosphere.

Figure 1.15 shows the lateral (left) and the longitudinal (right) particle profiles of the different shower components for simulated events of 10^{19} eV. The lateral profile (left panel) represents the particle density as a function of the core distance. The curves indicate how the particle density of the different shower components decreases at large distances. The longitudinal profile (right panel) shows the atmospheric depth (in g/cm^2 as a function of the particle number. The different curves show that the region of the maximum is mainly determined by the $e^{\pm}$ and γ profiles. The shape and fluctuation of these profiles are due to the interaction mechanisms in *electromagnetic* and *hadronic cascades* discussed in the following sections.

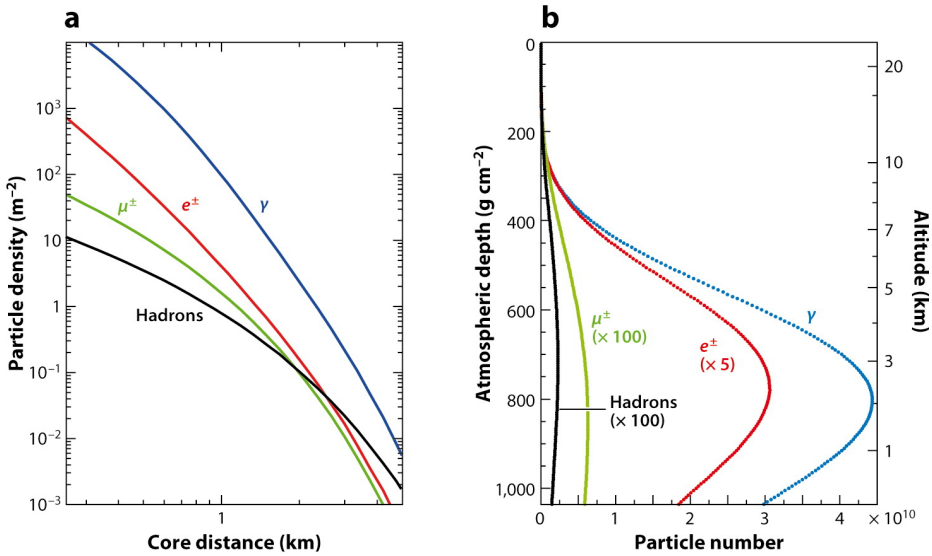

Figure 1.15: Average of the (a) lateral and (b) longitudinal shower profiles for simulated vertical proton showers of 10^{19} eV. The lateral profile of particles is measured at the detection level of 870 $\mathrm{g/cm^2}$. Taken from reference [103].

There are three main mechanisms by which a gamma ray can interact in the atmosphere: the photoelectric effect, the Compton effect, and pair production. Figure 1.16 shows the dependence of these attenuation coefficients on energy, with a predominance of the photoelectric effect for low energies, the Compton effect for medium energies, and the pair production for high energies. In the case of gamma rays with energies greater than GeV, the pair production effect dominates with a threshold energy of 1.02 MeV.

In the case of charged particles such as electrons, which pass through the atmosphere, there are two mechanisms of interest in energy loss:

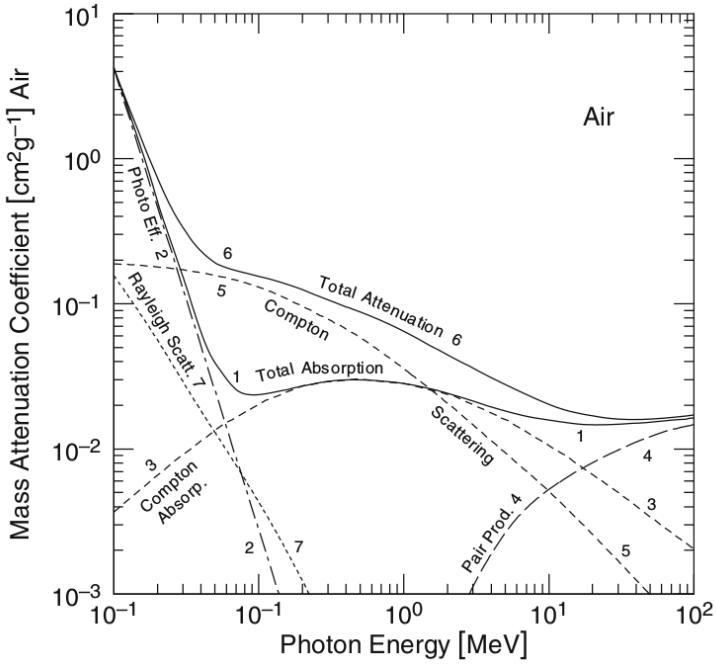

Figure 1.16: Mass attenuation coefficient for photons in air. Curve 1, labelled Total Absorption, is the sum of the linear coefficients for photoelectric absorption (curve 2), Compton absorption (curve 3), and pair production (curve 4). Adding the Compton scatter (curve 5) gives the Total Attenuation in curve 6. Other curves are shown as a complement. Taken from reference [105].

ionization and Bremsstrahlung. The losses by ionization refer to the Coulomb scattering of relativistic electrons from the atmospheric shower with the electrons in the medium. For low energy, an electron loses energy mainly by ionization. On the other hand, the main form of energy loss for energetic electrons is due to Bremsstrahlung because the intensity of this emission is inversely proportional to the square of the mass and proportional to the particle's energy. The energy at which the two losses are equal, ionization and Bremsstrahlung, is called *critical energy*. Then, the critical energy depends on the medium in which an electron propagates, being in the air at sea level $E_{crit} \approx 84$ MeV.

It is advantageous to define the radiation length X_0 (measured in g/cm^2) when the energy losses by radiation are dominant. The reason is that this magnitude represents the thickness traversed x in the medium by which the charged particle loses part of the initial energy E_0 by a factor e;

this is:

$$\frac{E(x)}{E_0} = e^{-\frac{x}{X_0}} \quad \Longrightarrow \quad \left(\frac{dE}{dx}\right)_{bremsstrahlung} = -\frac{E}{X_0}. \tag{1.7}$$

The expression relating Bremsstrahlung radiation length to pair production differs only by a factor:

$$X_{0,pair} = \left(\frac{9}{7}\right) X_{0,bremsstrahlung}, \tag{1.8}$$

which implies that, on average, a photon travels a longer path in a medium before creating an electron-positron pair than an electron does to experience bremsstrahlung. In general, a high-energy photon or electron that reaches the atmosphere will mainly experience interaction processes via pair production and bremsstrahlung. These processes create a cascade of secondary particles which define the electromagnetic component of the air shower.

1.4.1 Electromagnetic cascades

The simplest model for the development of atmospheric showers considers only the two fundamental processes already mentioned, pair production and bremsstrahlung, and is known as the *Heitler model* [106]. It is assumed that the radiation lengths for both processes are equal. Under the assumption that the particle is split in two for each unit radiation length λ_e (see Fig. 1.17a), the total number of particles N at depth X is

$$N(X) = 2^n \tag{1.9}$$

where $n = \frac{X}{\lambda_e}$ is the number of generations (i.e. consecutive iterations). The X_{max} is defined by the atmospheric depth where the maximum number of particles is reached, that is, when a $E = E_{crit}$, which leads to the following relation:

$$N_{max} = \frac{E_0}{E_{crit}}, \tag{1.10}$$

where the critical energy defines when the development of the shower stops. The previous equation can be solved for the X_{max}, giving the result:

$$X_{max}^{(EM)} \sim \lambda_e \ln\left(\frac{E_0}{E_{crit}}\right). \tag{1.11}$$

Therefore, the maximum number of particles is proportional to the primary particle's energy, and the shower's maximum depth grows logarithmically with the primary particle energy in the electromagnetic case.

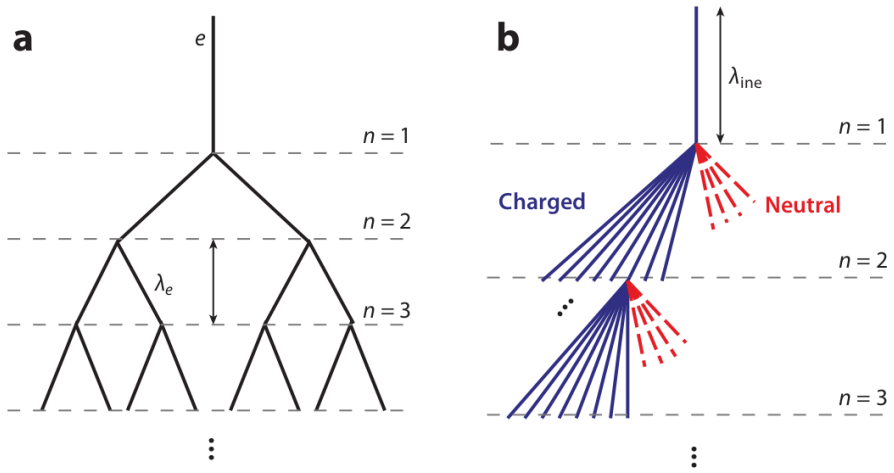

Figure 1.17: Shower model according to Heitler. (a) Electromagnetic case. (b) Hadronic case; dashed lines represent neutral particles (π^0) and solid lines represent charged particles ($\pi^{\pm}$). Only one interaction of a charged hadron is shown for each generation. Image taken from reference [103].

1.4.2 Hadronic cascades

The development of the hadronic shower is mainly determined by the hadron production and the decay of pions and muons as follows:

$$\begin{aligned} p + N &\longrightarrow p + N + n\pi^{\pm,0} + Q, \\ \pi^+ &\longrightarrow \mu^+ + \nu_\mu, \\ \pi^- &\longrightarrow \mu^- + \bar{\nu_\mu}, \\ \pi^0 &\longrightarrow \gamma + \gamma, \\ \mu^+ &\longrightarrow e^+ + \nu_e + \bar{\nu_\mu}, \\ \mu^- &\longrightarrow e^- + \bar{\nu_e} + \nu_\mu, \end{aligned} \tag{1.12}$$

where Q represents other hadrons. It is possible to see that neutral pions play a particular role in the development of cascades, making up a fraction of about 30% of all pions and instantly decaying into two photons. Muons are mainly produced in hadronic cascades and contribute about 10% on average to the total flux of particles at ground level in an atmospheric shower.

The characteristics of hadronic showers can be obtained by generalizing the Heitler model [107]. In this case, the interaction of a hadron with

energy E will produce n_{tot} new particles with energy E/n_{tot}, where two-thirds of which are charged particles n_{ch} (charged pions) and one-third of which are neutral particles (neutral pions). Neutral pions decay rapidly ($c\tau = 25$ nm) in two photons. After having travelled a distance corresponding to the interaction length λ_{ine}, the charged particles can interact again with the nuclei in the atmosphere. In the case of charged pions, they can decay ($c\tau = 7.8$ m), producing a muon particle per hadron. In each hadronic interaction, 1/3 of the energy is transferred to the electromagnetic component of the shower via decay of π^0. After n consecutive interactions, the energy of the hadronic and electromagnetic components is given respectively by:

$$E_{hadron} = \left(\frac{2}{3}\right)^n E_0 \quad , \quad E_{EM} = \left[1 - \left(\frac{2}{3}\right)^n\right] E_0. \tag{1.13}$$

At n $\approx$ 6, approximately 90% of the shower's initial energy is carried by electromagnetic particles and deposited as ionization energy in the atmosphere. Therefore, the electromagnetic particles determine the depth of the shower maximum in the cascade. Additionally, considering only the EM sub-showers produced in the first hadronic interaction, one can write the following:

$$\begin{aligned} X_{max}^{(hadronic)} &\approx \lambda_{ine} + X_{max}^{(EM)} \cdot \left(\frac{E_0}{2n_{tot}}\right) \\ &\sim \lambda_{ine} + X_0 \ln\left(\frac{E_0}{2n_{tot}E_{crit}}\right). \end{aligned} \tag{1.14}$$

The hadronic cascade can be seen as a superposition of electromagnetic sub-cascades, where the maximum number of electrons corresponds to the electromagnetic component with reduced energy. Hadronic cascades also spread laterally due to the transverse momentum of the secondary particles. Because of the large transverse momentum transfer, a hadronic cascade differs from an electromagnetic one. One form of radiation produced by air showers is the *Cherenkov light*.

1.4.3 Cherenkov light in air showers

Charged particles moving at relativistic speed through a dielectric medium generate a symmetrical polarization in the azimuthal plane but not along the motion axis [105]. As a result, a dipole field extends along the charged particle track. If a charged particle propagates in a medium with velocity v_p faster than the speed of light in that medium, the created dipole fields will

interfere under the Cherenkov emission angle θ defined by the following equation:

$$\cos(\theta) = \frac{1}{\beta\eta}, \tag{1.15}$$

where $\beta = v_p/c$ and η is the refraction index of the traversed medium. From equation 1.15 for a given η, there is a minimum velocity a charged particle must have in order to induce the Cherenkov emission in the medium, the threshold velocity $\beta_{th} = 1/\eta$. Moreover, for each medium, there is a specific maximum angle of emission θ_{max} when $\beta = 1$, i.e.:

$$\theta_{max} = 1/\arccos(\eta). \tag{1.16}$$

The threshold energy for the Cherenkov emission depends on the particle mass m_0 by:

$$E_{min} = \frac{m_0 c^2}{\sqrt{1-\eta^{-2}}}, \tag{1.17}$$

which means particles such as electrons and positrons have a lower threshold energy in the same medium compared to heavier particles. The air density changes continuously with height [105], as does the refractive index, and therefore, the threshold energy and emission angle depend on the altitude in the atmosphere. For instance, $E_{min}^{e^{\pm}}$ = 21.22 MeV ,$E_{min}^{\mu^{\pm}}$ = 4.38 GeV, $E_{min}^{p} \approx$ 39 GeV e $E_{min}^{Fe} \approx$ 1 TeV at sea level. The atmospheric density (and the index of refraction) increases as the altitude decreases. Assuming an isothermal atmosphere, one can use the barometric formula for air density to express the dependence on the altitude of the index of refraction:

$$\eta(h) = 1 + \eta_0\, e^{-h/h_0}, \quad \eta_0 = 0.00029 \ , \ h_0 = 7250 \text{ m}. \tag{1.18}$$

The emission angle θ_{max} as a function of altitude obtained from equations (1.15) and (1.18) is depicted in Fig. 1.18a. The Cherenkov light is emitted in a cone around the particle's path with an opening angle of $2\theta_{max}$. At the altitude H_0, this results in an approximately circular ring with a radius R given by

$$R = (h - H_0)\tan(\theta_{max}). \tag{1.19}$$

The change of the radius R with the emission altitude is shown in Fig. 1.18b. At the observation level, the light cones emitted by electrons

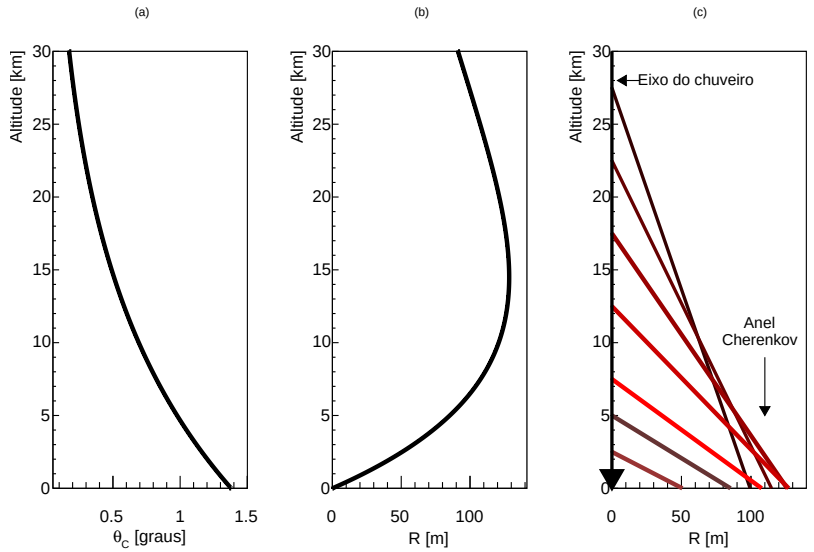

Figure 1.18: (a) Emission angle θ_C and (b) Cherenkov ring radius R as a function of emission altitude. Plot (c) clarifies the geometry of the Cherenkov light cone emitted at different altitudes. The observation level is at sea level.

and positrons at different altitudes overlap each other, resulting in an almost homogeneous distribution of light in a Cherenkov ring with a radius between 100 and 130 m (in the case of an electromagnetic shower [108]) around the axis of the shower head as shown in Figure 1.18c. The photons arrive in a period of a few nanoseconds. However, the light distribution contains scattered spots at the detection level due to multiple scattering for hadronic showers.

Figure 1.19 compares Cherenkov light distribution measured on the ground for simulated hadronic and EM showers. In the case of a gamma-ray of 1 TeV (top left plot), one can see the Cherenkov light pool with a radius of typically 150 m, as well as for the 30 TeV case (bottom left plot), which includes some electrons striking the ground. In contrast, the hadronic shower generated by a 1 TeV proton (top right plot) displays heterogeneous and asymmetric structures reflecting differences in shower development. The rings are caused by muons hitting the ground. For the 30 TeV proton shower (bottom left plot), the Cherenkov light pool starts to be well-defined because the higher the shower energy, the more Cherenkov photons are produced and reach the ground, dominating the Cherenkov rings caused by muons.

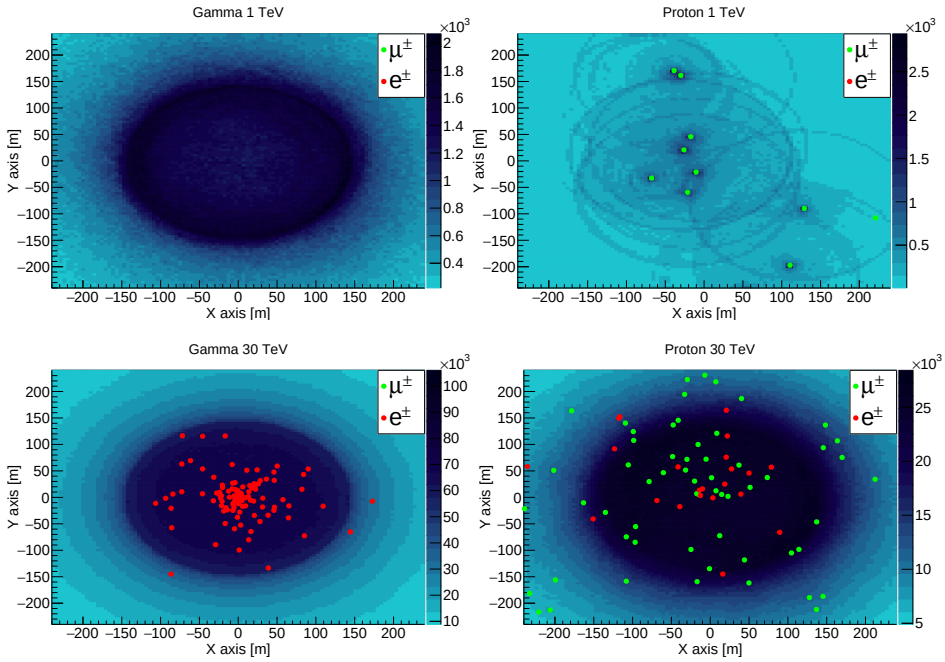

Figure 1.19: Cherenkov light distribution measured at ground. On the left, a gamma-ray shower of 1 TeV and 30 TeV is shown, and on the right, a proton shower of 1 TeV and 30 TeV. The images were simulated with CORSIKA. The green and red dots correspond to muons and electrons/positrons, respectively, arriving at the detection level.

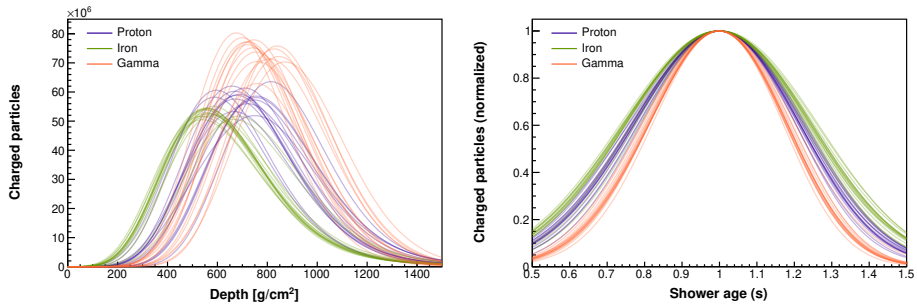

(a) Profiles as a function of depth.

(b) Profiles as a function of age.

Figure 1.20: Simulated longitudinal profiles of air showers as a function of depth (a) and shower age (b). Images taken from [111].

1.4.4 Shower universality

The concept of the *shower age* is related to the idea that all showers, at their maximum development, exhibit a certain degree of "similarity" to each other (which means to have the same age). This similarity is characterized by the fact that, in all showers at maximum, the energy spectra of most electrons and photons share the same shape [109]. The cascade theory gives the form of the shower age s defined as [110]:

$$s = \frac{3X}{X + 2X_{max}}, \tag{1.20}$$

where X is the atmospheric depth and X_{max} is the depth of the maximum. On the left side of Fig 1.20, it shows several profiles for each type of air shower, and on the right, the corresponding profiles as a function of the shower age [111]. It is possible to check that all profiles for the same primary share a universal behaviour near the maximum where $s = 1$ and along the shower age.

1.5 Artificial neural networks

The concept behind designing a neural network model draws an analogy from the information processing mechanisms found in biological organisms. In biological brains, neurons, which are electrically activated nerve cells, are interconnected through synapses, facilitating the transfer of information between neurons [112]. One equivalent machine learning (ML) architecture of this biological structure is the Artificial Neural Network (ANN), which learns from data to solve a specific task. The learning is done using mathematical functions called *neurons*. These neurons are arranged in *layers* and connected to each other, as shown in Fig 1.21. In the graphical description, the connections symbolize that the neurons of one layer become the inputs for the subsequent neurons in the next layer. This establishes a directional flow of information from layer to layer, classifying this architecture as a feed-forward neural network. In this discussion, we will explore one approach for optimizing neural networks: supervised learning. Supervised learning is an ML process where training data consists of input-output pairs. The input is accompanied by the correct answer (the label) and instructs the network on the desired task.

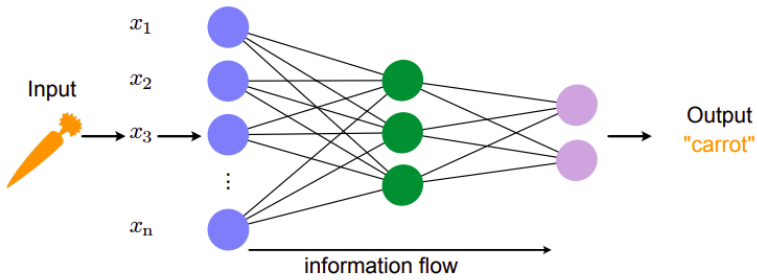

Figure 1.21: Basic architecture illustration of neural network with three layers: input layer (left), a hidden layer with three neurons (middle), and an output layer with two neurons (right). Image is taken from [112].

1.5.1 Neurons

The fundamental block of ANN is the *neuron*. A neuron is a real number and transfers the information through the layers throughout parameters known as *weights* and *biases*, optimised during the training of the network.

The linear function q_i that represents the value of the i-th neuron is:

$$q_i = \sum_j W_{ij} x_j + b_i, \tag{1.21}$$

where W_{ij} are the weights representing the connection strength of the j-th neuron with the i-th neuron, x_j are the input data of the preceding layer, and b_i is a constant known as the *bias*. This notation tells us that the value q of a neuron is the result of connections with all input neurons x_j from the previous layer (see schematic representation on the left side in Fig 1.22).

The neuron is transformed non-linearly using an *activation function g(q)* with the value q as input. The activation function represents the property that neuron spikes, producing a noticeable output when the input grows beyond a certain threshold value. Fig. 1.22 shows common choices of activation functions for input and hidden layers: Rectified Linear Unit (ReLU), sigmoid, and hyperbolic tangent function. A particular case of an activation function is the *softmax* used in the output layer. Let us label by $k = 1, \ldots, n$ the number of neurons in a layer with value q_k. Then, the softmax for a neuron k is given by:

$$g_k(q_1, \ldots, q_n) = \frac{e^{q_k}}{\sum_{k'=1}^{n} e^{q_{k'}}}. \tag{1.22}$$

The property $\sum_k g_k(q_1, \ldots, q_n) = 1$ can be derived from 5.2, which allows interpreting the output layer as a probability distribution and makes the softmax function useful for classification tasks.

1.5.2 Training

The goal of any ML algorithm is to calculate values that are as close as possible to the truth output for every input. The true value is called *label*, and for binary and multi-classification problems, the label is encoded in a one-hot vector. For a scenario composed of two classes, A and B (binary classification), the labels would be:

$$\begin{aligned} \text{class A} \longrightarrow \text{label} : l_0 &= \begin{pmatrix} 1 \\ 0 \end{pmatrix} \\ \text{class B} \longrightarrow \text{label} : l_1 &= \begin{pmatrix} 0 \\ 1 \end{pmatrix}. \end{aligned} \tag{1.23}$$

To measure how well the algorithm does the task, we use the definition of *loss function*. The lost function is computed by comparing the output of our algorithm with the true label of each sample i in a training data set. The

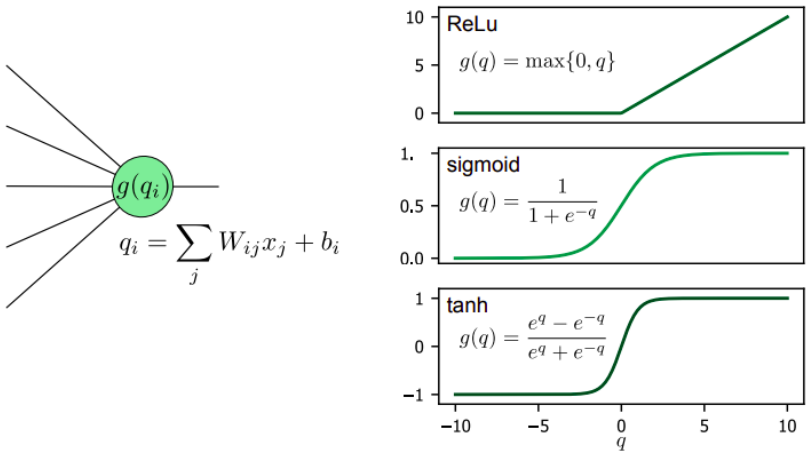

Figure 1.22: Left: schematic representation of a single neuron with its value $g(q)$. Right: Examples of activation functions: Rectified linear unit (ReLU), sigmoid, and hyperbolic tangent function. Image taken from [112].

most simple cost function L is given by the mean square error and defined as:

$$L(\theta) = \frac{1}{n} \sum_{i=0}^{n} (y_{(i)} - l_{(i)})^2, \tag{1.24}$$

where l_i are the true labels, $y_{(i)}$ are the outputs from the neural network and n is the total number of samples. The training process consists of minimizing $L(\theta)$ with respect to the weights and biases collectively denoted by θ. The gradient descent is an iterative method used to minimize the loss function numerically. The method can be seen as descending a hill in the parameter space until a local minimum is reached. The weights and biases are updated over training steps (epochs) using the derivatives of the cost function:

$$\theta_\alpha \to \theta_\alpha - \eta \frac{\partial L(\theta)}{\partial \theta_\alpha}. \tag{1.25}$$

where η is the learning rate representing the step size to be walked down the hill. The loss curve as a function of the epochs should have an initial steep decrease and stabilize toward the end of the training. The training is also verified in an independent data set called *validation* to avoid overfitting. One of the metrics to evaluate the performance of our neural network is accuracy, calculated in an independent *testing* set:

$$accuracy = \frac{correct\ predictions}{total\ predicitons} \tag{1.26}$$

1.5.3 Convolutional Neural Networks

Convolutional Neural Networks (CNNs) are a class of ANN that considers the geometric structure and identifies certain local patterns in the data (especially for pictures) [112]. CNN is one of the most successful tools for image classification. There are two main parts in the structure of a CNN: the convolutional layers plus the pooling layers, which focus on feature extraction, and the fully connected layer that makes the classification process. The following is a brief description of these types of layers.

Convolutional layer: This layer identifies local patterns such as straight or curved lines in the image. The patterns are encoded in kernels or filters with weights. As shown in Fig. 1.23, the filters convolve the image by an element-wise multiplication matrix with a portion of the image called the local receptive field. The convolution is repeated for each receptive field of the input. The output of this process defines the feature maps. After applying the filter to the full image, we obtain a feature map as output.

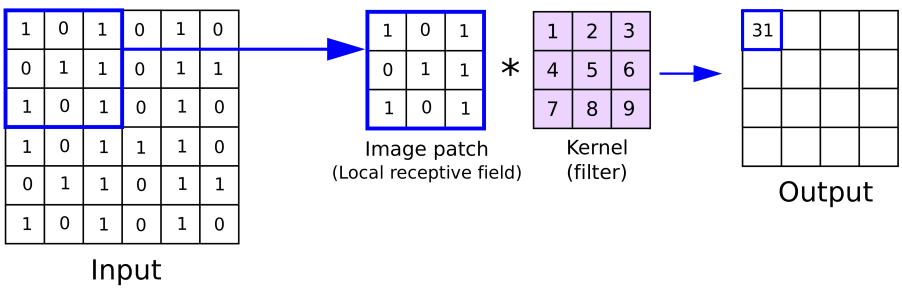

Figure 1.23: Schematics of a convolutional layer. The filter application is made over a specific image region (local receptive field) by an element-wise multiplication matrix. Image taken from [113].

Pooling layer: This layer reduces the spatial dimension of the feature map and typically goes after convolutional layers. The input feature map is compressed to a few neurons to contain the most significant information. There are two types: average pooling and max pooling, as shown in Fig.

1.24. The pool size defines the dimensional reduction. The *max pooling* detects any feature in the map by picking the neuron with the maximum value. Max pooling is useful to avoid zero values, i.e., dead neurons that do not represent a change in the training. In contrast, the *average pooling* is a direct compression that takes the average of the neurons.

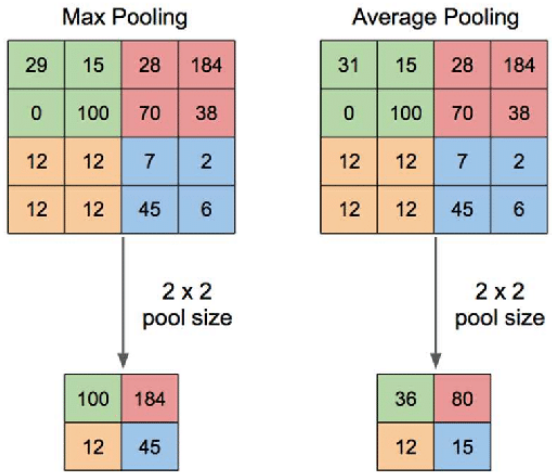

Figure 1.24: Output map after applying the two types of pooling layers in the feature map. Image taken from [114].

Dense layer: This fully connected layer of neurons goes after convolutional and pooling layers. Each neuron receives the extracted feature maps from the previous layers. The dense layers are structured to perform the classification task based on the information derived from the feature maps.

Dropout layer: it drops features similar to pooling layers. Nevertheless, dropout layers ignore neurons randomly during the training only. By dropping random neurons, dropout introduces noise to the network, which helps in making the network more robust to variations and perturbations in the input data. It also helps to identify the more general features better [112].

1.6 Outline of the thesis

This thesis is divided into two parts: I) Study of air shower detection using Cherenkov light and II) Iron/proton separation for air shower simulations with the CTA. Part I shows two proposed methods to reconstruct the depth of the shower maximum, and part II is focused on applying one of our methods to CTA simulations. It also includes the application of deep learning algorithms to separate the cosmic ray species.

Novel methods for air shower detection using Cherenkov light

The *Imaging Atmospheric Cherenkov Telescopes (IACTs)* have a central role in detecting gamma-ray air showers in the TeV energy range, as they reject cosmic-ray showers, which are considered background. In recent years, many IACTs have provided the possibility to reconstruct the cosmic-ray spectrum, which is limited by the identification of the primary mass. This thesis starts by tackling this problem by proposing a method to measure the shower maximum with an ideal array of telescopes. We aim to demonstrate the feasibility of measuring the X_{max} observable as a function of the distance to the shower impact. In chapter 3, we also proposed a more precise method to reconstruct the longitudinal shower profile. This method considers the distribution of the Cherenkov light around the shower axis and the contribution of all triggered telescopes. At the time of the writing of this manuscript, these results are already published.

Iron-proton separation for air showers simulations with the Cherenkov Telescope Array

In the second part, we tested our method that reconstructs the shower profile using the Cherenkov Telescope Array software simulations. We proposed a cut on the depth of shower maximum distribution to separate the iron events from proton showers. We also presented a deep learning architecture to classify images generated by iron and proton showers by training a *convolutional neural network (CNN)*. The CNN inputs combined the image pixel intensities, depth of shower maximum, and the event energy for images detected by Small-Sized Telescopes (SSTs) and Medium-Sized Telescopes (MSTs).

1.7 Contributions from co-authors

The work presented in this thesis was done with the contributions of several co-authors. This section summarizes the contributions of the PhD candidate and his co-authors in every chapter[4].

Chapter 2: Measuring the depth of the depth of shower maximum of extensive air showers using Cherenkov light

- **Andrés G. Delgado**: methodology, software, formal analysis, writing - original draft, review editing, and visualization.
- Vitor de Souza: conceptualization, methodology, software, writing - original draft, review editing, visualization, investigation, supervision and project administration.
- Luan B. Arbeletche: software, resources and investigation.
- Ralph Bird: supervision and project administration.
- Rene A. Ong: supervision and project administration.

Chapter 3: Cosmic-ray measurements with an array of Cherenkov telescopes using reconstruction of longitudinal profiles of air showers

- **Andrés G. Delgado**: methodology, software, formal analysis, writing - original draft, review editing, software, resources, investigation, and visualization.
- Vitor de Souza: conceptualization, methodology, software, writing - original draft, review editing, visualization, investigation, supervision and project administration.

Chapter 4: Cosmic-ray measurements by reconstructing longitudinal profiles for the Cherenkov Telescope Array

- **Andrés G. Delgado**: software development, co-writing, application of the methods, visualization, responsible for producing the results of propagation parameters.
- Manuela Vecchi: supervision, conceptualization, review and editing, inputs on the interpretation of the results.
- Vitor de Souza: supervision, conceptualization, review and editing, inputs on the interpretation of the results.

[4]The terminology of credit author statements are taken from `https://www.elsevier.com/authors/policies-and-guidelines/credit-author-statement`.

Chapter 5: Iron and proton separation using convolutional neural networks for the telescope Cherenkov Array

- **Andrés G. Delgado**: software development, co-writing, application of the methods, visualization, responsible for producing the results of propagation parameters.
- Manuela Vecchi: supervision, conceptualization, review and editing, inputs on the interpretation of the results.
- Vitor de Souza: supervision, conceptualization, review and editing, inputs on the interpretation of the results.

Bibliography

[1] Victor F. Hess. Über Beobachtungen der durchdringenden Strahlung bei sieben Freiballonfahrten. *Phys. Z.*, 13: 1084–1091, 1912. URL https://inspirehep.net/files/880fc3b9087fcfc846fab1e79df5b8eb.

[2] Victor Hess. On the Observations of the Penetrating Radiation during Seven Balloon Flights. *arXiv e-prints*, 7 2018. URL https://arxiv.org/abs/1808.02927.

[3] Dieter Fick and Dieter Hoffmann. Werner kolhörster (1887–1945): The german pioneer of cosmic ray physics. *Astroparticle Physics*, 53:50–54, 2014. ISSN 0927-6505. doi: https://doi.org/10.1016/j.astropartphys.2013.09.007. URL https://www.sciencedirect.com/science/article/pii/S0927650513001497. Centenary of cosmic ray discovery.

[4] Werner KOLHORSTER. Messungen der durchdringenden strahlung im freiballon in grosseren hohen. *Phys. Zeits.*, 14:1153–1156, 1913.

[5] Werner Kolhörster. Messungen der durchdringenden strahlungen bis in höhen von 9300 m. *Verh. deutsche phys. Gesellschaft*, 16:719–721, 1914.

[6] Preface. In A.M. HILLAS, editor, *Cosmic Rays*, The Commonwealth and International Library: Selected Readings in Physics, pages ix–x. Pergamon, 1972. ISBN 978-0-08-016724-4. doi: https://doi.org/10.1016/B978-0-08-016724-4.50003-3. URL https://www.sciencedirect.com/science/article/pii/B9780080167244500033.

[7] R. A. Millikan and I. S. Bowen. High frequency rays of cosmic origin i. sounding balloon observations at extreme altitudes. *Phys. Rev.*, 27:353–361, Apr 1926. doi: 10.1103/PhysRev.27.353. URL https://link.aps.org/doi/10.1103/PhysRev.27.353.

[8] R. A. Millikan and R. M. Otis. High frequency rays of cosmic origin ii. mountain peak and airplane observations. *Phys. Rev.*, 27:645–658, Jun 1926. doi: 10.1103/PhysRev.27.645. URL https://link.aps.org/doi/10.1103/PhysRev.27.645.

[9] R. A. Millikan and G. Harvey Cameron. High frequency rays of cosmic origin iii. measurements in snow-fed lakes at high altitudes. *Phys. Rev.*, 28:851–868, Nov 1926. doi: 10.1103/PhysRev.28.851. URL https://link.aps.org/doi/10.1103/PhysRev.28.851.

[10] Carl D. Anderson. The positive electron. *Phys. Rev.*, 43:491–494, Mar 1933. doi: 10.1103/PhysRev.43.491. URL https://link.aps.org/doi/10.1103/PhysRev.43.491.

[11] Seth H. Neddermeyer and Carl D. Anderson. Note on the nature of cosmic-ray particles. *Phys. Rev.*, 51:884–886, May 1937. doi: 10.1103/PhysRev.51.884. URL https://link.aps.org/doi/10.1103/PhysRev.51.884.

[12] J. C. Street and E. C. Stevenson. New evidence for the existence of a particle of mass intermediate between the proton and electron. *Phys. Rev.*, 52:1003–1004, Nov 1937. doi: 10.1103/PhysRev.52.1003. URL https://link.aps.org/doi/10.1103/PhysRev.52.1003.

[13] C. LATTES, G. OCCHIALINI, and POWELL. Observations on the tracks of slow mesons in photographic emulsions. *Nature*, 160: 486–492, 1947. doi: 10.1038/160486a0. URL https://doi.org/10.1038/160486a0.

[14] Patrick Maynard Stuart Blackett and Giuseppe Paolo Stanislao Occhialini. Some photographs of the tracks of penetrating radiation. *Proceedings of the Royal Society of London. Series A, Containing Papers of a Mathematical and Physical Character*, 139(839):699–726, 1933.

[15] Pierre Auger, P. Ehrenfest, R. Maze, et al. Extensive cosmic-ray showers. *Rev. Mod. Phys.*, 11:288–291, Jul 1939. doi: 10.1103/RevModPhys.11.288. URL https://link.aps.org/doi/10.1103/RevModPhys.11.288.

[16] John Linsley. Evidence for a primary cosmic-ray particle with energy 10^{20} ev. *Phys. Rev. Lett.*, 10:146–148, Feb 1963. doi: 10.1103/PhysRevLett.10.146. URL https://link.aps.org/doi/10.1103/PhysRevLett.10.146.

[17] Karl-Heinz Kampert and Alan A Watson. Extensive air showers and ultra high-energy cosmic rays: a historical review. *The European Physical Journal H*, 37(3):359–412, 2012.

[18] Kenneth Greisen. End to the cosmic-ray spectrum? *Phys. Rev. Lett.*, 16:748–750, Apr 1966. doi: 10.1103/PhysRevLett.16.748. URL https://link.aps.org/doi/10.1103/PhysRevLett.16.748.

[19] G. T. Zatsepin and V. A. Kuz'min. Upper Limit of the Spectrum of Cosmic Rays. *Soviet Journal of Experimental and Theoretical Physics Letters*, 4:78, August 1966.

[20] M. Takeda, N. Hayashida, K. Honda, et al. Extension of the cosmic-ray energy spectrum beyond the predicted greisen-zatsepin-kuz'min cutoff. *Phys. Rev. Lett.*, 81:1163–1166, Aug 1998. doi: 10.1103/PhysRevLett.81.1163. URL https://link.aps.org/doi/10.1103/PhysRevLett.81.1163.

[21] R. M. Baltrusaitis, R. Cady, G. L. Cassiday, et al. Evidence for a high-energy cosmic-ray spectrum cutoff. *Phys. Rev. Lett.*, 54:

1875–1877, Apr 1985. doi: 10.1103/PhysRevLett.54.1875. URL https://link.aps.org/doi/10.1103/PhysRevLett.54.1875.

[22] R. U. Abbasi, T. Abu-Zayyad, M. Allen, et al. First observation of the greisen-zatsepin-kuzmin suppression. *Phys. Rev. Lett.*, 100:101101, Mar 2008. doi: 10.1103/PhysRevLett.100.101101. URL https://link.aps.org/doi/10.1103/PhysRevLett.100.101101.

[23] J. Abraham, P. Abreu, M. Aglietta, et al. Observation of the suppression of the flux of cosmic rays above 4×10^{19} eV. *Phys. Rev. Lett.*, 101:061101, Aug 2008. doi: 10.1103/PhysRevLett.101.061101. URL https://link.aps.org/doi/10.1103/PhysRevLett.101.061101.

[24] H. Kawai, S. Yoshida, H. Yoshii, et al. Telescope array experiment. *Nuclear Physics B - Proceedings Supplements*, 175-176: 221–226, 2008. ISSN 0920-5632. doi: https://doi.org/10.1016/j.nuclphysbps.2007.11.002. URL https://www.sciencedirect.com/science/article/pii/S0920563207007992. Proceedings of the XIV International Symposium on Very High Energy Cosmic Ray Interactions.

[25] J. Abraham, P. Abreu, M. Aglietta, et al. Measurement of the depth of maximum of extensive air showers above 10^{18} eV. *Phys. Rev. Lett.*, 104:091101, Mar 2010. doi: 10.1103/PhysRevLett.104.091101. URL https://link.aps.org/doi/10.1103/PhysRevLett.104.091101.

[26] A. Aab, P. Abreu, M. Aglietta, et al. Depth of maximum of air-shower profiles at the pierre auger observatory. ii. composition implications. *Phys. Rev. D*, 90:122006, Dec 2014. doi: 10.1103/PhysRevD.90.122006. URL https://link.aps.org/doi/10.1103/PhysRevD.90.122006.

[27] Pedro Abreu et al. Interpretation of the Depths of Maximum of Extensive Air Showers Measured by the Pierre Auger Observatory. *JCAP*, 02:026, 2013. doi: 10.1088/1475-7516/2013/02/026.

[28] A. Aab, P. Abreu, M. Aglietta, et al. Evidence for a mixed mass composition at the 'ankle' in the cosmic-ray spectrum. *Physics Letters B*, 762:288–295, 2016. ISSN 0370-2693. doi: https://doi.org/10.1016/j.physletb.2016.09.039. URL https://www.sciencedirect.com/science/article/pii/S0370269316305433.

[29] A. Aab, P. Abreu, M. Aglietta, et al. Inferences on mass composition and tests of hadronic interactions from 0.3 to 100 eev using the water-cherenkov detectors of the pierre auger observatory. *Phys. Rev. D*, 96:122003, Dec 2017. doi: 10.1103/PhysRevD.96.122003. URL https://link.aps.org/doi/10.1103/PhysRevD.96.122003.

[30] A. M. Bykov, D. C. Ellison, A. Marcowith, and S. M. Osipov. Cosmic ray production in supernovae. *Space Sci. Rev.*, 214(1):41, 2018. doi: 10.1007/s11214-018-0479-4.

[31] Malcolm S. Longair. *High energy astrophysics*. Cambridge University Press, 3rd ed. Cambridge, 2011.

[32] Benedetto D'Ettorre Piazzoli, Si-Ming Liu, Domenico della Volpe, et al. Chapter 4 Cosmic-Ray Physics. *Chinese Physics C*, 46(3): 030004, March 2022. doi: 10.1088/1674-1137/ac3faa.

[33] C Sobey, A V Bilous, J-M Grießmeier, et al. Low-frequency Faraday rotation measures towards pulsars using LOFAR: probing the 3D Galactic halo magnetic field. *Monthly Notices of the Royal Astronomical Society*, 484(3):3646–3664, 01 2019. ISSN 0035-8711. doi: 10.1093/mnras/stz214. URL https://doi.org/10.1093/mnras/stz214.

[34] M. Tanabashi, K. Hagiwara, K. Hikasa, et al. Review of particle physics. *Phys. Rev. D*, 98:030001, Aug 2018. doi: 10.1103/PhysRevD.98.030001. URL https://link.aps.org/doi/10.1103/PhysRevD.98.030001.

[35] G. Giacinti and D. Semikoz. Model of Cosmic Ray Propagation in the Milky Way at the Knee. *arXiv e-prints*, art. arXiv:2305.10251, May 2023. doi: 10.48550/arXiv.2305.10251.

[36] A M Hillas. Can diffusive shock acceleration in supernova remnants account for high-energy galactic cosmic rays? *Journal of Physics G: Nuclear and Particle Physics*, 31(5):R95, apr 2005. doi: 10.1088/0954-3899/31/5/R02. URL https://dx.doi.org/10.1088/0954-3899/31/5/R02.

[37] V. I. Zatsepin and N. V. Sokolskaya. Three component model of cosmic ray spectra from 10 GeV to 100 PeV. A&A, 458(1):1–5, October 2006. doi: 10.1051/0004-6361:20065108.

[38] Julián Candia, Esteban Roulet, and Luis N. Epele. Turbulent diffusion and drift in galactic magnetic fields and the explanation of the knee in the cosmic ray spectrum. *Journal of High Energy Physics*, 2002(12):033, December 2002. doi: 10.1088/1126-6708/2002/12/033.

[39] Julián Candia, Silvia Mollerach, and Esteban Roulet. Cosmic ray spectrum and anisotropies from the knee to the second knee. J. Cosmology Astropart. Phys., 2003(5):003, May 2003. doi: 10.1088/1475-7516/2003/05/003.

[40] Paolo Lipari and Silvia Vernetto. The shape of the cosmic ray proton spectrum. *Astroparticle Physics*, 120:102441, 2020. ISSN 0927-6505. doi: https://doi.org/10.1016/j.astropartphys.

2020.102441. URL https://www.sciencedirect.com/science/article/pii/S0927650520300141.

[41] O. Adriani, G. C. Barbarino, G. A. Bazilevskaya, et al. PAMELA Measurements of Cosmic-Ray Proton and Helium Spectra. *Science*, 332(6025):69, April 2011. doi: 10.1126/science.1199172.

[42] M. Aguilar, D. Aisa, B. Alpat, et al. Precision measurement of the helium flux in primary cosmic rays of rigidities 1.9 gv to 3 tv with the alpha magnetic spectrometer on the international space station. *Phys. Rev. Lett.*, 115:211101, Nov 2015. doi: 10.1103/PhysRevLett.115.211101. URL https://link.aps.org/doi/10.1103/PhysRevLett.115.211101.

[43] A. D. Panov, J. H. Adams, H. S. Ahn, et al. Energy spectra of abundant nuclei of primary cosmic rays from the data of ATIC-2 experiment: Final results. *Bulletin of the Russian Academy of Sciences, Physics*, 73(5):564–567, June 2009. doi: 10.3103/S1062873809050098.

[44] Y. S. Yoon, T. Anderson, A. Barrau, et al. Proton and Helium Spectra from the CREAM-III Flight. ApJ, 839(1):5, April 2017. doi: 10.3847/1538-4357/aa68e4.

[45] O. Adriani, Y. Akaike, K. Asano, et al. Direct Measurement of the Cosmic-Ray Proton Spectrum from 50 GeV to 10 TeV with the Calorimetric Electron Telescope on the International Space Station. Phys. Rev. Lett., 122(18):181102, May 2019. doi: 10.1103/PhysRevLett.122.181102.

[46] Q. An, R. Asfandiyarov, P. Azzarello, et al. Measurement of the cosmic ray proton spectrum from 40 GeV to 100 TeV with the DAMPE satellite. *Science Advances*, 5(9):eaax3793, September 2019. doi: 10.1126/sciadv.aax3793.

[47] E. Atkin, V. Bulatov, V. Dorokhov, et al. New Universal Cosmic-Ray Knee near a Magnetic Rigidity of 10 TV with the NUCLEON Space Observatory. *Soviet Journal of Experimental and Theoretical Physics Letters*, 108(1):5–12, July 2018. doi: 10.1134/S0021364018130015.

[48] B. S. Acharya et al. *Science with the Cherenkov Telescope Array*. WSP, 11 2018. ISBN 978-981-327-008-4. doi: 10.1142/10986.

[49] Jörg R. Hörandel. On the knee in the energy spectrum of cosmic rays. *Astroparticle Physics*, 19(2):193–220, 2003. ISSN 0927-6505. doi: https://doi.org/10.1016/S0927-6505(02)00198-6. URL https://www.sciencedirect.com/science/article/pii/S0927650502001986.

[50] Alexey Yushkov. Mass composition of cosmic rays with energies above $10^{17.2}$ ev from the hybrid data of the pierre auger observatory. *Proceedings of 36th International Cosmic Ray Conference — PoS(ICRC2019)*, 2019.

[51] Karl-Heinz Kampert and Michael Unger. Measurements of the cosmic ray composition with air shower experiments. *Astroparticle Physics*, 35(10):660–678, 2012. ISSN 0927-6505. doi: https://doi.org/10.1016/j.astropartphys.2012.02.004. URL https://www.sciencedirect.com/science/article/pii/S0927650512000382.

[52] Interpretation of the depths of maximum of extensive air showers measured by the pierre auger observatory. *Journal of Cosmology and Astroparticle Physics*, 2013(02):026, feb 2013. doi: 10.1088/1475-7516/2013/02/026. URL https://dx.doi.org/10.1088/1475-7516/2013/02/026.

[53] J. Abraham, P. Abreu, M. Aglietta, et al. Measurement of the Depth of Maximum of Extensive Air Showers above 10^{18}eV. Phys. Rev. Lett., 104(9):091101, March 2010. doi: 10.1103/PhysRevLett.104.091101.

[54] A. Aab, P. Abreu, M. Aglietta, et al. Deep-learning based reconstruction of the shower maximum X_{max} using the water-Cherenkov detectors of the Pierre Auger Observatory. *Journal of Instrumentation*, 16(7):P07019, July 2021. doi: 10.1088/1748-0221/16/07/P07019.

[55] R. U. Abbasi, M. Abe, T. Abu-Zayyad, et al. Depth of Ultra High Energy Cosmic Ray Induced Air Shower Maxima Measured by the Telescope Array Black Rock and Long Ridge FADC Fluorescence Detectors and Surface Array in Hybrid Mode. ApJ, 858(2):76, May 2018. doi: 10.3847/1538-4357/aabad7.

[56] P. Sokolsky and HiRes Collaboration. Final Results from the High solution Fly's Eye (HiRes) Experiment. *Nuclear Physics B Proceedings Supplements*, 212:74–78, March 2011. doi: 10.1016/j.nuclphysbps.2011.03.010.

[57] S. P. Knurenko and I. S. Petrov. Estimation of the air shower depth of the maximum development by the relative fraction of muons and the composition of cosmic rays in the energy region $E_0 \geqslant 5$ EeV by yakutsk array data. *Phys. Rev. D*, 107:063017, Mar 2023. doi: 10.1103/PhysRevD.107.063017. URL https://link.aps.org/doi/10.1103/PhysRevD.107.063017.

[58] A. Corstanje, S. Buitink, H. Falcke, et al. Depth of shower maximum and mass composition of cosmic rays from 50 PeV to 2 EeV measured

with the LOFAR radio telescope. Phys. Rev. D, 103(10):102006, May 2021. doi: 10.1103/PhysRevD.103.102006.

[59] NASA. The fermi gamma-ray space telescope, 2022. Accessed Jun 19, 2023. https://fermi.gsfc.nasa.gov/.

[60] Trevor C. Weekes. Very high energy gamma-ray astronomy. *Physics Reports*, 160(1):1–121, 1988. ISSN 0370-1573. doi: https://doi.org/10.1016/0370-1573(88)90177-9. URL https://www.sciencedirect.com/science/article/pii/0370157388901779.

[61] H. Alfvén and N. Herlofson. Cosmic radiation and radio stars. *Phys. Rev.*, 78:616–616, Jun 1950. doi: 10.1103/PhysRev.78.616. URL https://link.aps.org/doi/10.1103/PhysRev.78.616.

[62] M Ryle. Evidence for the stellar origin of cosmic rays. *Proceedings of the Physical Society. Section A*, 62(8):491, aug 1949. doi: 10.1088/0370-1298/62/8/303. URL https://dx.doi.org/10.1088/0370-1298/62/8/303.

[63] W. Baade and F. Zwicky. Remarks on super-novae and cosmic rays. *Phys. Rev.*, 46:76–77, Jul 1934. doi: 10.1103/PhysRev.46.76.2. URL https://link.aps.org/doi/10.1103/PhysRev.46.76.2.

[64] W. L. Kraushaar, G. W. Clark, G. P. Garmire, et al. High-Energy Cosmic Gamma-Ray Observations from the OSO-3 Satellite. ApJ, 177:341, November 1972. doi: 10.1086/151713.

[65] C. E. Fichtel, R. C. Hartman, D. A. Kniffen, et al. High-energy gamma-ray results from the second Small Astronomy Satellite. ApJ, 198:163–182, May 1975. doi: 10.1086/153590.

[66] B. N. Swanenburg, K. Bennett, G. F. Bignami, et al. Second COS-B catalogue of high-energy gamma-ray sources. ApJ, 243:L69–L73, January 1981. doi: 10.1086/183445.

[67] N. Gehrels, E. Chipman, and D. Kniffen. The Compton Gamma Ray Observatory. ApJS, 92:351, June 1994. doi: 10.1086/191978.

[68] Tavani, M., Barbiellini, G., Argan, A., et al. The agile mission. *A&A*, 502(3):995–1013, 2009. doi: 10.1051/0004-6361/200810527. URL https://doi.org/10.1051/0004-6361/200810527.

[69] W. B. Atwood, A. A. Abdo, M. Ackermann, et al. The Large Area Telescope on the Fermi Gamma-Ray Space Telescope Mission. ApJ, 697(2):1071–1102, June 2009. doi: 10.1088/0004-637X/697/2/1071.

[70] PMS Blackett. A possible contribution to the night sky from the cerenkov radiation emitted by cosmic rays. *The emission spectra of the night sky and aurorae*, page 34, 1948.

[71] W. Galbraith and J. V. Jelley. Light Pulses from the Night Sky associated with Cosmic Rays. Nature, 171(4347):349–350, February 1953. doi: 10.1038/171349a0.

[72] G. G. Fazio, H. F. Helmken, G. H. Rieke, and T. C. Weekes. An experiment to search for discrete sources of cosmic gamma rays in the 1011 to 1012ev region. *Canadian Journal of Physics*, 46(10): S451–S455, 1968. doi: 10.1139/p68-268. URL https://doi.org/10.1139/p68-268.

[73] T. C. Weekes, G. G. Fazio, H. F. Helmken, et al. A Search for Discrete Sources of Cosmic Gamma Rays of Energy $10\hat{\{}11\}$-$10\hat{\{}12\}$ eV. ApJ, 174:165, May 1972. doi: 10.1086/151479.

[74] A. M. Hillas. Cerenkov Light Images of EAS Produced by Primary Gamma Rays and by Nuclei. In *19th International Cosmic Ray Conference (ICRC19), Volume 3*, volume 3 of *International Cosmic Ray Conference*, page 445, August 1985.

[75] MAGIC Group. The MAGIC telescopes, 2023. Accessed Jun 21, 2023. https://magic.mpp.mpg.de/.

[76] H.E.S.S. Collaboration. H.e.s.s. high energy stereoscopic system, 2023. Accessed Jun 21, 2023. https://www.mpi-hd.mpg.de/hfm/HESS/.

[77] VERITAS. Very Energetic Radiation Imaging Telescope Array System, 2004. Accessed Jun 21, 2023. https://veritas.sao.arizona.edu/.

[78] S. P. Wakely and D. Horan. TeVCat: An online catalog for Very High Energy Gamma-Ray Astronomy. In *International Cosmic Ray Conference*, volume 3 of *International Cosmic Ray Conference*, pages 1341–1344, January 2008.

[79] Scott Wakely and Deirdre Horan. TeVCat. Accessed Jun 21, 2023. http://tevcat.uchicago.edu/.

[80] A. Acharyya, R. Adam, C. Adams, et al. Sensitivity of the cherenkov telescope array to a dark matter signal from the galactic centre. *Journal of Cosmology and Astroparticle Physics*, 2021(01):057, jan 2021. doi: 10.1088/1475-7516/2021/01/057. URL https://dx.doi.org/10.1088/1475-7516/2021/01/057.

[81] H.E.S.S. Collaboration, Abramowski, A., Acero, F., et al. Measurement of the extragalactic background light imprint on the spectra of the brightest blazars observed with h.e.s.s. *A&A*, 550:A4, 2013. doi: 10.1051/0004-6361/201220355. URL https://doi.org/10.1051/0004-6361/201220355.

[82] H. Abdalla, H. Abe, F. Acero, et al. Sensitivity of the Cherenkov Telescope Array for probing cosmology and fundamental physics

with gamma-ray propagation. J. Cosmology Astropart. Phys., 2021 (2):048, February 2021. doi: 10.1088/1475-7516/2021/02/048.

[83] Andrei Bykov, Neil Gehrels, Henric Krawczynski, et al. Particle Acceleration in Relativistic Outflows. Space Sci. Rev., 173(1-4): 309–339, November 2012. doi: 10.1007/s11214-012-9896-y.

[84] F. Aharonian, A. G. Akhperjanian, A. R. Bazer-Bachi, et al. First ground-based measurement of atmospheric cherenkov light from cosmic rays. *Phys. Rev. D*, 75:042004, Feb 2007. doi: 10.1103/PhysRevD.75.042004. URL https://link.aps.org/doi/10.1103/PhysRevD.75.042004.

[85] A. Archer, W. Benbow, R. Bird, et al. Measurement of the iron spectrum in cosmic rays by veritas. *Phys. Rev. D*, 98:022009, Jul 2018. doi: 10.1103/PhysRevD.98.022009. URL https://link.aps.org/doi/10.1103/PhysRevD.98.022009.

[86] G. Di Sciascio. The lhaaso experiment: From gamma-ray astronomy to cosmic rays. *Nuclear and Particle Physics Proceedings*, 279-281: 166–173, 2016. ISSN 2405-6014. doi: https://doi.org/10.1016/j.nuclphysbps.2016.10.024. URL https://www.sciencedirect.com/science/article/pii/S240560141630205X. Proceedings of the 9th Cosmic Ray International Seminar.

[87] A. Acharyya, I. Agudo, E.O. Angüner, et al. Monte carlo studies for the optimisation of the cherenkov telescope array layout. *Astroparticle Physics*, 111:35–53, 2019. ISSN 0927-6505. doi: https://doi.org/10.1016/j.astropartphys.2019.04.001. URL https://www.sciencedirect.com/science/article/pii/S0927650519300234.

[88] D. Bose, V. R. Chitnis, P. Majumdar, and A. Shukla. Galactic and extragalactic sources of very high energy gamma rays. *European Physical Journal Special Topics*, 231(1):27–66, January 2022. doi: 10.1140/epjs/s11734-022-00434-8.

[89] Heinrich J. Völk and Konrad Bernlöhr. Imaging very high energy gamma-ray telescopes. *Experimental Astronomy*, 25(1-3):173–191, August 2009. doi: 10.1007/s10686-009-9151-z.

[90] E B Postnikov, A P Kryukov, S P Polyakov, et al. Gamma/hadron separation in imaging air cherenkov telescopes using deep learning libraries tensorflow and pytorch. *Journal of Physics: Conference Series*, 1181(1):012048, feb 2019. doi: 10.1088/1742-6596/1181/1/012048. URL https://dx.doi.org/10.1088/1742-6596/1181/1/012048.

[91] Maria Vasyutina et al. Gamma/Hadron Separation for a Ground Based IACT in Experiment TAIGA Using Machine Learning Methods. *PoS*, DLCP2021:008, 2022. doi: 10.22323/1.410.0008.

[92] D. Nieto Castaño, A. Brill, B. Kim, et al. Exploring deep learning as an event classification method for the Cherenkov Telescope Array. In *35th International Cosmic Ray Conference (ICRC2017)*, volume 301 of *International Cosmic Ray Conference*, page 809, July 2017. doi: 10.22323/1.301.0809.

[93] I. Shilon, M. Kraus, M. Büchele, et al. Application of deep learning methods to analysis of imaging atmospheric cherenkov telescopes data. *Astroparticle Physics*, 105:44–53, 2019. ISSN 0927-6505. doi: https://doi.org/10.1016/j.astropartphys.2018.10.003. URL https://www.sciencedirect.com/science/article/pii/S0927650518301178.

[94] Mikaël Jacquemont, Thomas Vuillaume, Alexandre Benoit, et al. First full-event reconstruction from imaging atmospheric cherenkov telescope real data with deep learning. In *2021 International Conference on Content-Based Multimedia Indexing (CBMI)*, pages 1–6, 2021. doi: 10.1109/CBMI50038.2021.9461918.

[95] R. D. Parsons and J. A. Hinton. A Monte Carlo Template based analysis for Air-Cherenkov Arrays. *Astropart. Phys.*, 56:26–34, 2014. doi: 10.1016/j.astropartphys.2014.03.002.

[96] M. Lemoine-Goumard, B. Degrange, and M. Tluczykont. Selection and 3d-reconstruction of gamma-ray-induced air showers with a stereoscopic system of atmospheric cherenkov telescopes. *Astroparticle Physics*, 25(3):195–211, 2006. ISSN 0927-6505. doi: https://doi.org/10.1016/j.astropartphys.2006.01.005. URL https://www.sciencedirect.com/science/article/pii/S0927650506000065.

[97] A. M. Hillas. Cerenkov Light Images of EAS Produced by Primary Gamma Rays and by Nuclei. In *19th International Cosmic Ray Conference (ICRC19), Volume 3*, volume 3 of *International Cosmic Ray Conference*, page 445, August 1985.

[98] Descriptive hillas. https://github.com/cta-observatory/ctapipe/issues/1078. Accessed: 2023-02-17.

[99] Mathieu de Naurois. Analysis methods for Atmospheric Cerenkov Telescopes. In *7th Workshop on Towards a Network of Atmospheric Cherenkov Detectors 2005*, pages 149–161, 7 2006.

[100] Piron, F., Djannati-Ataï, A., Punch, M., et al. Temporal and spectral gamma-ray properties of mkn 421 above 250 gev from cat observations between 1996 and 2000. *A&A*, 374(3):895–

906, 2001. doi: 10.1051/0004-6361:20010798. URL https://doi.org/10.1051/0004-6361:20010798.

[101] Gabriel Pérez Diaz, IAC . The technology behind the next generation very high-energy gamma-ray detector, 2023. Accessed Aug 31, 2023. https://www.cta-observatory.org/project/technology/.

[102] CTAO Performance . CTAO's expected "Alpha Configuration" performance, 2023. Accessed Aug 31, 2023. https://www.cta-observatory.org/science/ctao-performance/#1472563157332-1ef9e83d-426c.

[103] Ralph Engel, Dieter Heck, and Tanguy Pierog. Extensive air showers and hadronic interactions at high energy. *Annual Review of Nuclear and Particle Science*, 61(1):467–489, 2011. doi: 10.1146/annurev.nucl.012809.104544. URL https://doi.org/10.1146/annurev.nucl.012809.104544.

[104] Anne Zilles. *Introduction to Cosmic Rays and Extensive Air Showers*, pages 1–13. Springer International Publishing, Cham, 2017. ISBN 978-3-319-63411-1. doi: 10.1007/978-3-319-63411-1_1. URL https://doi.org/10.1007/978-3-319-63411-1_1.

[105] Peter K.F. Grieder. *Extensive air showers:* High Energy Phenomena and Astrophysical Aspects; A Tutorial, Reference Manual and Data Book. Springer, New York, 2 edition, 2010.

[106] W. Heitler. *The quantum theory of radiation*, volume 5 of *International Series of Monographs on Physics*. Oxford University Press, Oxford, 1936.

[107] J. Matthews. A Heitler model of extensive air showers. *Astroparticle Physics*, 22(5-6):387–397, January 2005. doi: 10.1016/j.astropartphys.2004.09.003.

[108] David J Fegan. /hadron separation at tev energies. *Journal of Physics G: Nuclear and Particle Physics*, 23(9):1013, sep 1997. doi: 10.1088/0954-3899/23/9/004. URL https://dx.doi.org/10.1088/0954-3899/23/9/004.

[109] Paolo Lipari. Concepts of "age" and "universality" in cosmic ray showers. Phys. Rev. D, 79(6):063001, March 2009. doi: 10.1103/PhysRevD.79.063001.

[110] Bruno Rossi and Kenneth Greisen. Cosmic-ray theory. *Rev. Mod. Phys.*, 13:240–309, Oct 1941. doi: 10.1103/RevModPhys.13.240. URL https://link.aps.org/doi/10.1103/RevModPhys.13.240.

[111] Luan Bonneau Arbeletche and Luiz Vitor de Souza Filho. Simulation of extensive air showers and its detection. Master's thesis, Universidade de São Paulo, 2021.

[112] Titus Neupert, Mark H Fischer, Eliska Greplova, et al. Introduction to Machine Learning for the Sciences. *arXiv e-prints*, art. arXiv:2102.04883, February 2021. doi: 10.48550/arXiv.2102.04883.

[113] Anh H. Reynolds. Convolutional neural networks (CNNs), 2019. Accessed Jun 14, 2023. https://anhreynolds.com/blogs/cnn.html.

[114] Vishal Rajput. Pooling layers in neural nets and their variants, 2022. Accessed Jun 14, 2023. https://medium.com/aiguys/pooling-layers-in-neural-nets-and-their-variants-f6129fc4628b.

Part I

Novel methods for air shower detection using Cherenkov light.

2. Measuring the depth of shower maximum of extensive air showers using Cherenkov light

Andrés G. Delgado Giler, Luan B. Arbeletche, Ralph Bird, Rene A. Ong, Vitor de Souza
Published in Astroparticle Physics
doi: 10.1016/j.astropartphys.2020.102508

ABSTRACT

A method is proposed to reconstruct the depth at which showers reach the maximum number of charged particles ($X_{max}^{charged}$) using atmospheric Cherenkov telescopes. The dependence of the Cherenkov signal with telescope distance from the shower core is explored, and a region in which the measurement is possible is determined (150 to 200 m). A parametrization is presented to reconstruct $X_{max}^{charged}$. The resolution of the method is studied as a function of energy for different primary particle types and for telescope fields of view ranging from 3.5° to 10°. Good resolution ($\sim 25\,g/cm^2$) is achieved for most of the cases of primary particle type (gamma ray, proton, and iron nuclei) and energy ($10\,TeV < E < 300\,TeV$). Very good resolution ($< 15\,g/cm^2$) is achieved in the best cases, and not-so-good resolution ($> 40\,g/cm^2$) is seen for energies below 30 TeV. The results presented here contribute to the understanding of the development of gamma-ray showers and suggest another possibility of using atmospheric Cherenkov telescopes to study cosmic rays in the TeV-PeV energy range.

2.1 Introduction

The imaging atmospheric Cherenkov telescope (IACT) technique has reached maturity with the observatories currently in operation: HESS [1], MAGIC [2] and VERITAS [3]. Currently, the precision of the instruments and the sophistication of the analysis allow the reconstruction of a gamma-ray air shower typically with 0.1° accuracy in the arrival direction and the determination of the gamma-ray energy with 15% resolution [4, 5, 6]. Thanks to their good performance, more than a hundred TeV gamma-ray sources have been discovered [7] and carefully studied, leading to important discoveries in high-energy astrophysics. The next stage is the Cherenkov Telescope Array (CTA) [8] which is presently under development. The CTA baseline design calls for 118 telescopes to be installed at two sites covering areas of $0.6\,\mathrm{km}^2$ on La Palma, Spain, and $4\,\mathrm{km}^2$ near Paranal, Chile. Each telescope of CTA detecting the same shower will offer a different view of the shower, and the multitude of images will offer a unique perspective of the air shower development.

Atmospheric Cherenkov telescopes are typically used for gamma-ray astrophysics studies. Non-gamma-ray events are mostly rejected by the telescope trigger and in the subsequent data analysis. Only a few dedicated analyses have been developed to study electron [9, 10, 11], proton [12] and iron nuclei primaries [13, 14]. For even the strongest gamma-ray sources, the flux of non-gamma-ray events is at least 1000 times higher than the flux of gamma-ray events at TeV energies. A crude estimate based on the extrapolation of the proton energy spectrum measured by AMS-02 [15] predicts that VERITAS detects more than 1000 proton events above 1 PeV per year of operation. The study of cosmic rays (non-gamma rays) with energies ranging from $10\,\mathrm{TeV}$ to $1\,\mathrm{PeV}$ lacks precision because not many events have been measured either by space or ground-based detectors. That happens because it is very challenging to extend the sensitivity in energy of space experiments because of the decreasing flux and very hard to extend down in energy the sensitivity of ground-based experiments because of the reduced number of particles reaching the ground.

Previous studies have proposed ways to study the cosmic ray composition using IACT [16, 17] based on the measurement of the Cherenkov light generated by the primary particle and by measuring the lateral distribution of Cherenkov light. Previous studies report $\mathrm{X}_{\mathrm{max}}^{\mathrm{charged}}$ reconstruction methods with resolution around $30\ \mathrm{g/cm}^2$ for gamma-ray events with energy below $10\,\mathrm{TeV}$ as seen by the H.E.S.S. experiment [18]. This paper proposes a new technique to reconstruct the depth at which the air shower reaches the maximum number of charged particles ($\mathrm{X}_{\mathrm{max}}^{\mathrm{charged}}$) using the data measured

by IACTs. The new method is based on the measurement of the longitudinal development of the Cherenkov light by telescopes further than 150 m from the shower core. The key aspect of the method is the capability of IACTs to measure the development of the longitudinal profile of Cherenkov photons. This feature explored here could be used in tandem with previous proposals of reconstruction of $X_{\rm max}^{\rm charged}$ and with composition studies based on the direct Cherenkov light from the primary particle.

It has long been known that $X_{\rm max}^{\rm charged}$ correlates with the primary particle type [19], and this variable has been used for primary identification in the data analysis of fluorescence telescopes [20, 21, 22]. However, the beamed emission of the Cherenkov light makes the analysis of the longitudinal profile of charged particles measured by IACT more complicated than the analysis of the fluorescence light, which is emitted isotropically. It has already been pointed out by Hillas [23] that the longitudinal development measured by an IACT depends on the position of the telescope and also that at larger distances ($> 200\,$m) from the shower core, the "Cherenkov flux traces the longitudinal development surprisingly faithfully". However, this idea of exploring the longitudinal development in shower reconstruction seems not to be fully developed in modern data analysis.

Given the significance of $X_{\rm max}^{\rm charged}$, the method developed here could impact the analysis procedures in IACT in many ways: a) better discrimination of gamma-ray events, b) an enhancement of the science scope of IACTs to non-gamma-ray events can be developed especially towards mass composition studies of all primaries, c) improvements of the air-shower reconstruction in observatories with large number of telescopes (CTA) could be derived and d) a better understanding of the shower physics is also possible. The method proposed here does not include details of the telescope or of the reconstruction chain. The details of each analysis chain and the characteristics of each observatory need to be taken into account to get the final resolution of the method. Nevertheless, the resolution obtained here is robust even when bad-case scenarios are considered.

Throughout the paper, the conditions in which Cherenkov light detected by IACTs can be used to calculate $X_{\rm max}^{\rm charged}$ are explained. The dependence on telescope distance from the shower core is explored in detail. In section 2.2, modern simulation software packages are used to produce a large library of gamma-ray, proton, and iron nuclei showers. In section 2.3, a method is proposed to calculate $X_{\rm max}^{\rm charged}$ using telescopes outside the Cherenkov cone ($> 150\,$m from the shower core). It is shown that the method works for a wide energy range and all primaries. A parametrization useful to data analysis is given. The $X_{\rm max}^{\rm charged}$ resolution achieved by this technique suggests the possibility that IACT could measure the cosmic ray

energy spectrum for groups of elements for energies ranging from 10's of TeV to 1 PeV. Finally, in section 2.4, the main limitations of the technique are discussed, and the conclusions are presented in section 2.5.

2.2 Simulation

2.2.1 Air shower simulation

The CORSIKA version 7.6300 software package [24] was used to simulate 10^4 air showers for each case described below. Three primary particles were considered: gamma rays, proton (A = 1) and iron nuclei (A = 56) with energies of 10 TeV, 30 TeV, 100 TeV and 300 TeV. The incident zenith was set to 20° and azimuthal angles were allowed to vary randomly. The cutoff energies for secondary particles of the air shower were set to 300 MeV for hadrons, 100 MeV for muons, 20 MeV for electrons, and 20 MeV for photons (including π^0). The observation level was fixed at 2150 m above sea level. EPOS-LHC [25] and FLUKA [26] codes were used to simulate the hadronic interactions. The longitudinal development of all particles in the shower was recorded in steps of 5 g/cm^2. The depth at which the shower reaches the maximum number of charged particles ($\mathrm{X}_{\mathrm{max}}^{\mathrm{charged}}$) was calculated by fitting the number of charged particles as a function of depth with a Gaisser-Hillas function [27]:

$$N(X) = N_{max}\left(\frac{X - X_0}{\mathrm{X}_{\mathrm{max}}^{\mathrm{charged}} - X_0}\right)^{\frac{\mathrm{X}_{\mathrm{max}}^{\mathrm{charged}} - X_0}{\lambda}} \exp\left(\frac{\mathrm{X}_{\mathrm{max}}^{\mathrm{charged}} - X}{\lambda}\right) \quad (2.1)$$

in which X is atmospheric depth, N_{max} is the maximum number of particles in the shower, λ and X_0 are mass and energy dependent fit parameters.

2.2.2 Reconstruction of longitudinal Cherenkov profile

Cherenkov photons were produced in bunches of up to five and propagated to ground level. No telescope simulation was considered. A simple field of view (FOV) cut is used to simulate the aperture limitation of the telescopes. All photon bunches reaching spheres with 5 m radius were considered detected, and their position, arrival direction, and energy were stored. The simplified telescopes were placed in 10 m steps up to 300 m from the shower core. Cherenkov photons are not attenuated in the simulations considered here. The study is concentrated in very high energy (> 10 TeV); therefore, the shower produces light well above the trigger level of current

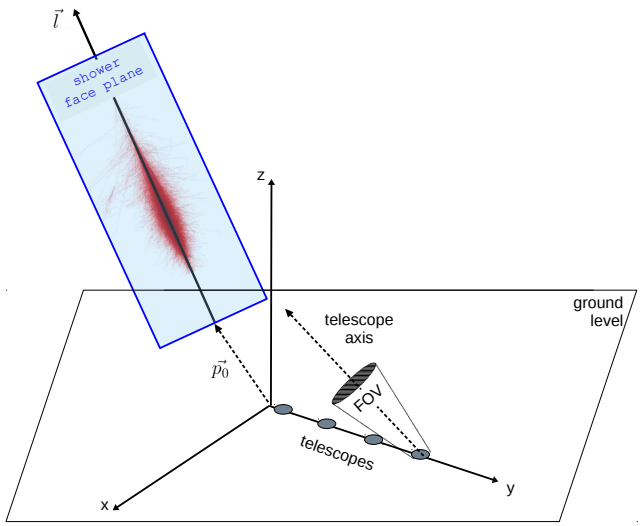

Figure 2.1: Definition of the shower face plane and detector geometry. The various quantities are defined in the text.

IACTs. One exception to this case is going to be noted below for telescopes with small FOV and far away from the shower core.

The shower face plane is defined here by the set of points $\vec{p}$ such that $(\vec{p} - \vec{p_0}) \cdot \vec{n} = 0$, where $\vec{p_0}$ is the shower core position and $\vec{n}$ is the direction perpendicular to the shower face plane. The vector $\vec{n}$ is defined such that its projection at ground points towards the telescope position. Therefore, for each telescope, a different shower face plane is assigned. See figure 2.1 for a visualization of the shower face plane in which $\vec{l}$ is the direction of the primary particle. In this paper, it is assumed that the direction of the primary particle ($\vec{l}$), the core position ($\vec{p_0}$) and the energy are reconstructed using one of the techniques available in the literature.

The longitudinal Cherenkov profile is reconstructed by projecting the arrival direction of each photon bunch back into the shower face plane. Examples of the Cherenkov photons projected on the shower face plane are shown in figure 2.2. The subsequent projection of all bunches on the shower axis results in figure 2.3, which shows the longitudinal Cherenkov profile. The depth at which the longitudinal Cherenkov profile reaches its maximum ($X_{\mathrm{max}}^{\mathrm{Cherenkov}}$) is calculated by fitting a second-order polynomial

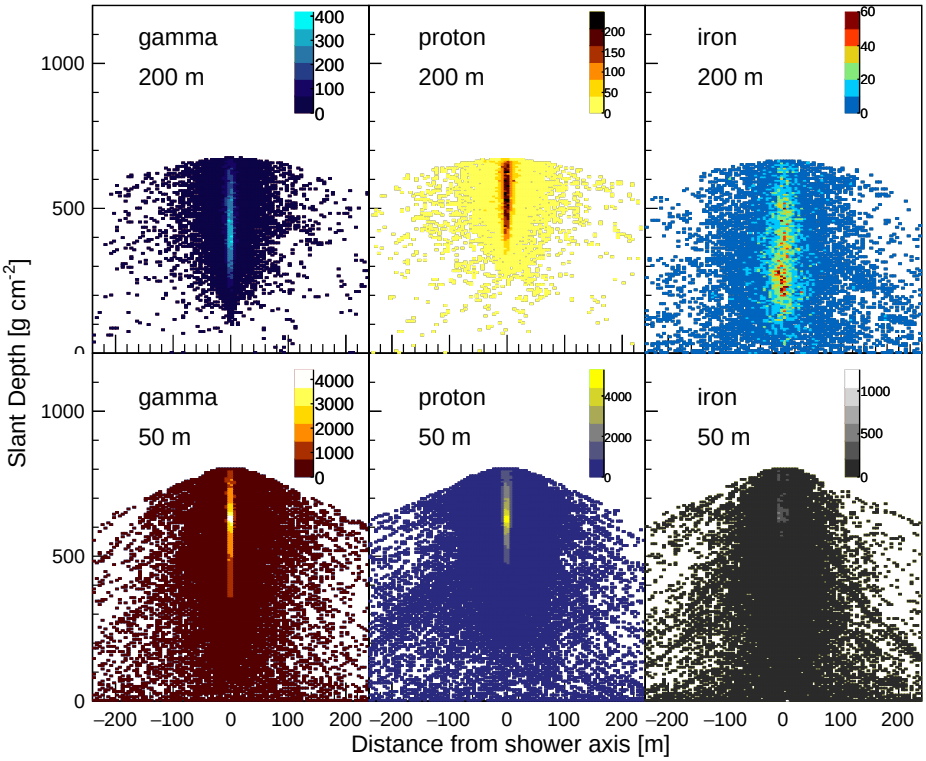

Figure 2.2: Examples of projections of Cherenkov photons in the shower face plane. Showers were initiated by gamma ray (left), proton (middle) and iron nuclei (right) with primary energies of 100 TeV. Telescopes were located at 50 m (lower row) and 200 m (upper row) from the shower core. The colour code shows the number of Cherenkov photons. Note that each plot has its own colour scale.

function as shown in figure 2.3. Only events surviving fit quality criteria (cuts) are used in the following calculations. The quality cuts are: a) the fit must result in a parabola with its opening in the downward direction (negative coefficient for the second order term), b) the fitted $X_{\max}^{\text{Cherenkov}}$ should be bracketed by measured points and be further than 45 g/cm^2 from the edge[1] of the detected profile and c) chi-squared per degree of freedom ($\chi^2/ndof$) smaller than 10. Errors are taken to be Poissonian, and the $ndof$ is the number of points in the fit minus three. Roughly 80% of the simulated events survived these cuts depending slightly on energy.

[1]The edge is defined by the intersection of the longitudinal profile with the telescopes' FOV.

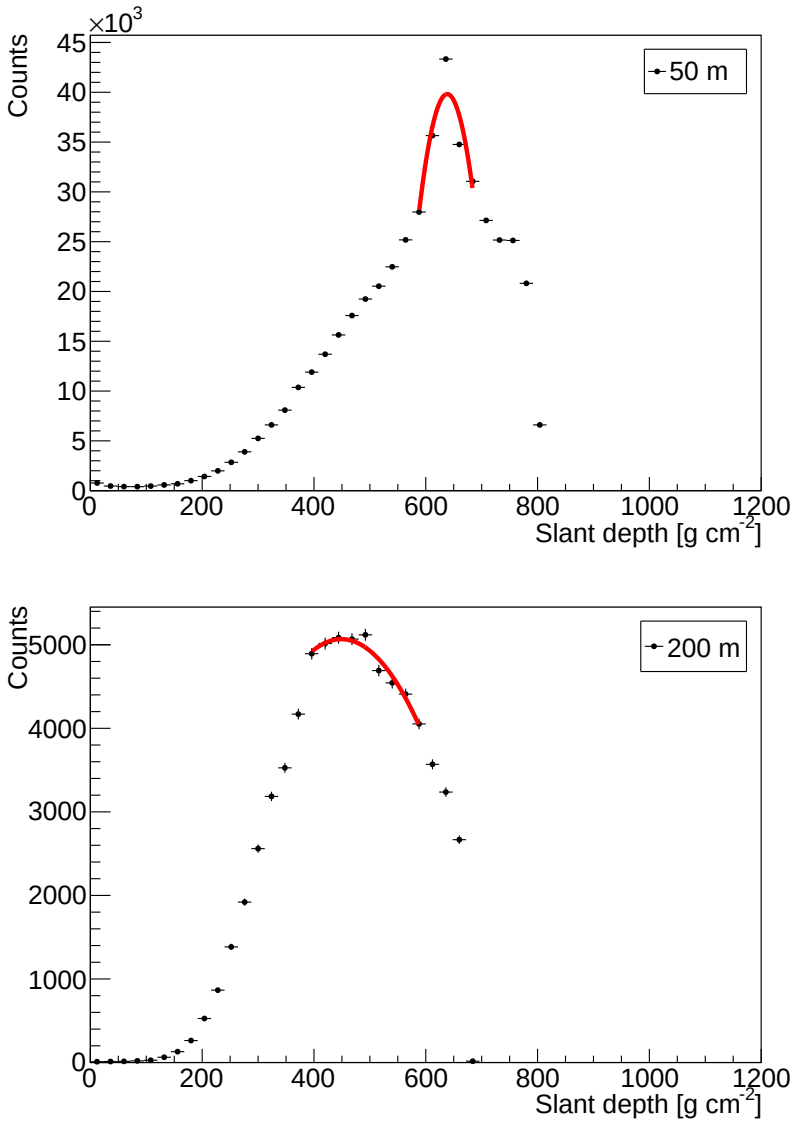

Figure 2.3: Longitudinal development of the number of Cherenkov photons for a gamma-ray shower with 100 TeV seen by telescopes at 50 m (top) and 200 (bottom) m from the shower core. The number of photons was fitted by a second-order polynomial, as shown in red.

2.3 Analysis of the longitudinal Cherenkov profile

The arrival direction of each photon in the telescope accumulates information about a large set of factors, including the variation of the index of refraction with height, the evolution of the electron energy spectrum with shower age, the scattering of the electrons around the shower axis and of the photons (Rayleigh [28] and Mie [29]) along the way to the telescope. The deconvolution of all these effects is not a straightforward problem, but it is easy to understand that all together, they result that $X_{max}^{Cherenkov}$ depends on the telescope position relative to the shower core. Besides, these factors might also mean that $X_{max}^{Cherenkov}$ is different from the depth at which the shower reaches its maximum number of particles ($X_{max}^{charged}$).

Figure 2.4 shows the longitudinal Cherenkov profile of the same shower as seen by telescopes with varying distances from the shower core. The dependence of $X_{max}^{Cherenkov}$ with the distance of the telescope from the shower core is discernible. Figure 2.5 shows examples of $X_{max}^{Cherenkov}$ versus the distance from the telescope to the shower core for three gamma-ray showers. $X_{max}^{charged}$ is also shown by the horizontal dashed line.

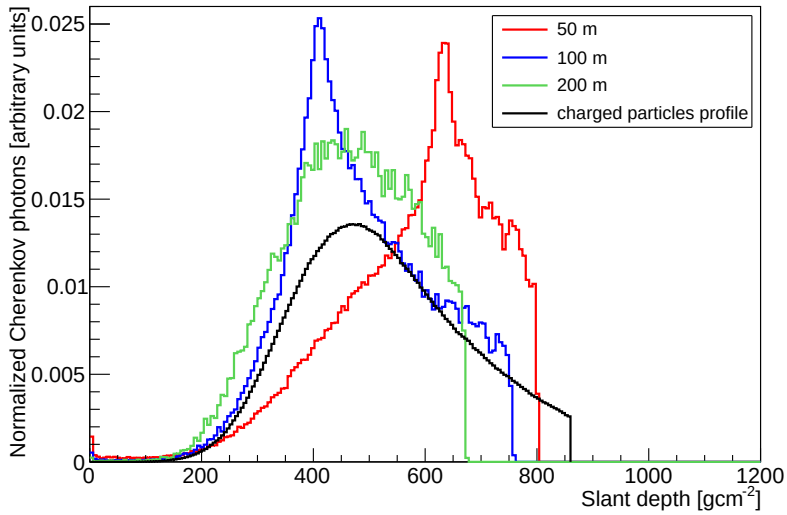

Figure 2.4: Longitudinal development of the number of Cherenkov photons seen by telescopes at 50, 100 and 200 m away from the shower core for gamma-ray shower with 100 TeV energy. The number of photons was normalized to an integral of 1.0 to allow comparison of the profiles.

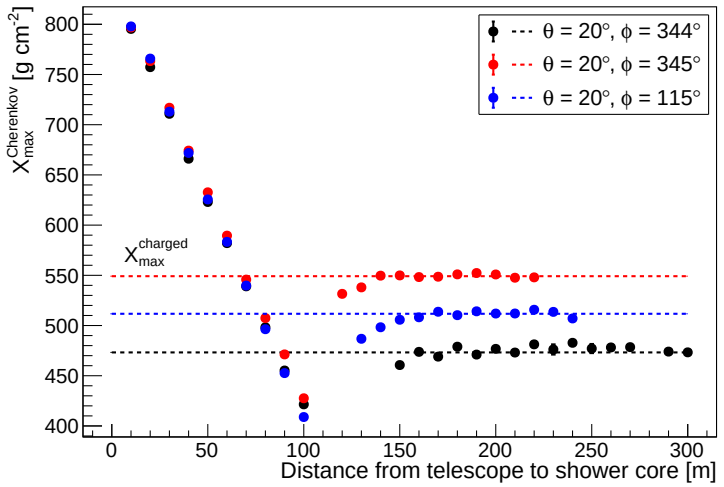

Figure 2.5: $X_{max}^{Cherenkov}$ as a function of the telescope position from the shower core. Each colour shows the simulation of one shower initiated by a gamma-ray primary with energy 100 TeV at 20° zenith angle and different azimuth angles as indicated in the legend. The field of view of the telescopes was set to 10°. $X_{max}^{charged}$ (dashed lines) is also shown for each shower.

For distances smaller than ≈100 m from the shower core, the amount of Cherenkov light reaching the telescopes is highly dominated by the Cherenkov pool. The combination of all factors listed above resulted in a linear decrease of $X_{max}^{Cherenkov}$ as a function of distance from the shower core up to 100 m. For distances larger than 150 m from the shower core, $X_{max}^{Cherenkov}$ does not depend on the distance and stays constant. The amount of Cherenkov light reaching these distances is dominated by scattering, and therefore the light does not keep the information of the Cherenkov angle of emission. A transition in the behaviour of $X_{max}^{Cherenkov}$ with distance from the shower core around (100-150) m is seen. Figure 2.6 shows the transition in detail. Two peaks are seen in this transition region: a narrow one corresponding to the Cherenkov light pool and a broader one corresponding to the scattered Cherenkov light. As a telescope gets farther from the shower core, the peak corresponding to the scattered light dominates. A similar trend of $X_{max}^{Cherenkov}$ as a function of distance from the shower core was seen irrespective of primary particle type and energy. The effect of the scattering at larger distances from the shower core is also visible in figure 2.2.

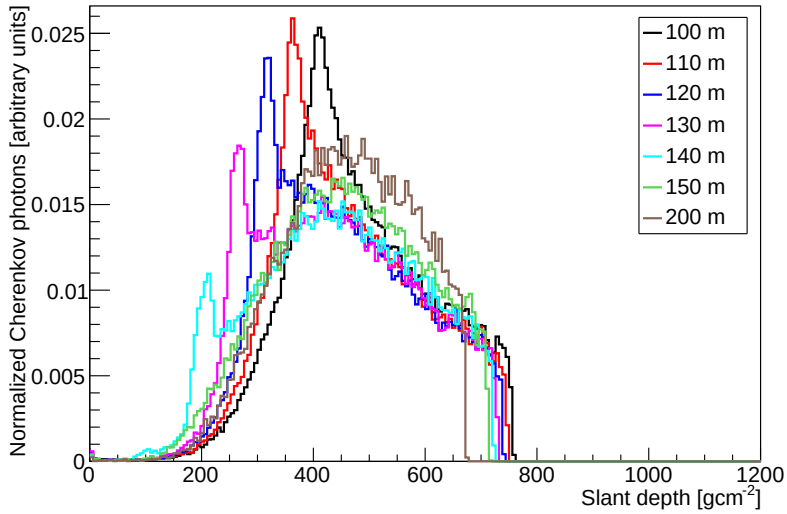

Figure 2.6: Longitudinal development of the number of Cherenkov photons seen by telescopes at distances 100, 110, 120, 130, 140 and 150 m from the shower core for a gamma ray shower with 100 TeV energy. The number of photons was normalized to an integral of 1.0 to allow comparison of the profiles.

2.3.1 Definition of the Apparent Cherenkov Maximum

The constant behaviour of the $X_{max}^{Cherenkov}$ for distances larger than 150 m from the shower core suggests a reconstruction procedure that is independent of telescope distance. Beyond that, note in figure 2.5 that the three events shown also suggest a correlation between the constant value of $X_{max}^{Cherenkov}$ and $X_{max}^{charged}$. The distance range from 120 to 150 m from the shower core is avoided because the exact transition between regimes depends on several aspects and because of the presence of two peaks in the longitudinal profile. Distances beyond 200 m from the shower core were also avoided due to large fluctuations and, in addition, the trigger efficiency of a shower beyond 200 m strongly depends on the configurations of the telescopes, and specific analysis should be done to extend the range beyond 200 m. The apparent Cherenkov depth of maximum ($X_{max}^{apparent}$) is defined here as the constant value of $X_{max}^{Cherenkov}$ for distances larger than 150 m and smaller than 200 m from the shower core and it is calculated by fitting a constant line.

Figure 2.7 shows the correlation of $X_{max}^{charged}$ and $X_{max}^{apparent}$. There is a linear correlation between $X_{max}^{charged}$ and $X_{max}^{apparent}$ for gamma-ray and proton primaries regardless of energy and for iron nuclei with energy above 30 TeV.

Even if iron nuclei do not have a linear behaviour for energies below 30 TeV, these showers were included in the calculations of the resolution below. In these figures, six telescopes with positions ranging from 150 to 200 m from the shower core were used in the fit to calculate $X_{max}^{apparent}$. The influence of the number of telescopes used in this fit will be studied in the next sections.

2.3.2 Reconstruction of $X_{max}^{charged}$ using $X_{max}^{apparent}$

A linear fit $X_{max}^{charged} = p_o + p_1 X_{max}^{apparent}$ was done for all simulated events at given fixed energies. In the first attempt, the three simulated primaries, gamma-rays, proton, and iron nuclei, were fit together as shown in figure 2.8a. The results of the fit for each energy are shown in table 2.1. These parametrizations can be used to reconstruct $X_{max}^{charged}$ from $X_{max}^{apparent}$ even when the primary particle is not known. The calculation was done for four hypothetical configurations: a) six telescopes at distances of 150 to 200 m from the shower core, b) three telescopes 150, 170 and 190 m from the shower core, one telescope at 150 m from the shower core and one telescope at 200 m from the shower core. The configuration with six telescopes represents a theoretical best-performance case.

The parameterization was used to reconstruct a value of $X_{max}^{charged}$ for all simulated events. The reconstructed $X_{max}^{charged}$ is named X_{max}^{rec} to differentiate it from the simulated true value $X_{max}^{charged}$. In other words, X_{max}^{rec} is calculated by the linear parametrization $X_{max}^{rec} = p_o + p_1 X_{max}^{apparent}$ with p_0 and p_1 given in table 2.1. Figure 2.8b shows the distribution of X_{max}^{rec} - $X_{max}^{charged}$ for all events. The resolution in the reconstruction of X_{max}^{rec} is taken as the standard deviation of the (X_{max}^{rec} - $X_{max}^{charged}$) distribution. Table 2.1 shows the values of the resolution for all cases. It is clear that the resolution improves with energy and also with the number of telescopes used to calculate $X_{max}^{apparent}$ (see figure 3.8).

2.4 Resolution in the reconstruction of $X_{max}^{charged}$ for different scenarios

As mentioned in the introduction, it is not the purpose of this study to analyse the details of detection and the specific reconstruction chain of each IACT observatory. Each collaboration makes use of different analysis techniques, and the specifications are only available for internal use. The method proposed here is, therefore, based on shower simulation and on perfect detection of Cherenkov light. The method is proven to be robust in a large energy range and to be independent of the previous knowledge

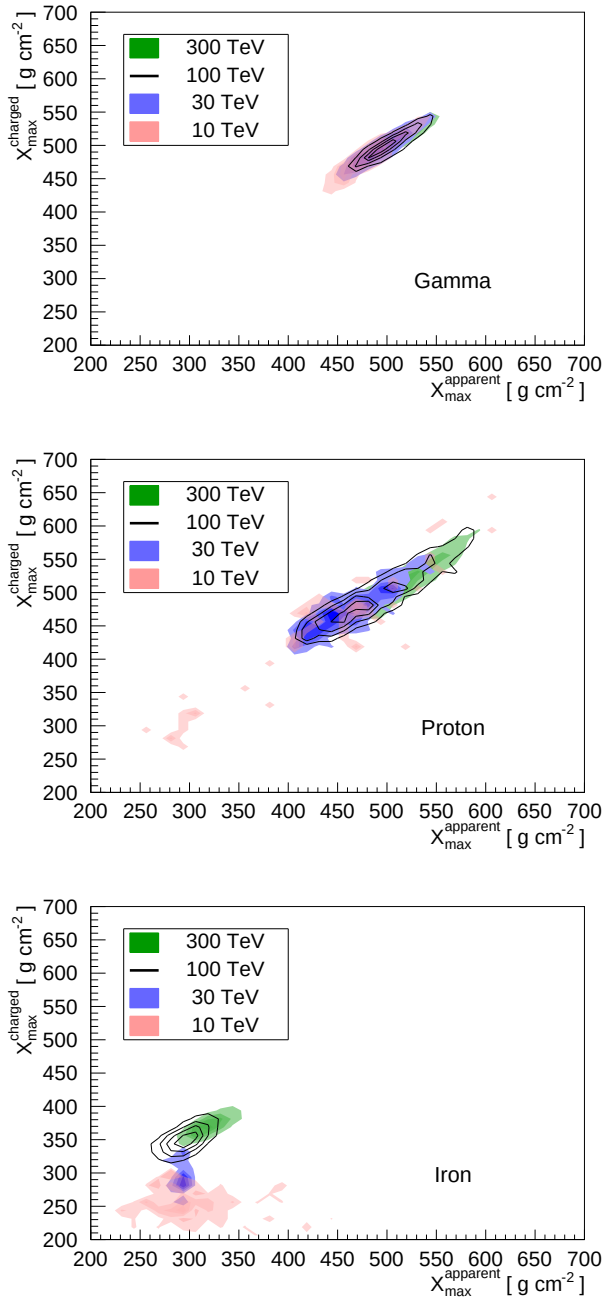

Figure 2.7: Correlation between $X_{max}^{charged}$ and $X_{max}^{apparent}$ for gamma-ray, proton and iron showers with energies of 10 TeV, 30 TeV, 100 TeV and 300 TeV at a zenith angle of 20°. Telescopes were considered to have 10° FOV.

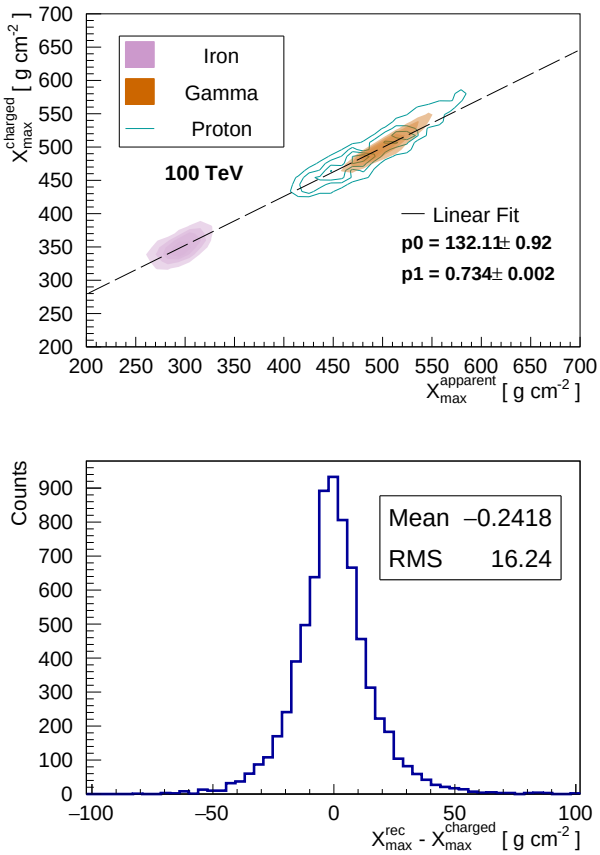

Figure 2.8: Top: $X_{max}^{charged}$ versus $X_{max}^{apparent}$ for gamma-ray, proton and iron nuclei initiated 100 TeV air showers. Six telescopes (150 to 200 m from the shower core) were used to calculate $X_{max}^{charged}$. Telescopes were considered to have 10° FOV. Bottom: Distribution of the difference between X_{max}^{rec} and $X_{max}^{Cherenkov}$.

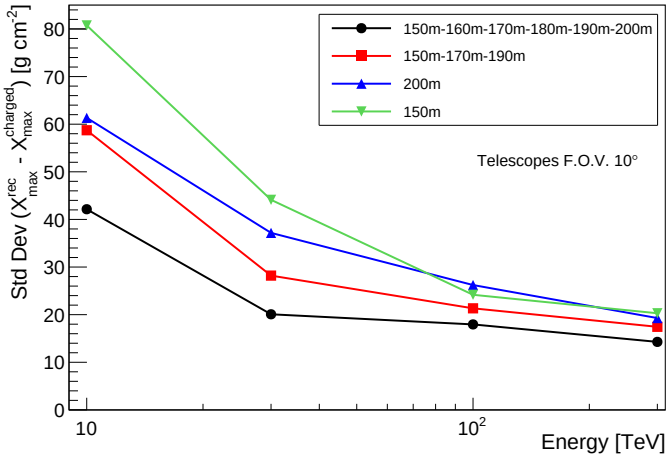

Figure 2.9: Resolution in the reconstruction of X_{max}^{rec} as a function of energy. Telescopes were considered to have 10° FOV. The four colours correspond to the configuration of telescopes used to fit $X_{max}^{apparent}$. All simulated primaries are used together.

E	150 to 200 m			150-170-190 m		
(TeV)	p_0	p_1	σ	p_0	p_1	σ
10	20.72	0.97	42.14	-8.99	1.02	58.73
30	16.84	0.97	20.08	8.75	0.99	28.20
100	132.11	0.73	16.24	102.9	0.80	21.33
300	90.47	0.82	14.28	78.78	0.85	17.45

E	200 m			150 m		
(TeV)	p_0	p_1	σ	p_0	p_1	σ
10	-7.63	1.02	61.33	-25.96	1.05	80.75
30	28.04	0.95	37.17	-3.54	1.02	44.12
100	99.36	0.80	26.22	118.3	0.78	24.17
300	58.47	0.88	19.28	135.9	0.74	20.29

Table 2.1: Results of the linear fit ($X_{max}^{rec} = p_o + p_1 X_{max}^{apparent}$) and the reconstruction resolution of X_{max}^{rec} (σ in g/cm^2). Gamma-ray, proton and iron nuclei primaries were used. Each column shows the configuration of telescopes used to calculate $X_{max}^{apparent}$. Telescopes were considered to have 10° FOV.

of the primary particle. In this section, the resolution of the method is calculated under the assumption of selected primary particles and different telescope FOV.

Minor aspects in the determination of the resolution of the method are discussed here. The energy determination of current IACT is around 15% for gamma-ray showers and around 25% for hadronic showers. Figure 2.7 shows that the parametrization proposed here does not depend on energy for all cases, except iron nuclei with energy below 30 TeV. Therefore an energy resolution of 25% has a negligible effect on the resolution of $X_{\rm max}^{\rm charged}$ determined here. The use of a specific hadronic interaction model (EPOS and FLUKA) also has minor ($< 5\%$) influence in IACT analysis [30]. The largest difference of $X_{\rm max}^{\rm charged}$ between models at this energy is 9 g/cm^2, still smaller than the resolution calculated in this paper, resulting in a minor source of systematic effect.

The method proposed here is based on the distance of the telescope from the shower core. Therefore, the resolution on the core position determination influences the resolution of $X_{\rm max}^{\rm charged}$ achieved by the method. Current IACTs are able to determine the core position with a resolution better than 30 m for the energies of this study. This figure will likely improve with CTA. If the core position is shifted with respect to its true position, the optimum range of 150-200 m from the shower core would also be shifted accordingly. However, this does not invalidate the ideas presented here. The key aspect of the method proposed here is that there is a range in distance from the shower core in which $X_{\rm max}^{\rm apparent}$ does not change. If a large array of telescopes is used in the measurement of the shower, the range of distances from the shower core for which $X_{\rm max}^{\rm apparent}$ is constant can be determined event-by-event from the data itself. For observatories with a small number of telescopes, the range of distances from the shower core for which $X_{\rm max}^{\rm apparent}$ is constant needs to be calculated, including the details of the analysis chain, especially the core position resolution. The effect for the observatories with a small number of telescopes should be a shift of the range of distances from the shower core for which $X_{\rm max}^{\rm apparent}$ is constant by a value smaller than the resolution in the determination of the core position.

2.4.1 Selected primary particles

In section 2.3.2, the parametrization of $X_{\rm max}^{\rm charged}$ and the resolution were calculated as if no information about the primary particle were known, and equal samples of gamma rays, proton and iron nuclei were considered in the simulations. However, as previously written, many analysis methods were developed to discriminate gamma-ray events from other primaries.

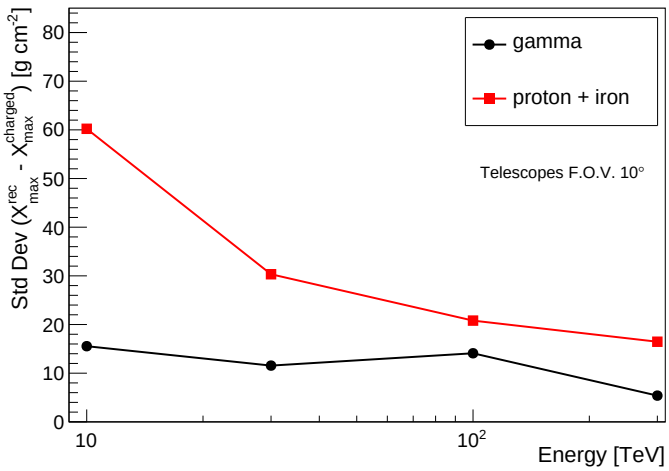

Figure 2.10: Resolution in the reconstruction of the X_{max}^{rec} as a function of the energy. Six telescopes (150 to 200 m from the shower core) were used to fit $X_{max}^{apparent}$. Telescopes were considered to have 10° FOV. The two curves correspond to gamma or proton and iron primary particles, as indicated in the legend.

The basic image analysis techniques (e.g. Hillas moments [31]) remove more than 99% of the background, keeping 50-70% gamma rays. Therefore, it is justifiable to consider parametrizations tuned for gamma-ray events separated from proton and iron nuclei showers.

The same procedure above was repeated. A fit of a linear function is done ($X_{max}^{rec} = p_o + p_1 X_{max}^{apparent}$) considering now two sets: a) gamma-ray and b) proton and iron nuclei events. Table 2.2 shows the results of the fit. Figure 2.10 shows the resolution for the two sets as a function of energy.

2.4.2 Telescope FOV

The telescope FOV is an important limitation for the determination of $X_{max}^{charged}$. Since $X_{max}^{apparent}$ should be within the FOV of the telescope in order to be measured, small FOV telescopes will have limited power of detection. The effect is illustrated in figure 2.11 in which $\langle X_{max}^{Cherenkov} \rangle$ is shown as a function of the telescope distance from the shower core. The average of $X_{max}^{Cherenkov}$ over all simulated events is shown to emphasize the effect by minimizing the fluctuations. It is clear that when the FOV gets smaller, the constancy of $X_{max}^{Cherenkov}$ with distance from the shower core is valid for a narrower interval of distance. In single showers, the effect is not so strong due to fluctuations.

E	gamma ray			proton + iron		
TeV	p_0	p_1	σ	p_0	p_1	σ
10	-39.88	1.09	15.55	22.28	0.97	60.22
30	-14.69	1.03	11.56	26.85	0.97	30.33
100	-65.81	1.13	14.09	121.5	0.76	20.81
300	21.72	0.95	5.39	105.5	0.80	16.46

Table 2.2: Results of the linear fit ($X_{max}^{rec} = p_o + p_1 X_{max}^{apparent}$) and the reconstruction resolution of X_{max}^{rec} (σ in g/cm^2). The analysis was done using two independent sets: a) gamma rays and b) proton and iron nuclei. Six telescopes were used to calculate $X_{max}^{apparent}$. Telescopes were considered to have 10° FOV.

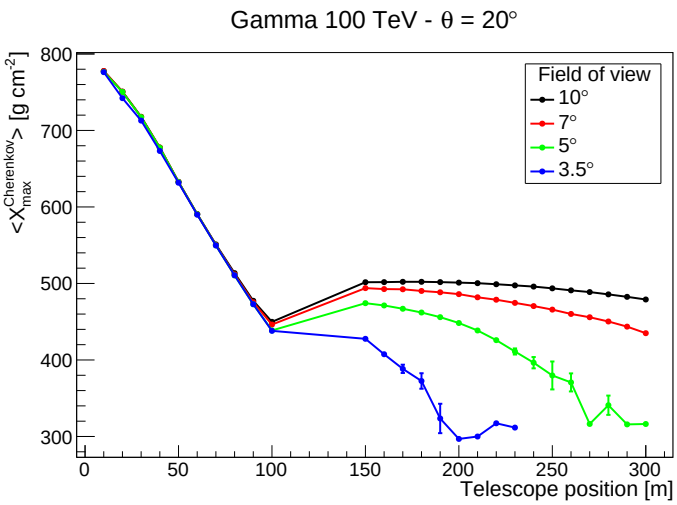

Figure 2.11: Mean $X_{max}^{Cherenkov}$ as a function of telescope distance from the shower core for different telescope fields of view. The different curves correspond to four different fields of view, as indicated in the legend.

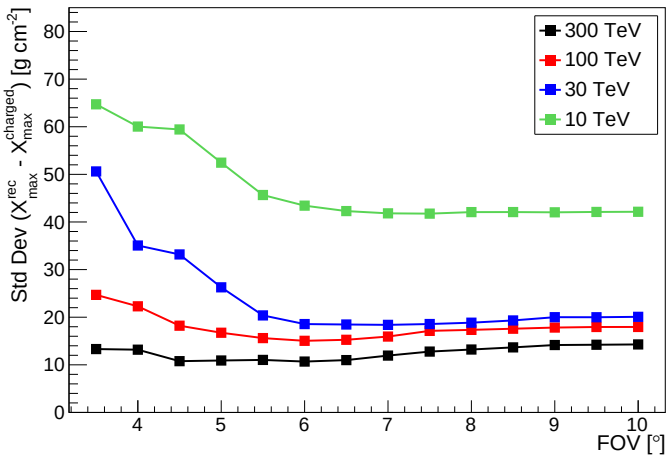

Figure 2.12: Resolution in the reconstruction of the X_{max}^{rec} as a function of telescope FOV. Six telescopes (150 to 200 m from the shower core) were used to fit $X_{max}^{apparent}$. The four curves correspond to different primary energies, as indicated in the legend. All simulated primaries are used together.

The analysis procedure discussed above was repeated for different telescope fields of view ranging from 3.5° to 10°. For each FOV, a new $X_{max}^{Cherenkov}$ versus $X_{max}^{apparent}$ correlation was done, and a new fit was performed. In this way, the corresponding X_{max}^{rec} for each FOV was calculated. Figure 2.12 shows the resolution of the X_{max}^{rec} reconstruction as a function of FOV. The resolution curve shows an artificial improvement for FOV values smaller than $\approx 4.5^{\circ}$ which is not related to an improvement of the technique. For small FOV values ($< 4.5^{\circ}$), the telescopes start to show showers with small $X_{max}^{charged}$ (shower developing high in the atmosphere). The spread of the measured $X_{max}^{charged}$ is smaller, the calibration curve is more precise, and the resolution seems to get better. The calculated resolution gets artificially better with decreasing FOV because the telescopes measure a sample of showers with less spread in $X_{max}^{charged}$.

2.5 Conclusions

A method to reconstruct $X_{max}^{charged}$ using atmospheric Cherenkov telescope data was presented. The dependency of the Cherenkov signal on the distance of the telescope from the shower core was studied. The depth at which telescopes measure the maximum number of Cherenkov photons

($X_{max}^{Cherenkov}$) depends on the distance of the telescope from the shower core up to (120-150 m). For distances larger than 150 m and smaller than 200 m from the shower core, $X_{max}^{Cherenkov}$ stays constant with distance and a reconstruction method is proposed using the data detected by these telescopes.

A new parameter, $X_{max}^{apparent}$, is defined from the linear fit of the dependence of $X_{max}^{Cherenkov}$ with distance. $X_{max}^{apparent}$ is the average constant value of $X_{max}^{Cherenkov}$ in the distance range of (150-200) m from the shower core. $X_{max}^{apparent}$ is shown to be correlated with $X_{max}^{charged}$, and this correlation is proposed as a novel reconstruction method.

The resolution of the method to reconstruct $X_{max}^{charged}$ has been studied as a function of energy, primary particle type, number of telescopes and telescope FOV. Figure 2.7 shows that the parametrization proposed here does not depend on energy for all cases except iron nuclei with energy below 30ÎTeV. The resolution improves with energy starting from 60 g/cm^2 at 10 TeV and reaching 15 g/cm^2 at 300 TeV, even if the primary particle is not known. Two sets of primary particles are considered: a) gamma rays and b) proton and iron nuclei. The method shows better resolution for the gamma-ray events 10-20 g/cm^2, whereas proton and iron nuclei have 20-60 g/cm^2, depending on energy. The number of telescopes used to fit $X_{max}^{apparent}$ was considered to be a maximum of six and a minimum of one at selected distances from the shower core. The best resolution is achieved when six telescopes are used. If only one telescope is used, the resolution worsens by a maximum of 40 g/cm^2 in the worst case. The resolution also improves as a function of increasing telescope FOV. The dependence with FOV is more important at lower energies (10 and 30 TeV) than at high energies (100 - 300 TeV).

The parametrization proposed here could be tuned to each telescope type and the telescope array configuration. It is expected that a fine-tuning of the parametrization to the characteristics of each observatory will improve the resolution of $X_{max}^{charged}$ predicted here. The $X_{max}^{charged}$ distributions of proton and iron nuclei at 100 TeV have mean 502 and 342 g/cm^2, respectively, differing from each other of 160 g/cm^2. The resolution achieved by the method proposed here is, in all cases, much smaller than the differences between the means, suggesting a new possibility to study cosmic rays with IACTs using $X_{max}^{charged}$ distributions.

Acknowledgments

AGDG, LBA, and VdS acknowledge FAPESP Project 2015/15897-1. This study was financed in part by the Coordenação de Aperfeiçoamento de Pessoal de Nível Superior - Brasil (CAPES) - Finance Code 001. The authors acknowledge the National Laboratory for Scientific Computing (LNCC/MCTI, Brazil) for providing HPC resources of the SDumont supercomputer (http://sdumont.lncc.br). VdS received support from UCLA during his visit in 2017 and acknowledges CNPq.

Bibliography

[1] https://www.mpi-hd.mpg.de/hfm/HESS/, .

[2] http://www.magic.iac.es/, .

[3] http://veritas.sao.arizona.edu/, .

[4] C.-C. Lu and for the H.E.S.S. Collaboration. Improving the H.E.S.S. angular resolution using the disp method. 2013. , arXiv:1310.1200.

[5] J. Aleksić, S. Ansoldi, L.A. Antonelli, et al. The major upgrade of the MAGIC telescopes, Part II: A performance study using observations of the crab nebula. *Astroparticle Physics*, 72:76 – 94, 2016. ISSN 0927-6505. doi: https://doi.org/10.1016/j.astropartphys.2015.02.005. URL http://www.sciencedirect.com/science/article/pii/S0927650515000316.

[6] The VERITAS Collaboration. VERITAS specifications, 2023. URL https://veritas.sao.arizona.edu/about-veritas/veritas-specifications. Accessed = 2023-10-25.

[7] http://tevcat.uchicago.edu/, .

[8] B.S. Acharya, M. Actis, T. Aghajani, et al. Introducing the cta concept. *Astroparticle Physics*, 43:3 – 18, 2013. ISSN 0927-6505. doi: https://doi.org/10.1016/j.astropartphys.2013.01.007. URL http://www.sciencedirect.com/science/article/pii/S0927650513000169. Seeing the High-Energy Universe with the Cherenkov Telescope Array - The Science Explored with the CTA.

[9] F. Aharonian, A. G. Akhperjanian, U. Barres de Almeida, et al. Energy spectrum of cosmic-ray electrons at TeV energies. *Phys. Rev. Lett.*, 101:261104, Dec 2008. doi: 10.1103/PhysRevLett.101.261104. URL https://link.aps.org/doi/10.1103/PhysRevLett.101.261104.

[10] D. Borla Tridon, P. Colin, L. Cossio, et al. Measurement of the cosmic electron plus positron spectrum with the MAGIC telescopes. *32nd ICRC*, 2011. , arXiv:1110.4008.

[11] A. Archer, W. Benbow, R. Bird, et al. Measurement of cosmic-ray electrons at TeV energies by VERITAS. *Phys. Rev. D*, 98:062004, Sep 2018. doi: 10.1103/PhysRevD.98.062004. URL https://link.aps.org/doi/10.1103/PhysRevD.98.062004.

[12] F. Aharonian, A. G. Akhperjanian, J. A. Barrio, et al. Cosmic ray proton spectrum determined with the imaging atmospheric cherenkov technique. *Phys. Rev. D*, 59:092003, Mar 1999. doi: 10.1103/PhysRevD.59.092003. URL https://link.aps.org/doi/10.1103/PhysRevD.59.092003.

[13] A. Archer, W. Benbow, R. Bird, et al. Measurement of the iron spectrum in cosmic rays by VERITAS. *Phys. Rev. D*, 98:022009, Jul 2018. doi: 10.1103/PhysRevD.98.022009. URL https://link.aps.org/doi/10.1103/PhysRevD.98.022009.

[14] F. Aharonian, A. G. Akhperjanian, A. R. Bazer-Bachi, et al. First ground-based measurement of atmospheric cherenkov light from cosmic rays. *Phys. Rev. D*, 75:042004, Feb 2007. doi: 10.1103/PhysRevD.75.042004. URL https://link.aps.org/doi/10.1103/PhysRevD.75.042004.

[15] M. Aguilar, D. Aisa, B. Alpat, et al. Precision measurement of the proton flux in primary cosmic rays from rigidity 1 GV to 1.8 TV with the Alpha Magnetic Spectrometer on the International Space Station. *Phys. Rev. Lett.*, 114:171103, Apr 2015. doi: 10.1103/PhysRevLett.114.171103. URL https://link.aps.org/doi/10.1103/PhysRevLett.114.171103.

[16] The HEGRA-Collaboration. Energy spectrum and chemical composition of cosmic rays between 0.3 and 10 pev determined from the cherenkov-light and charged-particle distributions in air showers. *Astronomy & Astrophysics*, 359:682–694, 2000.

[17] D.B Kieda, S.P Swordy, and S.P Wakely. A high resolution method for measuring cosmic ray composition beyond 10 tev. *Astroparticle Physics*, 15(3):287 – 303, 2001. ISSN 0927-6505. doi: https://doi.org/10.1016/S0927-6505(00)00159-6. URL http://www.sciencedirect.com/science/article/pii/S0927650500001596.

[18] R.D. Parsons and J.A. Hinton. A monte carlo template based analysis for air-cherenkov arrays. *Astroparticle Physics*, 56:26 – 34, 2014. ISSN 0927-6505. doi: https://doi.org/10.1016/j.astropartphys.2014.03.002. URL http://www.sciencedirect.com/science/article/pii/S0927650514000231.

[19] J. Matthews. A Heitler model of extensive air showers. *Astroparticle Physics*, 22(5-6):387 – 397, 2005. ISSN

0927-6505. doi: DOI:10.1016/j.astropartphys.2004.09.003. URL http://www.sciencedirect.com/science/article/B6TJ1-4DN0YT7-1/2/837bfde7279edb347fd6f60f21a9b793.

[20] G. L. Cassiday, R. Cooper, S. C. Corbato, et al. Measurements of Cosmic-Ray Air Shower Development at Energies above 10^{17} eV. *Astrophysical Journal*, 356:669, Jun 1990. doi: 10.1086/168873.

[21] R. U. Abbasi, T. Abu-Zayyad, M. Al-Seady, et al. Indications of proton-dominated cosmic-ray composition above 1.6 EeV. *Phys. Rev. Lett.*, 104:161101, Apr 2010. doi: 10.1103/PhysRevLett.104.161101. URL https://link.aps.org/doi/10.1103/PhysRevLett.104.161101.

[22] A. Aab, P. Abreu, M. Aglietta, et al. Depth of maximum of air-shower profiles at the Pierre Auger Observatory. i. measurements at energies above $10^{17.8}$ eV. *Phys. Rev. D*, 90:122005, Dec 2014. doi: 10.1103/PhysRevD.90.122005. URL https://link.aps.org/doi/10.1103/PhysRevD.90.122005.

[23] M. Hillas. *J. Phys. G : Nucl. Phys.*, 8:1475–1492, 1982.

[24] D. Heck, J. Knapp, J.N. Capdevielle, et al. A monte-carlo code to simulate extensive air showers - report FZKA 6019. Technical report, Forschungszentrum Karlsruhe, www-ik.fzk.de/∼heck/corsika, 1998.

[25] T Pierog, Iu. Karpenko, J M Katzy, et al. EPOS LHC: Test of collective hadronization with data measured at the CERN Large Hadron Collider. *Phys. Rev. C*, 92:034906, 2015. doi: 10.1103/PhysRevC.92.034906.

[26] Giuseppe Battistoni, Till Boehlen, Francesco Cerutti, et al. Overview of the FLUKA code. *Annals of Nuclear Energy*, 82:10 – 18, 2015. ISSN 0306-4549. doi: https://doi.org/10.1016/j.anucene.2014.11.007. URL http://www.sciencedirect.com/science/article/pii/S0306454914005878. Joint International Conference on Supercomputing in Nuclear Applications and Monte Carlo 2013, SNA + MC 2013. Pluri- and Trans-disciplinarity, Towards New Modeling and Numerical Simulation Paradigms.

[27] T. K. Gaisser and A. M. Hillas. Reliability of the method of constant intensity cuts for reconstructing the average development of vertical showers. In 15^{nd} *Int. Cosmic Ray Conf.*, volume 8, pages 353–356, Plovdiv (Bulgaria), 1977.

[28] Hon. J.W. Strutt. Lviii. on the scattering of light by small particles. *The London, Edinburgh, and Dublin Philosophical Magazine and Journal of Science*, 41(275):447–454, 1871. doi: 10.1080/14786447108640507. URL https://doi.org/10.1080/14786447108640507.

[29] Gustav Mie. Beiträge zur optik trüber medien, speziell kolloidaler metallösungen. *Annalen der Physik*, 330(3):377–445, 1908. doi: 10.1002/andp.19083300302. URL https://onlinelibrary.wiley.com/doi/abs/10.1002/andp.19083300302.

[30] The CTA Consortium, M. Actis, G. Agnetta, et al. Design concepts for the Cherenkov Telescope Array CTA: an advanced facility for ground-based high-energy gamma-ray astronomy. *Experimental Astronomy*, 32(3):193–316, November 2011. ISSN 0922-6435, 1572-9508. doi: 10.1007/s10686-011-9247-0. URL http://www.springerlink.com/index/10.1007/s10686-011-9247-0.

[31] M. Hillas. Proceedings of the International Cosmic Rays Conference. 3:445, 1985.

3. Cosmic-ray measurements with an array of Cherenkov telescopes using reconstruction of longitudinal profiles of air showers

Andrés G. Delgado Giler, Vitor de Souza,
Published in Astroparticle Physics
doi: 10.1016/j.astropartphys.2023.102817

ABSTRACT

We present a method to reconstruct the longitudinal profile of electrons in showers using Cherenkov telescopes. We show how the Cherenkov light collected by an array of telescopes can be transformed into the number of electrons as a function of atmospheric depth. This method is validated using air shower and simplified telescope simulations. The reconstruction of the depth in which the shower has the maximum number of electrons (X_{max}) opens the possibility of cosmic ray composition studies with Cherenkov telescopes in the energy range from 10 to 100 TeV.

3.1 Introduction

Cherenkov telescopes are mainly used for gamma-ray astronomy. Non-gamma-ray events have not been fully analysed by standard analysis chains. Exceptions are the study of electron [1, 2, 3] and extreme (proton and iron) nuclei primaries [4, 5, 6]. Besides those, Cherenkov telescopes measure at least 1000 times more cosmic rays, including all nuclei, than gamma-ray showers.

This paper proposes a technique to reconstruct the longitudinal profile of electrons in the shower using the signal detected by Cherenkov telescopes. The reconstruction of the longitudinal profile of electrons in the shower could be applied to better understand the shower development in comparison to the Monte Carlo simulation and also to improve reconstruction chains. We focus on the possibility of reconstructing the depth in which showers have the maximum number of electrons (X_{max}) and its use to determine the primary particle type.

Deep learning models to analyze data from arrays of imaging atmospheric Cherenkov telescopes (IACTs) are under active development [7]. Previous papers based on the lateral distribution of Cherenkov light produced in the shower proposed methods to study the cosmic ray composition using IACTs [8, 9]. The determination of the X_{max} was also studied in references [10, 11]. In these studies, a complex full reconstruction of the shower is implemented via a fit of the camera image or deep learning techniques. All parameters are reconstructed together, including X_{max}. The complexity of these methods increases significantly with the number of telescopes in the analysis. They also depend on large sets of simulated showers. In reference [10], an X_{max} resolution of 30 g/cm^2 for energies below 1 TeV was achieved.

In a previous publication [12], we showed how to use telescopes outside the Cherenkov beam (> 150 m) to reconstruct X_{max}. In this paper, we make use of the parametrization of the angular distribution function of Cherenkov photons [13] to reconstruct the longitudinal profile and calculate X_{max} using telescopes at all distances from the shower axis. This is one of the key differences between the method proposed here and previous publications. The new method allows a more direct measurement of the shower properties and the use of telescopes with larger signals and, therefore higher probability of trigger. The method proposed here also significantly reduces the complexity of the analysis by focusing on only one parameter (X_{max}), which might lead to computational advantages when analyzing multiple telescopes simultaneously.

In section 3.2, the shower and the telescope simulation are explained. In section 3.3, we present the method to reconstruct the longitudinal profile of electrons and the fitting to calculate its maximum. In section 3.4, the reconstructed shower maximum X_{max} and the resolution are discussed; and finally, in section 3.5, the conclusions and final remarks are given.

3.2 Simulation of the Cherenkov light reaching the telescopes

We simulated air showers using the CORSIKA 7.6900 package [14]. We considered vertical showers generated by gamma, proton and iron nuclei with energy of 10, 30 and 100 TeV. QGSJET II-04 [15] and URQMD [16] were used for high and low-energy hadronic interactions. The hadronic interaction models do not influence the reconstruction of X_{max}, which is the focus of this paper. The hadronic interaction models influence the interpretation of X_{max} as composition. For each energy and primary particle, 10000 events were simulated. The threshold energies for hadrons, muons, electrons and photons were set to 0.3, 0.01, 0.020, and 0.020 GeV, respectively. The U.S. standard atmosphere model was used.

Cherenkov photons were produced in the simulation. Photons were emitted in bunch size 5 with a wavelength between 200 and 700 nm. The emission angle of the Cherenkov light is taken to be wavelength-independent, and photons are propagated until sea level. An array in the shape of a North-South cross with 24 telescopes delimited by spheres with 2.15 m of radius spaced 40 m apart from each other. All photons reaching the detectors have direction and momentum recorded.

A simplified simulation of the telescope was considered taking into account the field of view of 10.5 degrees and the camera pixelization with 0.19 degrees hexagonal pixels. Pixels were considered to be triggered if the number of collected photons is three times larger than the night sky background of 2.6×10^8 photons per sr s m^2. The sampling rate was taken to be 500 MHz. The optical efficiency of the telescopes was assumed to be 0.1 p.e./photon. An example of a simulated image is shown in figure 3.1.

3.3 Reconstruction of the longitudinal profile

The shower plane is defined by the shower axis and the vector pointing to the telescope from the impact point of the shower axis. Each pixel intersects the shower plane, defining a region. In a good approximation,

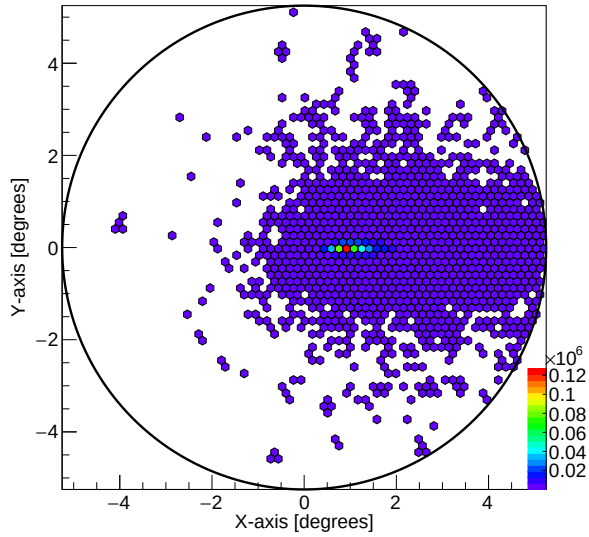

Figure 3.1: Simplified simulation of a camera image generated by a vertical proton of 100 TeV. The image corresponds to the telescope at 120 m from the shower axis. Only pixels satisfying the trigger condition are plotted.

all photons detected by one pixel can be considered to be generated in this region. Figure 3.2 shows the number of photons in each region defined by the pixels shown in figure 3.1 and its subsequent (right panel) projection into the shower axis to find the longitudinal profile of Cherenkov photons. A constant density of photons was considered inside each pixel, and the photons were distributed into depth bins uniformly. For details about the projection, see reference [12].

Given that the Cherenkov emission is highly beamed, the Cherenkov photons emitted at a given depth can only be measured by telescopes in specific positions. In other words, each telescope samples different parts of the longitudinal development of the shower as shown in figure 3.3 for telescopes at 80, 120, 160 and 200 m away from the shower core and as carefully discussed in reference [12].

According to the model developed in reference [13], the number of Cherenkov photons emitted in a given angle, θ, with the shower axis by the particles in a shower can be written as

$$\frac{\mathrm{d}^2 N_\gamma}{\mathrm{d}\theta\, \mathrm{d}X}(\theta, s, h) = \frac{1}{\pi}\, N_\mathrm{e}(s) \times \sin\theta \times I(\theta, h) \times K(\theta, s, h) \tag{3.1}$$

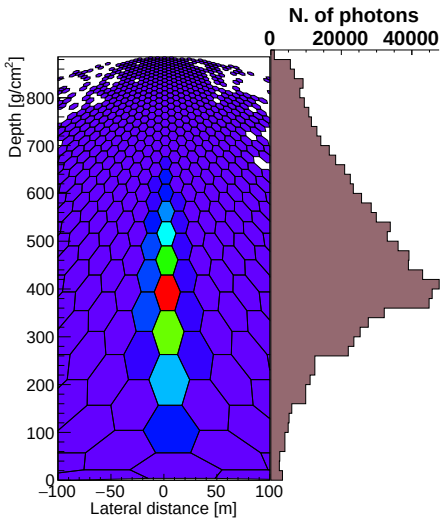

Figure 3.2: Projected pixels correspond to figure 3.1. Only pixels that satisfy good projection are plotted. On the right side is shown the number of photons summed along the longitudinal axis.

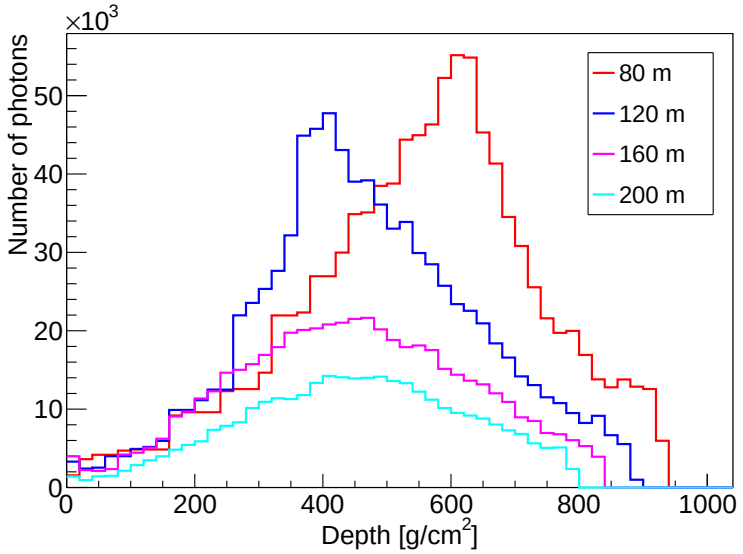

Figure 3.3: Cherenkov photon profiles of the same air shower event initiated by a proton of 100 TeV. Each curve represents the profile observed by telescopes at different distances from the impact point.

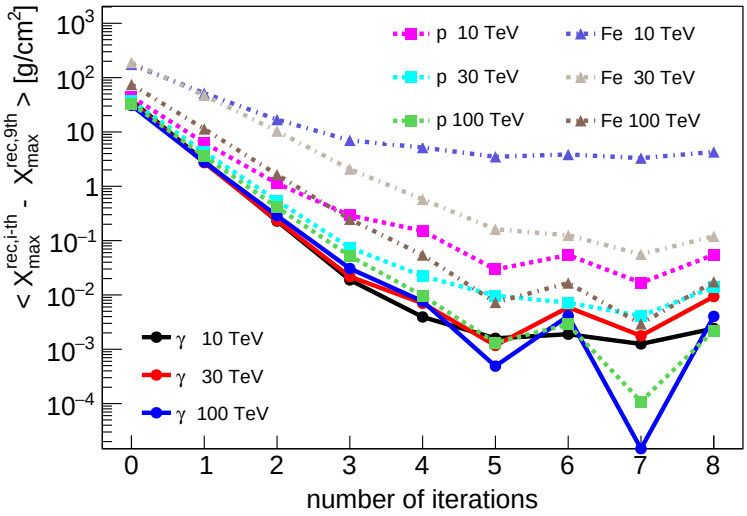

Figure 3.4: Mean value of X^{rec}_{max} difference at each step of iteration with respect to the X^{rec}_{max} at 9th iteration.

where s is age[1], h height and N_e the number of electrons in the shower. $I(\theta, h)$ and $K(\theta, s, h)$ are functions describing the angular emission of Cherenkov photons for which a parametrization is given in reference [13]. This parametrization describes quite well the behaviour of the Cherenkov light distribution at short distances with respect to the shower core.

Given the position of the telescope, equation 3.1 allows us to calculate the number of electrons corresponding to the number of photons detected by each pixel. The calculation must be done in an iterative procedure, given the dependence on age. We start the calculation considering $s = 1$ for all pixels and find the corresponding longitudinal profile. We find the maximum of this longitudinal profile and recalculate the longitudinal profile using the new estimate of age. The procedure is repeated until convergence. Figure 3.4 shows that after the 5th iteration, the reconstructed depth in which the shower has the largest number of electrons, X^{rec}_{max} , is stable within less than 1 g/cm^2.

Figure 3.5 shows the longitudinal profile of electrons reconstructed using the procedure explained above. The number of photons simulated in each pixel of the 24 telescopes was projected into the shower plane and then projected into the shower axis. The longitudinal profile of Cherenkov photons was transformed into the number of electrons using equation 3.1.

[1] $s = 3X/(X + 2X_{max})$

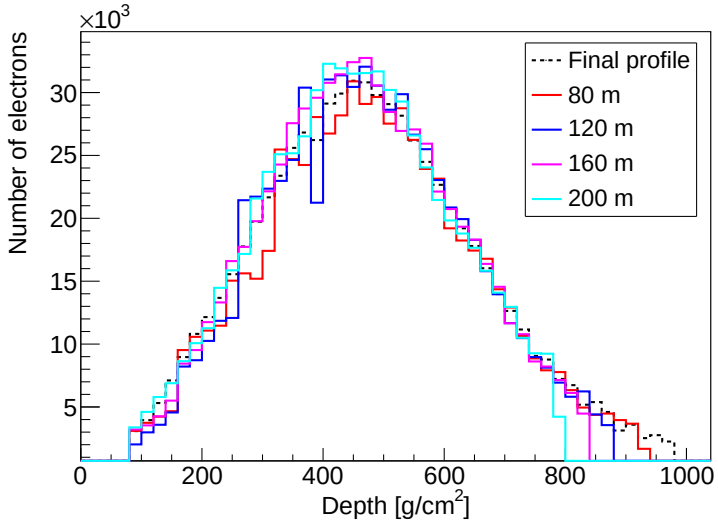

Figure 3.5: Electron shower profiles reconstructed at 9th iteration from Cherenkov photons profiles for telescopes at different distances. The final profile is the weighted average not only of the profiles shown but of the complete telescope configuration.

The contribution of the telescopes at 80, 120, 160 and 200 m away from the shower core are shown for comparison; however, the final reconstructed longitudinal electron profile includes the signal of all 24 telescopes in the simulation. X_{max}^{rec} is calculated by fitting the reconstructed profile with a second-order polynomial ranging ± 100 g/cm^2 around the peak as shown in figure 3.6. The agreement between the reconstructed and simulated longitudinal electron profile is remarkable, as well as the simulated (X_{max}^{sim}) and reconstructed shower maximum. Because the telescopes point to the zenith and have 10.5 degrees of field of view, they don't detect Cherenkov photons generated deep in the atmosphere, causing the reconstructed profile to have systematically fewer particles than the simulated profile at large depths.

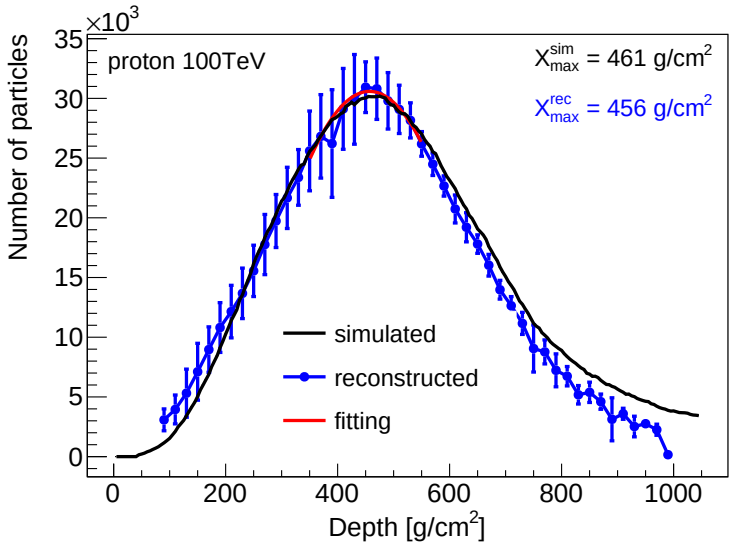

Figure 3.6: Example of the simulated (black) and the corresponding reconstructed profile (blue). This event corresponds to an air shower initiated by a vertical proton of 100 TeV. The red curve is the second-degree polynomial fitting of the reconstructed profile.

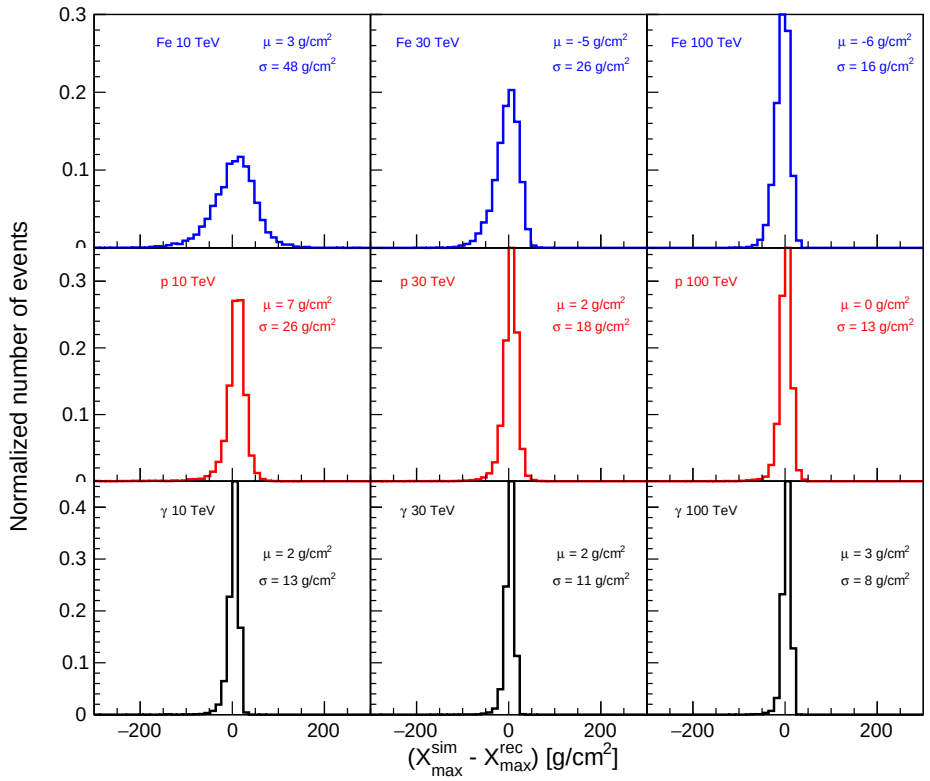

Figure 3.7: Distributions of $X_{max}^{sim} - X_{max}^{rec}$ for all primary particles and energies.

3.4 Results

Figure 3.7 shows the distribution of $X_{max}^{sim} - X_{max}^{rec}$ for all primary particles and energies considered here. The distributions are narrow, showing the quality of the method. The resolution of the reconstruction is taken as the standard deviation of these distributions, and they are shown in figure 3.8.

For gamma-ray showers, the resolution is around 10 g/cm^2 along the energy range. A deterioration of the resolution can be seen for cosmic ray events at low energies. In the best case at 100 TeV, the resolution for cosmic ray showers is below 16 g/cm^2.

The arrival direction accuracy (angular resolution) is probably the most important source of systematic uncertainty for this method. If the arrival direction is badly reconstructed, the projection of each pixel onto the shower plane would be systematically misplaced, affecting the reconstruction of the longitudinal profile and, therefore, of X_{max}. IACT

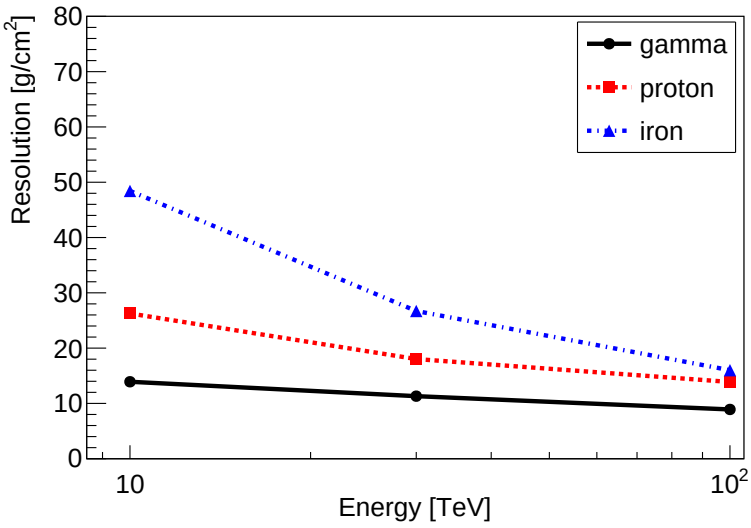

Figure 3.8: Resolution of the reconstruction, defined as the standard deviation of the distribution of $X^{sim}_{max} - X^{rec}_{max}$, as a function of the primary energy for three different kinds of air showers.

angular resolution is typically 0.1 degrees, which is expected to be smaller than 0.05 degrees for CTA [17]. We calculated the resolution in X_{max} for 100 TeV proton events, assuming that the reconstructed shower direction is 0.1 degrees apart from the simulated shower direction. The X_{max} resolution worsens only by 1 g/cm^2. The second-degree polynomial fitting also provides the maximum number of reconstructed particles N^{rec}_{max} observed at depth X^{rec}_{max} , which is a reasonable energy estimator of the primary particle. Table 3.1 contains the mean and standard deviation values of the $(N^{sim}_{max} - N^{rec}_{max})/N^{sim}_{max}$ distribution for each particle and energy, where N^{sim}_{max} is the maximum number of simulated particles at X^{sim}_{max}.

Energy	Gamma		Proton		Iron	
	mean	std dev	mean	std dev	mean	std dev
10 TeV	0.0399	0.0641	0.1401	0.1173	0.7119	0.0621
30 TeV	0.0000	0.0617	0.0671	0.0916	0.5152	0.0546
100 TeV	-0.0413	0.0522	0.0119	0.0729	0.3237	0.0458

Table 3.1: Mean and standard deviation values for $(N^{sim}_{max} - N^{rec}_{max})/N^{sim}_{max}$ distribution.

3.5 Conclusions

In this paper, a novel method for the reconstruction of longitudinal air shower profiles using Cherenkov telescopes was presented. Using a shower and simplified detector simulations, we have shown that the X_{max} parameter can be reliably estimated for each event. The resolution in the X_{max} reconstruction, which was defined as the standard deviation of the difference distribution between X_{max} simulated and X_{max} reconstructed, was determined as a function of energy and type of primary particle. For all primaries, the resolution improves with energy. Moreover, the resolution is below 16 g/cm^2 at 100 TeV for all studied cases. The resolution is worse for heavier nuclei, which might indicate the need for a two-dimensional analysis for these primaries. The resolution achieved here makes it possible to study cosmic ray composition with Cherenkov telescopes.

Besides reconstructing X_{max}, the method proposed here reconstructs the longitudinal development of electrons in the shower. This feature of the method is going to be developed in a future study towards reconstructing the energy of the shower. As it is widely used in the cosmic ray data analysis [18, 19], fitting the entire longitudinal development with a Gaisser-Hillas fuction [20] leads to a very accurate and bias-free reconstruction of the shower energy.

The method developed here must be optimized for the telescope type and array configuration. The calculation presented in this paper based on simplified telescope simulations would imply that the X_{max} resolution overestimates the real X_{max} resolution to be achieved by the method. Exposure and acceptance estimations and systematic uncertainties should be considered when analysing real data towards composition studies. Moreover, the simplicity of the method proposed here allows the use of the data from dozens of telescopes without the computational expenses required by template or deep learning techniques. It is expected that a fine-tuning of the method to the characteristics of each observatory will improve the resolution of X_{max} predicted here. The X_{max} resolution of gamma-rays, proton and iron nuclei at 100 TeV are 8, 13, 16 g/cm^2, respectively. The N_{max} resolution (standard deviation) of gamma-rays, proton and iron nuclei at 100 TeV are 5.22%, 7.29% and 4.58%, respectively. The X_{max} resolutions are much smaller than the differences between the means of X_{max} distributions, suggesting a real possibility of studying cosmic rays with IACTs as complementary measurements together with other well-developed methods. Also, these measurements would allow synergy and complementarity with information from space instruments that lack data.

3.6 Acknowledgments

Authors acknowledge FAPESP Project 2015/15897-1 and the National Laboratory for Scientific Computing (LNCC/MCTI, Brazil) for providing HPC resources of the SDumont supercomputer (http://sdumont.lncc.br). VdS acknowledges CNPq. This study was financed in part by the Coordenação de Aperfeiçoamento de Pessoal de Nível Superior - Brasil (CAPES) - Finance Code 001. The authors thank Luan B. Arbeletche for fruitful discussions.

Bibliography

[1] F. Aharonian et al. The energy spectrum of cosmic-ray electrons at TeV energies. *Phys. Rev. Lett.*, 101:261104, 2008. doi: 10.1103/PhysRevLett.101.261104.

[2] Daniela Borla Tridon. Measurement of the cosmic electron spectrum with the MAGIC telescopes. In *International Cosmic Ray Conference*, volume 6 of *International Cosmic Ray Conference*, page 47, January 2011. doi: 10.7529/ICRC2011/V06/0680.

[3] David Staszak. A Cosmic-ray Electron Spectrum with VERITAS. *PoS*, ICRC2015:411, 2016. doi: 10.22323/1.236.0411.

[4] A. Archer et al. Measurement of the Iron Spectrum in Cosmic Rays by VERITAS. *Phys. Rev. D*, 98(2):022009, 2018. doi: 10.1103/PhysRevD.98.022009.

[5] R. Bühler. Energy spectrum of cosmic iron nuclei measured by H.E.S.S. In *International Cosmic Ray Conference*, volume 2 of *International Cosmic Ray Conference*, pages 15–18, January 2008.

[6] David Jankowsky. *Measurement of the Cosmic Ray Proton Spectrum with H.E.S.S. and Characterization of the TARGET ASICs for the CTA*. doctoralthesis, Friedrich-Alexander-Universität Erlangen-Nürnberg (FAU), 2020.

[7] Ari Brill, Bryan Kim, Daniel Nieto, et al. CTLearn: Deep learning for imaging atmospheric Cherenkov telescopes event reconstruction, March 2021. URL `https://doi.org/10.5281/zenodo.4576196`.

[8] F. Arqueros et al. Energy spectrum and chemical composition of cosmic rays between 0.3-PeV and 10-PeV determined from the Cherenkov light and charged particle distributions in air showers. *Astron. Astrophys.*, 359:682–694, 2000.

[9] S. P. Swordy and D. B. Kieda. Elemental composition of cosmic rays near the knee by multiparameter measurements of air showers. *Astropart. Phys.*, 13:137–150, 2000. doi: 10.1016/S0927-6505(99)00117-6.

[10] R.D. Parsons and J.A. Hinton. A monte carlo template based analysis for air-cherenkov arrays. *Astroparticle Physics*, 56:26–34, 2014. ISSN 0927-6505. doi: https://doi.org/10.1016/j.astropartphys.2014.03.002.

[11] Mathieu de Naurois and Loïc Rolland. A high performance likelihood reconstruction of γ-rays for imaging atmospheric cherenkov telescopes. *Astroparticle Physics*, 32(5):231–252, 2009. ISSN 0927-6505. doi: https://doi.org/10.1016/j.astropartphys.2009.09.001.

[12] Andrés G. Delgado Giler, Luan B. Arbeletche, Ralph Bird, et al. Measuring the depth of shower maximum of extensive air showers using Cherenkov light. *Astropart. Phys.*, 124:102508, 2021. doi: 10.1016/j.astropartphys.2020.102508.

[13] Luan B. Arbeletche and Vitor de Souza. Parametrization of the angular distribution of Cherenkov light in air showers. *Eur. Phys. J. C*, 81(2): 195, 2021. doi: 10.1140/epjc/s10052-021-08971-7.

[14] D. Heck, J. Knapp, J. N. Capdevielle, et al. *CORSIKA: a Monte Carlo code to simulate extensive air showers.* 1998.

[15] S. Ostapchenko. Monte Carlo treatment of hadronic interactions in enhanced pomeron scheme: QGSJET-II model. *Phys. Rev. D*, 83: 014018, Jan 2011. doi: 10.1103/PhysRevD.83.014018.

[16] M Bleicher, E Zabrodin, C Spieles, et al. Relativistic hadron-hadron collisions in the ultra-relativistic quantum molecular dynamics model. *Journal of Physics G: Nuclear and Particle Physics*, 25(9):1859–1896, sep 1999. doi: 10.1088/0954-3899/25/9/308.

[17] The CTA Consortium. *Science with the Cherenkov Telescope Array*. WORLD SCIENTIFIC, feb 2018. doi: 10.1142/10986. URL `https://doi.org/10.1142%2F10986`.

[18] Pierre Auger Collaboration. Depth of maximum of air-shower profiles at the Pierre Auger Observatory. i. measurements at energies above $10^{17.8}$ eV. *Phys. Rev. D*, 90:122005, Dec 2014. doi: 10.1103/PhysRevD.90.122005. URL `https://link.aps.org/doi/10.1103/PhysRevD.90.122005`.

[19] R. U. Abbasi, T. Abu-Zayyad, M. Al-Seady, et al. Indications of proton-dominated cosmic-ray composition above 1.6 EeV. *Phys. Rev. Lett.*, 104:161101, Apr 2010. doi: 10.1103/PhysRevLett.104.161101. URL `https://link.aps.org/doi/10.1103/PhysRevLett.104.161101`.

[20] T. K. Gaisser and A. M. Hillas. Reliability of the method of constant intensity cuts for reconstructing the average development of vertical showers. In 15^{nd} *Int. Cosmic Ray Conf.*, volume 8, pages 353–356, Plovdiv (Bulgaria), 1977.

Part II

Iron-proton separation for air showers simulations with the Cherenkov Telescope Array

4. Cosmic-ray measurements by reconstructing longitudinal profiles for the Cherenkov Telescope Array

Andrés G. Delgado Giler, M. Vecchi, V. de Souza
Results published in Proceedings of Science
URL: PoS(ECRS)073

ABSTRACT

The *Cherenkov Telescope Array (CTA)* will be the next-generation gamma-ray observatory to observe the energy range from 20 GeV to 300 TeV, offering 5-10 times better flux sensitivity than the current generation of *Imaging Atmospheric Cherenkov Telescopes (IACTs)*. Each telescope will capture an image of the Cherenkov light produced when air showers created by gamma or cosmic rays pass through the atmosphere.

The longitudinal development of the shower in the atmosphere can be studied by measuring the number of charged particles produced as a function of depth. The reconstruction of the longitudinal shower profile provides the *depth of the shower maximum* X_{max}, a mass-sensitive parameter useful for cosmic ray composition. In this work, we use for the first time the Cherenkov light detected on IACT cameras to reconstruct the longitudinal profile and the X_{max} of air showers initiated by two kinds of cosmic ray species, proton and iron, with energies between 10 TeV and 300 TeV. This method is different from other methods used in the past as template-based fit techniques that require a detailed and computing-intensive simulation chain. In contrast, we use a parameterized function for the angular distribution of Cherenkov light around the shower axis for the first time.

4.1 Introduction

Cosmic ray (CR) particles interact in the atmosphere, producing cascades of secondary particles known as air showers. Along each air shower, the number of charged particles reaches a maximum, referred to as X_{max}. The depth of the X_{max}, expressed in g/cm^2 of traversed matter, is a key observable to estimate the mass of primary cosmic particles (see [1] for a review) and has been used for many experiments (see [2, 3]). In this work, we applied a new method proposed in [4, 5] to reconstruct the longitudinal shower profile and the X_{max} from images recorded by imaging atmospheric Cherenkov telescopes (IACTs).

The Cherenkov Telescope Array (CTA) [6] will be the next generation of IACTs to observe the energy range from 20 GeV to 300 TeV. In order to observe the sky, tens of telescopes will be spread out over two arrays: one in La Palma (Spain, CTA North) and one in Paranal (Chile, CTA South). CTA will have telescopes of three different sizes: Small-Sized Telescopes (SSTs), Medium-Sized Telescopes (MSTs), and Large-Sized Telescopes (LST) to cover the large energy range. Since the cosmic-ray flux dominates the incoming gamma-ray flux, CTA could also provide cosmic composition through indirect CR measurements in the energy regime where the transition from galactic to extragalactic CRs occurs [7]. These indirect measurements would allow synergy with data from space instruments such as CALET [8] and DAMPE [9]. Nevertheless, indirect measurements have difficulties identifying individual CRs, and consequently, the composition has a lower resolution than direct measurements. Therefore, methods are required to measure mass-sensitive parameters as X_{max}. For instance, the Pierre Auger Observatory, which uses fluorescence telescopes to measure the development of CR air showers, has shown a total X_{max} resolution of about 15 g/cm^2 at energies above $10^{19.3}$ eV [10]. On the other hand, Monte Carlo template-based analysis [11] for IACTs is a commonly used tool to find the best-fit shower parameters, which provide a relatively small spread (30 g/cm^2) in the reconstructed values of the shower maximum. The template-based analysis techniques require detailed and computing-intensive simulations of image templates for each array configuration and particle type, while our method does not. Instead, our method uses a parameterized function that describes the development of the Cherenkov light along the air shower for gamma and cosmic rays separately [12]. For other techniques and resolution values, see [13, 14].

This work is organized as follows: section 4.2 describes the simulations used in this analysis. We also describe the method for reconstructing the longitudinal profiles and the quality cuts applied. Section 4.3 presents the

results of the X_{max} resolution. Additionally, we separate the iron events from proton showers using a cut on the X_{max} distribution. Finally, we conclude the work in section 4.4.

4.2 Air showers

4.2.1 Image simulation

In this work, the data set consists of simulated air showers generated by protons and iron CR particles detected by 25 MSTs with FlashCam using Prod5 (Omega configuration). The camera is hexagonal with a radius of 1.2 m for the external circle. The array dimension extends within a $\sim$ 500m radius circle. The events come from random directions within a view cone of 10 degrees, pointing at a 20-degree zenith angle in the North direction. A set of $\sim$ 15000 air showers from 10 TeV to 300 TeV was used for proton events following a power law in the energy distribution with a spectral index of -2.57. For iron events, we simulated $\sim$ 3000 events for each energy bin 10 TeV, 30 TeV, 50 TeV, 100 TeV and 300 TeV. The images are calibrated and parameterized using the ctapipe v11.0 [15]. The calibration process consists of an initial step where pixels must be above a given threshold value and a neighbour above a second threshold. Afterwards, the Hillas parametrization [16] allows the extraction of image parameters from these cleaned images. An example of one image produced by an 11.2 TeV proton-induced shower is shown on the top panel of Fig. 4.1, where triggered pixels are highlighted in green.

The information used to reconstruct the *shower plane* containing longitudinal profile involves the telescopes' position and direction in the layout and true values of the shower's impact and direction. We used the pixel intensities to estimate the number of photons along the longitudinal profile. The pixel coordinates are used to project each pixel from the camera into the shower plane.

4.2.2 Shower profile reconstruction

The longitudinal profile reconstruction is performed using the method described in [4, 17]. As a first step, we reconstruct a plane spanned by the shower axis and telescope position using the information of the shower core and direction. Within this plane, a geometrical projection of the camera pixels is achieved by using the pixel coordinates and the telescope axis. An example of one reconstructed shower plane with the geometrical

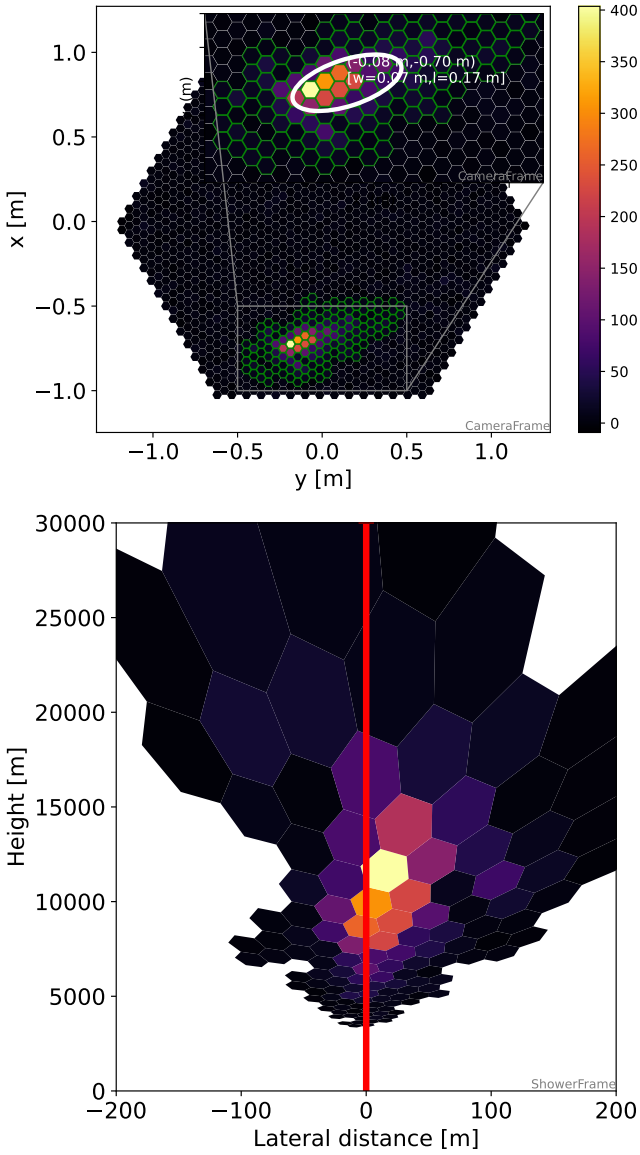

Figure 4.1: **Top panel**: Camera image generated by an 11.2 TeV proton-induced shower. The colour palette denotes the number of photo-electrons in the pixels. Triggered pixels are highlighted in green. The zoom box shows the ellipsoid obtained from the Hillas parametrization. **Bottom panel:** Shower plane. Pixels are projected along the height and lateral distance. The colour palette is the same as the camera view. The red line indicates the true direction of the shower axis.

pixel projection is shown at the bottom in Fig. 4.1. Only triggered pixels are projected in the plane.

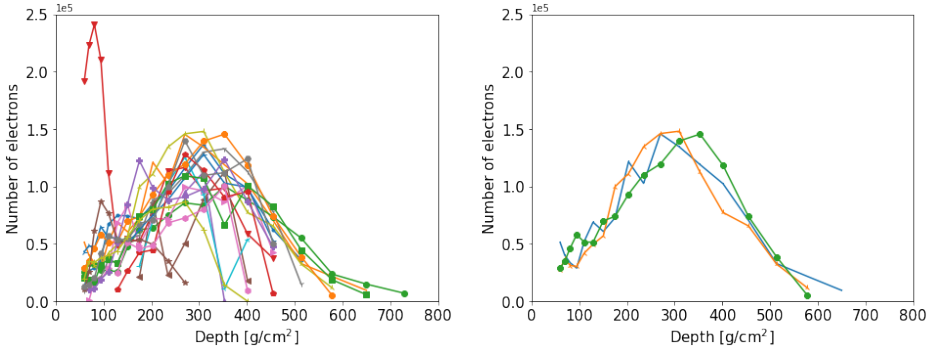

(a) Before applying cuts **(b)** After applying cuts

Figure 4.2: Profile reconstruction of an 11.2 TeV proton air shower. (a) Electron profiles before applying quality cuts. Each curve belongs to one image of a triggered telescope. In this case, 19 telescopes were triggered. (b) Electron profiles after applying quality cuts. Each curve belongs to one image of a triggered telescope.

With the help of the reconstructed shower plane, the content of every projected pixel of an image is binned along the vertical axis corresponding to the altitude. Then, the altitude is transformed in depth using an atmospheric model for CTA South. This process generates one photon profile $\frac{dN_\gamma}{dX}$ per telescope. In the final step of the reconstruction, the electron profiles $N_e(X)$ are obtained from the photon profiles using a parametrization for the angular distribution of Cherenkov light f_C around the shower axis given by [12]:

$$\frac{d^2N_\gamma}{d\theta\, dX}(\theta, s, h) = \frac{1}{\pi} N_e(X) \times f_C(\theta, s, h, E), \tag{4.1}$$

where θ is the angle between the shower axis and the photon emission, E is the energy of the primary particle, $s = 3X/(X + 2X_{max})$ is the shower age, and N_γ and N_e is the number of Cherenkov photons and electrons, respectively, at atmospheric depth X or altitude h. The form of the angular distribution of Cherenkov photons is shown in Appendix 4.A.

The attenuation and absorption of the photons in the atmosphere are also taken into account in the reconstruction by transmission factors due to Rayleigh (T_R) and Mie (T_M) scattering given in [18]:

$$T_R = \exp\left[-\left(\frac{|X_1 - X_2|}{X_R}\right)\left(\frac{400}{\lambda}\right)^4\right], \tag{4.2}$$

where X_1 and X_2 are the slant depth at emission and detection, λ is wavelength of the Cherenokov photon in nm, and X_R = 2974 g/cm^2,

$$T_M = \exp\left[\left(e^{-\left(\frac{h_1}{h_M}\right)} - e^{-\left(\frac{h_2}{h_M}\right)}\right)\frac{h_M \sec(\theta)}{L_M}\right], \tag{4.3}$$

where h_1 and h_2 are the emission and detection altitudes, the scale height is $h_M = 1200$ m, the mean free path at 360 nm for the Mie scattering is L_M = 14000 m, and θ is the angle between the shower axis and the photon emission.

Since equation (4.1) depends on the shower maximum through the shower age, s=1 is set at the beginning of the reconstruction. Once the electron profiles are calculated by using equation (4.1), the longitudinal profile is obtained as the average of the electron profiles. A Gaisser-Hillas (GH) function [19] is adjusted around the peak of the average profile to obtain the depth of the shower maximum reconstructed, which is referred to X_{max}^{rec} in the following. We recalculate and update the value of the X_{max}^{rec} in the next iterations. Fig. 4.2a shows the electron profiles at the 5th iteration, considering all the triggered telescopes for the same event where each camera image produces a profile. As shown in Fig. 4.2a, including profiles from all telescopes results in a noisy measurement of the longitudinal profile.

To determine the images that offer the best description in the reconstruction, we applied a quality cut in the number of *islands*. The number of islands is defined as a cluster of contiguous bright or boundary pixels surrounded by empty pixels. An island could be as large as the main part of a shower image or even as small as a single bright pixel. With island cleaning, more pixels are included, whilst the noise pixel is excluded as it is not part of a significant island. Hadronic showers tend to give rise to sub-showers, resulting in multiple Cherenkov images and, thus, light clusters away from the image's main part, resulting in an incorrect reconstruction of the longitudinal shower profile [20].

In order to identify those telescopes that provide the best description in the reconstruction, we applied the following quality cuts to select images: the position of the ellipse with respect to the centre of the camera must be less than or equal to 0.8 m, the number of pixels clusters per image must be less than 3, the telescope position with respect to the shower core must be within a radius of at least 300 m in order to see the region of the shower maximum, and each event must trigger at least five telescopes. Fig. 4.2b shows the electron reconstructed profiles using these cuts. It is remarkable to note that profiles that do not provide a good reconstruction are rejected.

4.3 Results

We can present our results based on the iron and proton simulated data sets described in the data section. This set is considered relevant to describe the heavier and lighter CR data better. In this section, we first inspect the reconstruction of the shower profile and check its compatibility with the true and reconstructed parameters. We then analyse shower maximum distribution and discuss the Fe/p separation based on the shower maximum.

4.3.1 Reconstructed profile

Fig. 4.3 shows an example of a reconstructed longitudinal shower profile for a proton event with the true depth of the shower maximum $X_{\rm max}^{\rm true} = 298.46$ g/cm^2. The blue curve corresponds to the average from the three profiles of Fig. 4.2b. The red curve is the Gaisser-Hillas function fitted around the maximum and constrained to the maximum data point, plus three data points to the right and left. The reconstructed shower maximum was $X_{\rm max}^{\rm rec} = 297.39 \pm 30$ g/cm^2, close to the true value.

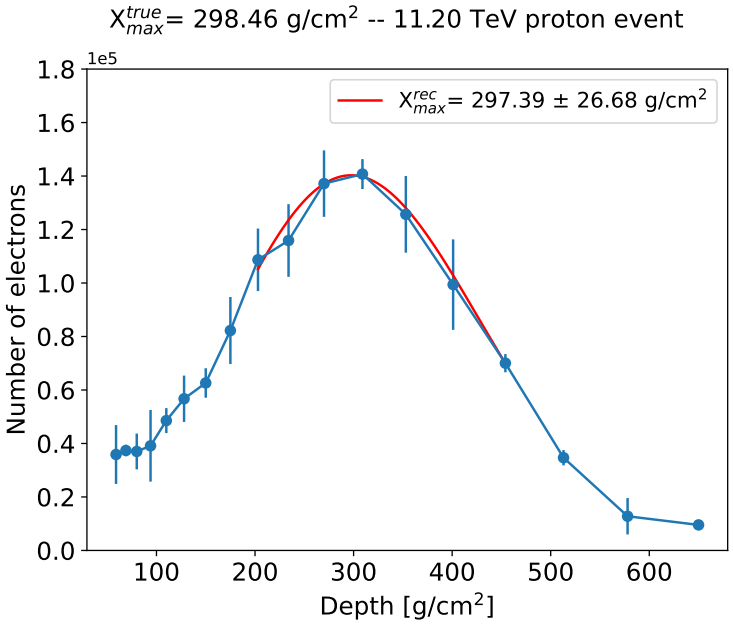

Figure 4.3: Reconstructed longitudinal profile of 11.2 TeV proton event. The profile is obtained as the average from the three profiles of Fig 4.2b. The red curve is the Gaisser-Hillas fitting around the maximum.

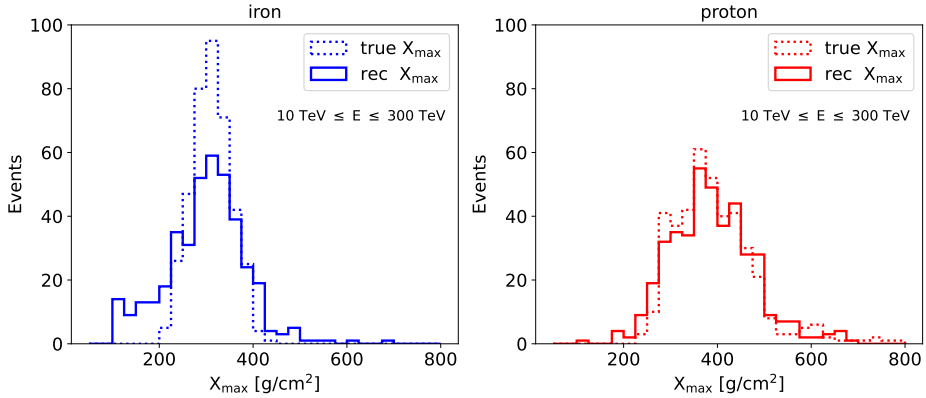

Figure 4.4: Comparison of the X_{max} distributions as reconstructed (solid histograms) for iron (blue) and proton (red) showers and the simulated distribution (dashed histograms).

The correct shape of the X_{max} distribution is crucial for estimating the cosmic-ray composition [21]. To investigate the X_{max} distribution, we show in Fig. 4.4 the results of the X_{max} reconstruction with our method in the energy range from 10 TeV to 300 TeV. The solid histograms represent the distribution of reconstructed X_{max} for iron (blue) and proton (red) showers. The simulated X_{max} values are marked by dashed histograms. It is noticeable that the simulated and reconstructed distributions agree with each other for both the iron and proton events. To validate our method, we separately estimated the resolution in the X_{max} reconstruction from the distribution of the difference between the reconstructed and the true shower maximum for proton and iron events. A Gaussian function is fitted on each distribution where the standard deviation σ and the mean μ of the distribution are considered as the resolution and bias of the method, respectively. The resolution and bias for proton and iron events taking the whole energy range are shown in Fig. 4.5. The resolution is around 31 $\pm$ 1 g/cm^2 for proton showers and represents a relative error of 11 % (see appendix 4.B and Fig.4.10 for the relative error distribution). In the case of iron showers, the resolution is around 37 $\pm$ 2 g/cm^2, representing a relative error of 8%. In both cases, the bias is marginally compatible with zero for iron and proton showers, meaning the reconstructed maximum is slightly shifted. The relative error of the bias is $<$ 1% in both kinds of showers. In Fig. 4.6, the event-by-event correlation between the X_{max} reconstructed and simulated is shown. The Pearson correlation coefficient is 0.74 for iron showers and 0.89 for proton showers.

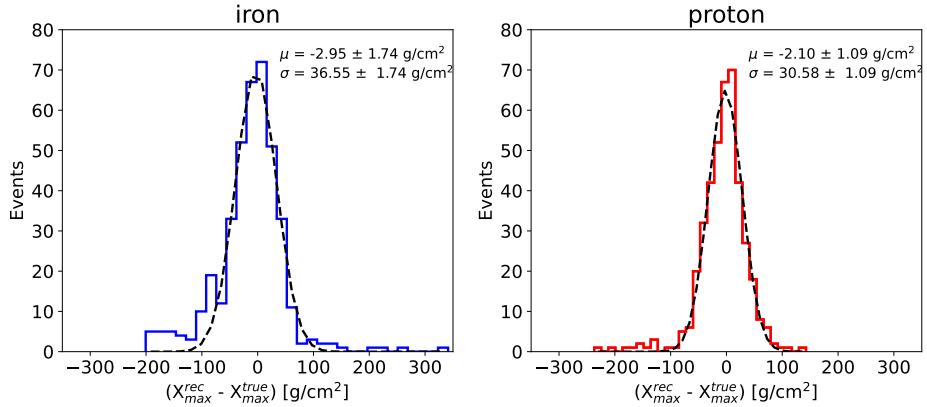

Figure 4.5: Distribution of the difference between the reconstructed and the true shower maximum for iron (blue) and iron (red) showers. Gaussian fitting is the black dashed curve with their respective mean and standard deviation.

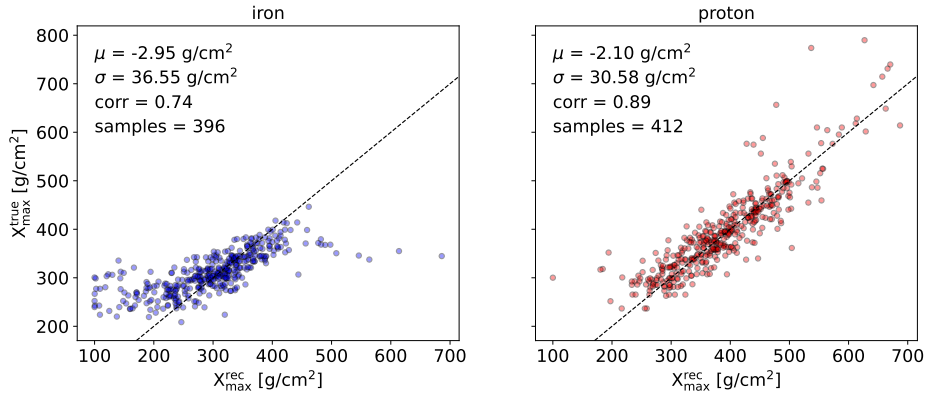

Figure 4.6: Event-by-event correlation of the X_{max} reconstructed and simulated for iron (blue) and proton (red) showers.

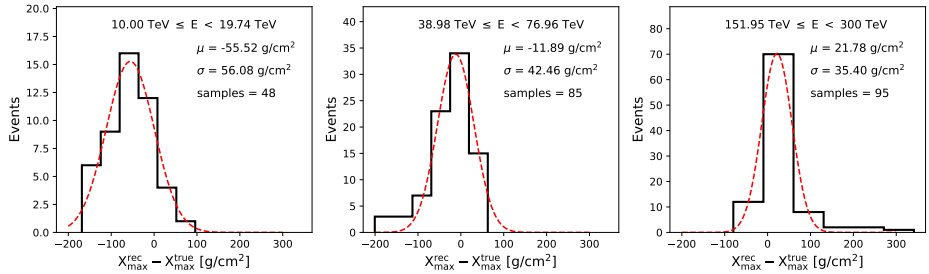

Figure 4.7: Difference of the X_{max} between reconstructed and true values for three example energy intervals for iron showers.

4.3.2 Resolution of X_{max} vs energy

To provide a more precise assessment of the reconstruction of the X_{max} and offer a detailed analysis of the resolution, we evaluated the first and second moments of the distribution of the shower maxima as a function of the energy. In figure 4.7, we present the event-by-event difference $\Delta X_{max} = X_{max}^{rec} - X_{max}^{true}$ for three example energy intervals for iron showers. It can be observed that all distributions are relatively narrow and follow a Gaussian function. Each energy interval's bias and resolution values are obtained from a Gaussian fitting. The energy dependency of this reconstruction bias is summarized in Fig. 4.8b. The bias fluctuates between around 20 g/cm^2 and -20 g/cm^2 in the full energy range. Only the lowest bin at 14.87 TeV exhibits a larger bias for iron showers. The negative observed biases indicate that the average reconstructed X_{max} values are too small. Consequently, our method reconstructs shallower X_{max} values for iron showers, except at the highest energy bin. In contrast, larger X_{max} values are reconstructed for proton showers. The error bars represent the uncertainty from the Gaussian fitting. In Fig. 4.8a, we show the standard deviation $\sigma_{\Delta X_{max}}$ of the event-wise differences between the reconstructed and true shower maximum. There is a significant energy dependence in the resolution for iron events, which decreases from 56.08 g/cm^2 at 14.87 TeV to 35.40 g/cm^2 at about 226 TeV. In the case of proton showers, there is no significant energy dependence in the resolution. Only the highest energy bin at around 226 TeV shows a slightly smaller resolution of 24.98 g/cm^2. The error bars indicate the uncertainty of the $\sigma_{\Delta X_{max}}$ of Gaussian fitting within the corresponding energy bin.

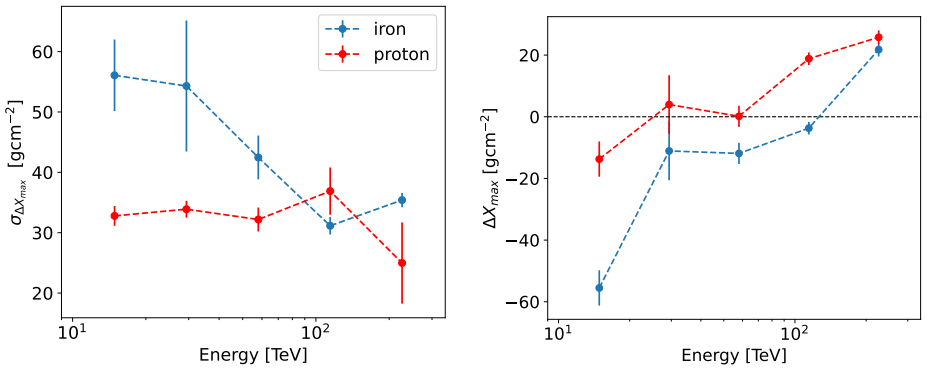

(a) Resolution **(b)** Bias

Figure 4.8: (Energy-dependent (a) resolution and (b) bias for proton and iron showers.

4.3.3 Iron-proton separation

In order to separate the iron events from proton showers, we set a cut on the shower maximum distribution called X_{max}^{cut}. Since proton showers develop deeper in the atmosphere, they will have a larger shower maximum than iron showers of the same energy. Hence, values of $X_{max} > X_{max}^{cut}$ are considered proton events, and values of $X_{max} \leqslant X_{max}^{cut}$ are considered as iron events. To calculate the position of the cut, we compute the efficiency of events classified as iron or proton. The iron η_{Fe} and proton η_p efficiency is defined as:

$$\eta_{Fe}(X_{max}^{cut}) = \frac{\text{iron events} \leqslant X_{max}^{cut}}{N_{Fe}}, \tag{4.4}$$

$$\eta_p(X_{max}^{cut}) = \frac{\text{proton events} \leqslant X_{max}^{cut}}{N_p}, \tag{4.5}$$

where N_{Fe} and N_p are the total number of triggered iron and proton events. Given this definition, η_{Fe} corresponds to the correct classification of iron events, and η_p corresponds to the misclassification of iron as proton events. Therefore, a maximum value of η_{Fe} and a minimum value of η_p gives the best scenario. Fig. 4.9 shows the iron (solid line) and proton (dashed line) efficiency for different cut values from 100 g/cm^2 to 700 g/cm^2. The optimal cut value is given at the position of maximum separation between both efficiency curves. The maximum separation occurs at $X_{max}^{cut} = 346$ g/cm^2 which corresponds to iron efficiency η_{Fe} of around 75 %. On the other hand, the false positive rate, which is the fraction of true proton events reconstructed as iron events, is about 32% for this cut.

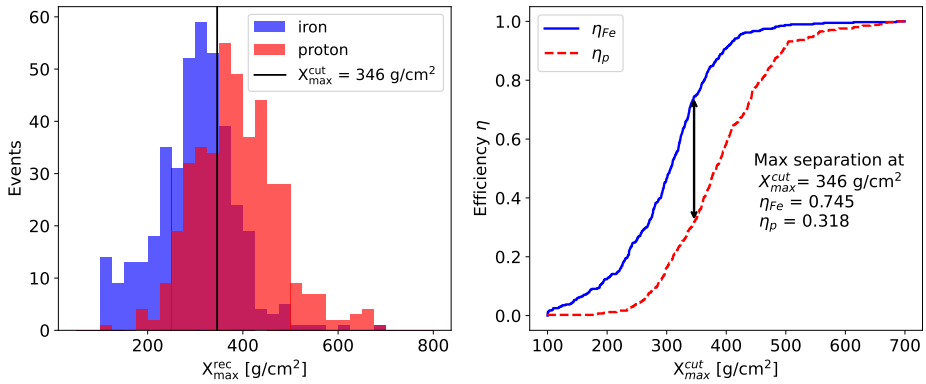

Figure 4.9: Left: distribution of reconstructed shower maximum for iron (blue) and proton (red) showers. The vertical line represents the optimized X^{cut}_{max}. Right: Iron and proton efficiency as a function of the X^{cut}_{max}. The black arrow shows the position of the maximum separation for both curves.

4.4 Conclusion

For the first time, longitudinal profiles of the Cherenkov emission of simulated cosmic-ray air showers using the CTA telescopes were reconstructed. In this study, we used $\sim 10^4$ simulated events of proton and iron recorded by the MSTs in the energy range from 10 TeV to 300 TeV. The applied method measured the shower maximum on an event-by-event basis, opening a complementary technique to space-based detectors for estimating the CR composition in the TeV energy range up to PeV.

The X_{max} resolution and bias for two kinds of cosmic-ray showers were obtained. For iron-induced showers, the resolution was 36.55 g/cm^2, and the bias was -2.95 g/cm^2 in the energy range from 10 TeV to 300 TeV. For proton-induced showers, the resolution was below compared to the iron case, 30.58 g/cm^2, and the bias was -2.10 g/cm^2. The bias in both cases showed a slight shift in the reconstructed shower maximum. When analysing per energy bin, the resolution of X_{max} improves as the energy of cosmic rays increases and depends on the composition of the cosmic rays. For iron-induced showers, the resolution is 56.08 at the lowest energy bin and improves to 35.40 at the highest energies. For proton primaries, the resolution is around 34 g/cm^2 along the energy and is better than 25 g/cm^2 at the highest energy bin. We then estimate the bias of reconstructed X_{max}. Compared to the true shower maximum, a shift of the reconstructed X_{max} of up to -2 g/cm^2 was found for both primaries in the full energy range.

The bias fluctuates around $\pm$ 20 g/cm^2 from 10 TeV to 300 TeV, and only the lowest energy bin shows a larger shift for iron showers.

Additionally, reconstructing the longitudinal profile and X_{max} opens the possibility for complementary indirect measurements of cosmic rays, especially in the energy regime where direct observations lack statistics. For instance, the reconstructed X_{max} distribution is suitable for distinguishing between light and heavy nuclei. We separated iron from proton showers by applying a cut on the shower maximum distribution at 346 g/cm^2. The true reconstructed iron events were separate with an efficiency of 74.5 %, while the 31.8 % corresponded to the fraction of true proton events reconstructed as iron primaries.

Since we are using one type of telescope, it is essential to mention that the resolution stated in this analysis does not represent the actual X_{max} resolution expected by the entire CTA South array at the end of the construction phase. However, it has a significant potential to offer new understandings of the composition of cosmic rays at very high energy levels.

Appendix 4.A Angular distribution of Cherenkov photons

We used the angular distribution of Cherenkov photons f_C given in the literature by [12] as:

$$f_C(\theta, s, h, E) = N \sin(\theta) I(\theta, h) K(\theta, s, h, E) \tag{4.6}$$

where the $I(\theta, h)$ corresponds to the distribution of the light and $K(\theta, s, h, E)$ represents the electron energy along the atmosphere. We used the parametrisation for I and K proposed by Luan B. in [12]:

$$I(\theta, \theta_{em}) = \frac{1}{\sin\langle\theta_p\rangle} \begin{cases} \pi - \log\left(1 - \frac{\theta}{\theta_{em}}\right), & \text{if } \theta \leqslant \theta_{em} \\ \pi - \log\left(1 - \frac{\theta_{em}}{\theta}\right), & \text{if } \theta > \theta_{em}, \end{cases} \tag{4.7}$$

and

$$K(\theta, s, h, E) = C \left\langle\theta_p\right\rangle^{\nu-1} e^{-\frac{\langle\theta_p\rangle}{\theta_1}} \left(1 + \epsilon e^{\frac{\langle\theta_p\rangle}{\theta_2}}\right) \tag{4.8}$$

where $\theta_{em} = \arccos(1/n)$. θ_p stands for the scattering angle of the particle originating the Cherenkov photon and its average is given by [12]:

$$\theta_p = \begin{cases} \theta_{em}, & \text{if } \theta \leqslant \theta_{em} \\ \theta, & \text{if } \theta > \theta_{em}, \end{cases} \tag{4.9}$$

The parameters ν, θ_1, θ_2 and ϵ vary with the shower age, energy, and refractive index (height):

$$\begin{aligned} \nu(s, n) &= p_{0,\nu}(n-1)^{p_{1,\nu}} + p_{2,\nu}\log(s) \\ \theta_1(s, n, E) &= p_{0,\theta_1}(E)^{p_{2,\theta_1}}(n-1)^{p_{1,\theta_1}} + p_{3,\theta_1}\log(s) \\ \theta_2(s, n, E) &= \theta_1(s, n, E)(p_{0,\theta_2} + p_{1,\theta_2}\, s) \\ \epsilon(E) &= p_{0,\epsilon} + p_{1,\epsilon}(E)^{p_{2,\epsilon}} \end{aligned} \tag{4.10}$$

where the coefficients are listed in tables 4.1 and 4.2 for gamma and proton air showers, respectively. We consider the proton air shower coefficients for iron showers in our reconstruction.

Appendix 4.B Distribution of $\Delta X_{\max}$

Fig. 4.10 shows the relative error of the difference distribution between the $X_{\max}^{\text{rec}}$ and $X_{\max}^{\text{true}}$ for both iron and proton, separately. A Gaussian function is fitted (black) in order to obtain the mean and standard deviation parameters.

i	$p_{0,i}$	$p_{1,i}$	$p_{2,i}$	$p_{3,i}$
ν	0.34329	-0.10683	1.46852	-
θ_1	1.4053	0.32382	0	-0.048841
θ_2	0.95734	0.26472	-	-
ϵ	0.0031206	0	0	-

Table 4.1: Coefficients for the angular distribution of Cherenkov photons in gamma-ray showers. Taken from [12]

i	$p_{0,i}$	$p_{1,i}$	$p_{2,i}$	$p_{3,i}$
ν	0.21155	-0.16639	1.21803	-
θ_1	4.513	0.45092	-0.008843	-0.058687
θ_2	0.90725	0.41722	-	-
ϵ	0.009528	0.022552	-0.4207	-

Table 4.2: Coefficients for the angular distribution of Cherenkov photons in proton showers. Taken from [12]

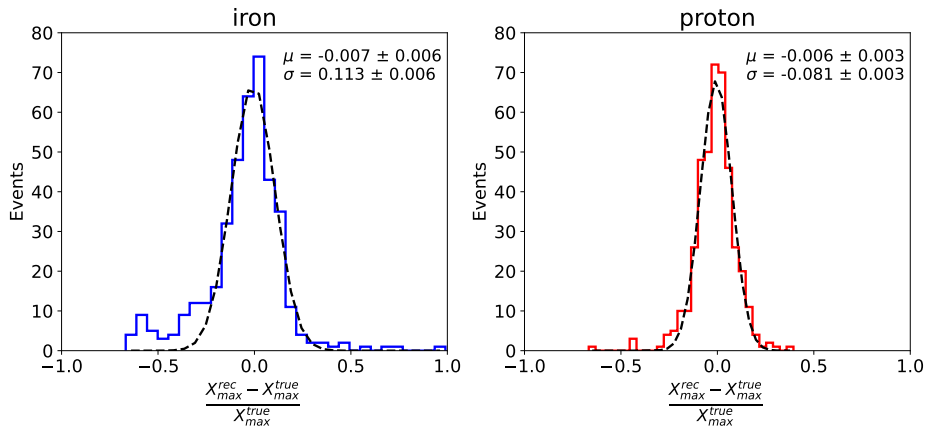

Figure 4.10: Relative error of the difference between the reconstructed and the true shower maximum for iron (blue) and iron (red) showers. Gaussian fitting is the black dashed curve with their respective mean and standard deviation.

Appendix 4.C Distribution of ΔX_{max} per energy intervals

4.C.1 Iron showers

Fig. 4.11 and 4.12 show the difference distributions and their relative error, respectively, between the reconstructed and simulated shower maximum for iron showers. The mean μ and standard deviation σ are obtained from a Gaussian fitting (red dashed curve).

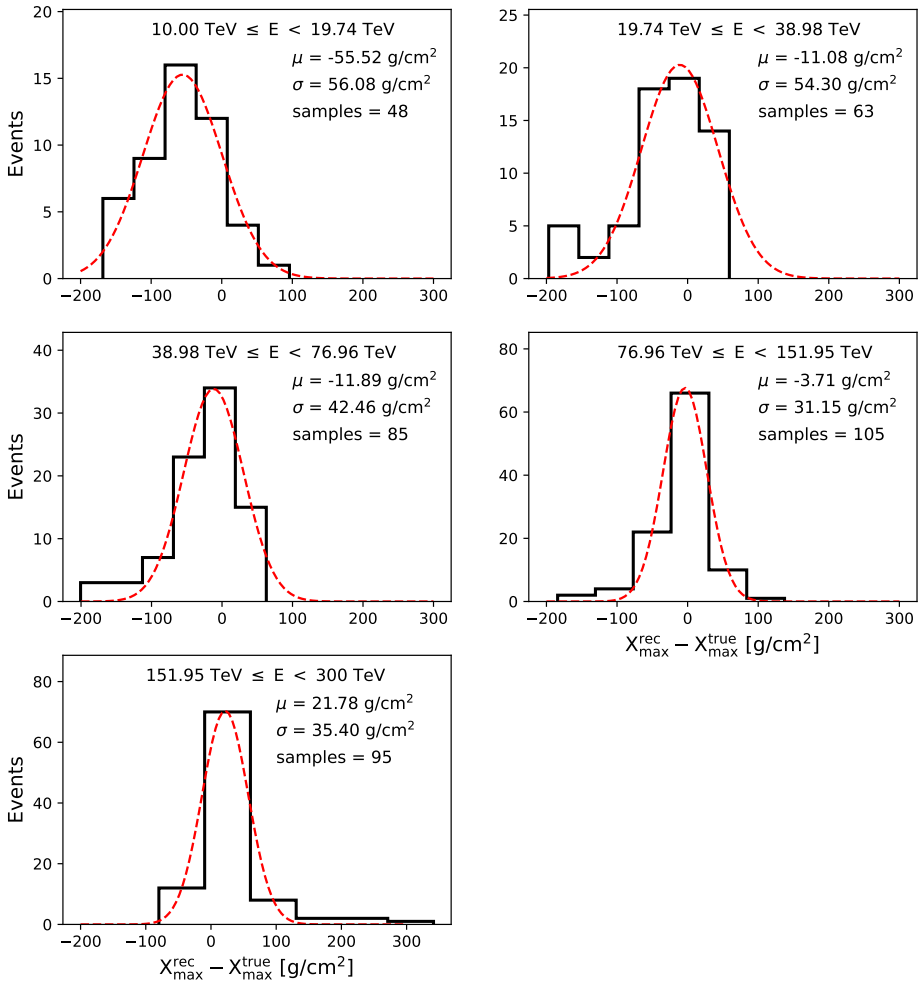

Figure 4.11: Difference of the X_{max} between reconstructed and true values for five energy intervals for iron showers.

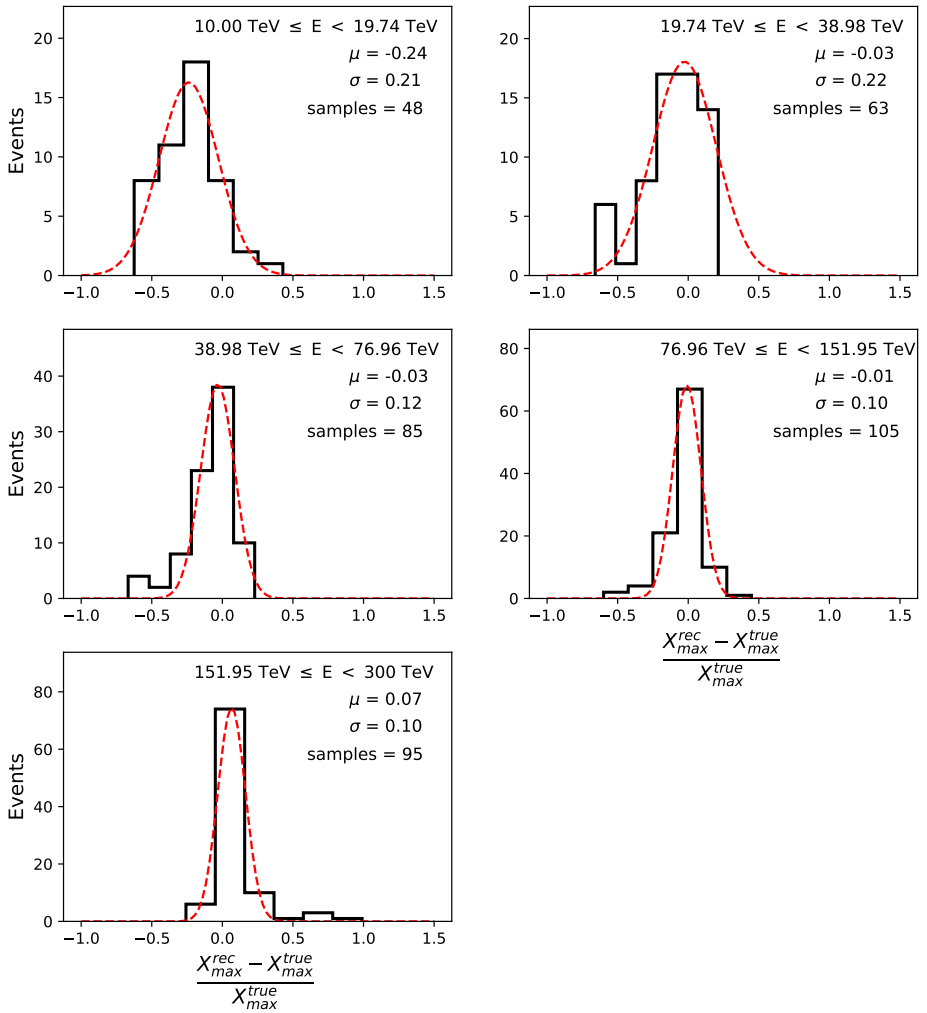

Figure 4.12: Relative error difference of the X_{max} between reconstructed and true values for five energy intervals for iron showers.

4.C.2 Proton showers

Fig. 4.13 and 4.14 show the difference distributions and their relative error, respectively, between the reconstructed and simulated shower maximum for proton showers. The mean μ and standard deviation σ are obtained from a Gaussian fitting (red dashed curve).

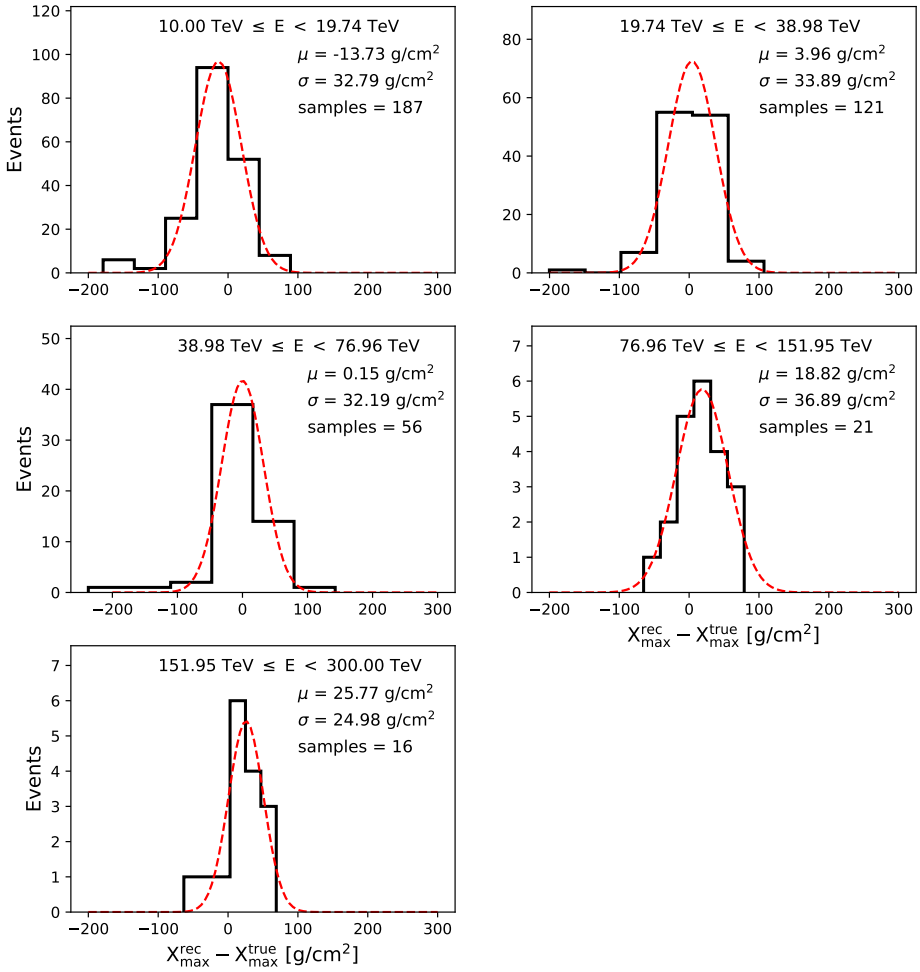

Figure 4.13: Difference of the X_{max} between reconstructed and true values for five energy intervals for proton showers.

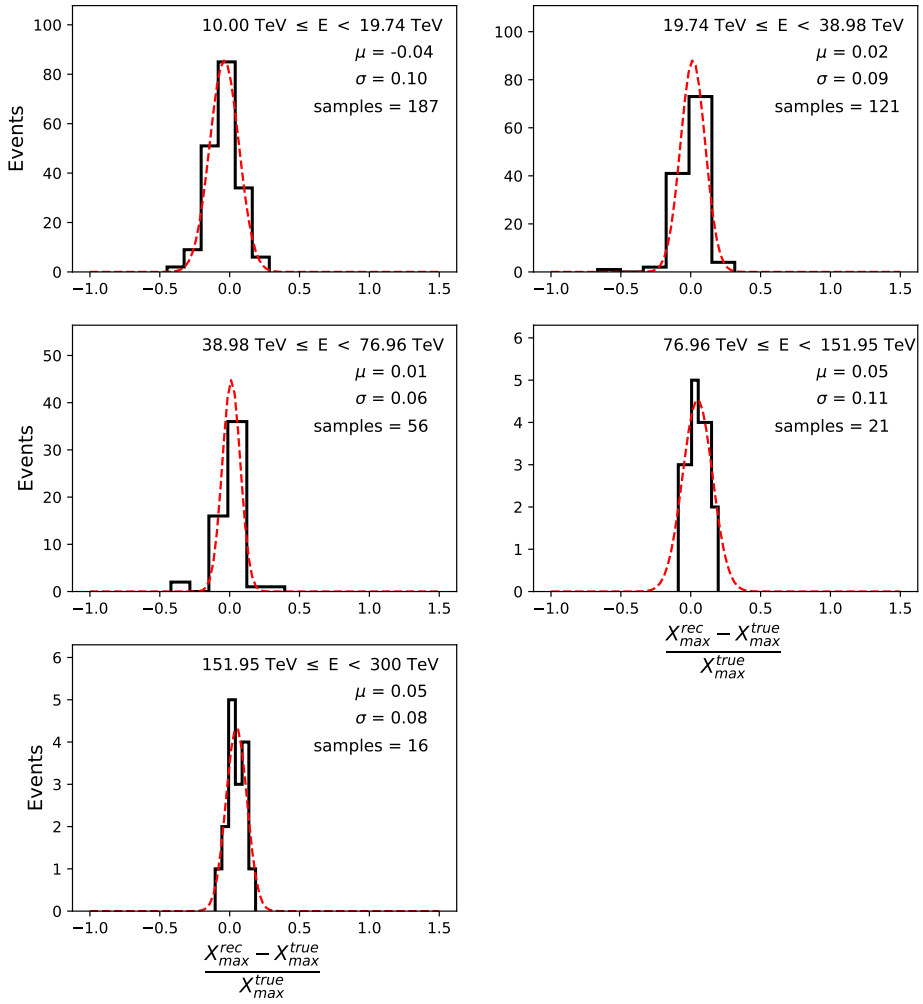

Figure 4.14: Relative error difference of the X_{max} between reconstructed and true values for five energy intervals for proton showers.

Bibliography

[1] Karl-Heinz Kampert and Michael Unger. Measurements of the cosmic ray composition with air shower experiments. *Astroparticle Physics*, 35 (10):660–678, May 2012. doi: 10.1016/j.astropartphys.2012.02.004.

[2] Alberto Daniel Supanitsky. Determination of the Cosmic-Ray Chemical Composition: Open Issues and Prospects. *Galaxies*, 10 (3):75, 2022. doi: 10.3390/galaxies10030075.

[3] Pedro Abreu et al. The depth of the shower maximum of air showers measured with AERA. *PoS*, ICRC2021:387, 2021. doi: 10.22323/1.395.0387.

[4] Andrés G. Delgado Giler and Vitor de Souza. Cosmic-ray measurements with an array of Cherenkov telescopes using reconstruction of longitudinal profiles of air showers, September 2022. arXiv:2209.04045.

[5] Andrés G. Delgado Giler and Vitor de Souza. Cosmic-ray measurements with an array of cherenkov telescopes using reconstruction of longitudinal profiles of air showers. *Astroparticle Physics*, 148:102817, 2023. ISSN 0927-6505. doi: https://doi.org/10.1016/j.astropartphys.2023.102817. URL https://www.sciencedirect.com/science/article/pii/S0927650523000038.

[6] B.S. Acharya et al. Introducing the CTA concept. *Astroparticle Physics*, 43:3–18, 2013. ISSN 0927-6505. doi: https://doi.org/10.1016/j.astropartphys.2013.01.007. URL https://www.sciencedirect.com/science/article/pii/S0927650513000169. Seeing the High-Energy Universe with the Cherenkov Telescope Array - The Science Explored with the CTA.

[7] Jörg R. Hörandel. On the knee in the energy spectrum of cosmic rays. *Astroparticle Physics*, 19(2):193–220, 2003. ISSN 0927-6505. doi: https://doi.org/10.1016/S0927-6505(02)00198-6. URL https://www.sciencedirect.com/science/article/pii/S0927650502001986.

[8] Y Asaoka, O Adriani, Y Akaike, et al. Calet results after three years on the international space station. *Journal of Physics: Conference Series*, 1468(1):012074, feb 2020. doi: 10.1088/1742-6596/1468/1/012074. URL https://dx.doi.org/10.1088/1742-6596/1468/1/012074.

[9] Francesca Alemanno. Latest results from the DAMPE space mission. In *56th Rencontres de Moriond on Very High Energy Phenomena in the Universe*, 9 2022.

[10] Aab, A. et al. Depth of maximum of air-shower profiles at the Pierre Auger Observatory. I. Measurements at energies above 1 $0^{17.8}$ eV. Phys. Rev. D, 90(12):122005, December 2014. doi: 10.1103/PhysRevD.90.122005.

[11] R. D. Parsons and J. A. Hinton. A Monte Carlo template based analysis for air-Cherenkov arrays. *Astroparticle Physics*, 56:26–34, April 2014. doi: 10.1016/j.astropartphys.2014.03.002.

[12] Luan B. Arbeletche and Vitor de Souza. Parametrization of the angular distribution of Cherenkov light in air showers. *European Physical Journal C*, 81(2):195, February 2021. doi: 10.1140/epjc/s10052-021-08971-7.

[13] S. Buitink, A. Corstanje, J. E. Enriquez, et al. Method for high precision reconstruction of air shower $X_{\max}$ using two-dimensional radio intensity profiles. *Phys. Rev. D*, 90:082003, Oct 2014. doi: 10.1103/PhysRevD.90.082003. URL https://link.aps.org/doi/10.1103/PhysRevD.90.082003.

[14] R. Conceição, L. Peres, M. Pimenta, and B. Tomé. New methods to reconstruct $X_{\max}$ and the energy of gamma-ray air showers with high accuracy in large wide-field observatories. *Eur. Phys. J. C*, 81(1):80, 2021. doi: 10.1140/epjc/s10052-021-08883-6.

[15] Karl Kosack, Jason Watson, Maximilian Nöthe, et al. cta-observatory/ctapipe: v0.11.0, May 2021. URL https://doi.org/10.5281/zenodo.4746317.

[16] A. M. Hillas. Cerenkov Light Images of EAS Produced by Primary Gamma Rays and by Nuclei. In *19th International Cosmic Ray Conference (ICRC19), Volume 3*, volume 3 of *International Cosmic Ray Conference*, page 445, August 1985.

[17] Andrés G. Delgado Giler, Luan B. Arbeletche, Ralph Bird, et al. Measuring the depth of shower maximum of extensive air showers using cherenkov light. *Astroparticle Physics*, 124:102508, 2021. ISSN 0927-6505. doi: https://doi.org/10.1016/j.astropartphys.2020.102508. URL https://www.sciencedirect.com/science/article/pii/S0927650520300803.

[18] Peter K.F. Grieder. *Atmospheric Fluorescence*, pages 879–912. Springer Berlin Heidelberg, Berlin, Heidelberg, 2010. ISBN 978-3-540-76941-5. doi: 10.1007/978-3-540-76941-5_17. URL https://doi.org/10.1007/978-3-540-76941-5_17.

[19] T. K. Gaisser and A. M. Hillas. Reliability of the Method of Constant Intensity Cuts for Reconstructing the Average Development of Vertical Showers. In *International Cosmic Ray Conference*, volume 8 of *International Cosmic Ray Conference*, page 353, January 1977.

[20] I. H. Bond, A. M. Hillas, and S. M. Bradbury. An island method of image cleaning for near threshold events from atmospheric Cherenkov telescopes. *Astropart. Phys.*, 20:311–321, 2003. doi: 10.1016/S0927-6505(03)00193-2.

[21] Vitor de Souza. Measurements of the depth of maximum of air-shower profiles at the pierre auger observatory and their composition implications. *arXiv: High Energy Astrophysical Phenomena*, page 010015, 2016.

5. Iron and proton separation using convolutional neural networks for the Cherenkov Telescope Array.

Andrés G. Delgado Giler, M. Vecchi, V. de Souza
Manuscript in preparation

ABSTRACT

The *Cherenkov Telescope Array* (CTA) will be the next-generation gamma-ray observatory offering better flux sensitivity than the current generation. Each telescope will detect the Cherenkov emission from air showers initiated by gamma and cosmic rays. State-of-the-art deep learning algorithms, such as convolutional neural networks (CNNs), are used to reconstruct the energy and classify the primary particle. CNNs are commonly used for image classification because they extract and learn from the features and patterns within an image. In this work, we proposed an architecture to separate iron and proton-induced showers using the image recorded in the camera (Image), the depth of the shower maximum (X_{max}), and the particle energy (E) associated with the air shower. We tested the CNN performance with three different inputs: (i) Image + E, (ii) Image + X_{max}, and (iii) Image + X_{max} + E. In addition, we used reconstructed and true values (for the X_{max} and E) during the training and the prediction. This architecture takes advantage of the image patterns and the air showers' mass-sensitive parameters. Therefore, we aim to obtain significant efficiency in identifying iron and proton events.

5.1 Introduction

Very-high energy (VHE) gamma rays are photons with energies between hundreds of GeV to hundreds of TeV that hit the Earth's atmosphere [1].On the other hand, cosmic rays (CRs) are relativistic charged particles made up of $\sim$ 85% protons, $\sim$ 12% helium, $\sim$ 2% electrons, and $\sim$ 1% of heavier charged nuclei with energies up to $\sim 10^{15}$ eV (also known as the *knee*) [2]. The flux of CRs with energies below the knee can be described by a power law spectrum $\frac{d\Phi}{dE} \propto E^{-\gamma}$ with a spectral index $\gamma \sim 2.7$: these particles are expected to be of Galactic origin [3]. Precise measurement of the CR flux is essential because it encodes important information about sources and properties of CR propagation in the Galaxy. For instance, specific components of the CR flux can contain additional spectral structures [4]. On the other hand, although supernova remnants (SNRs) are the most likely candidate for the galactic CRs, the search for the sources of GCRs is still an open question [5, 6].

The Earth's atmosphere is opaque to gamma rays and CRs. When these particles hit the atmosphere, a cascade of secondary particles (including electrons, positrons, and pions) is created. This cascade is called *air shower* [7]. The secondary particles propagating in the atmosphere with velocities higher than the speed of light produce nanosecond-long flashes of Cherenkov radiation captured by arrays of *Imaging Atmospheric Cherenkov Telescopes* (IACTs), which use these light pulses to reconstruct the type of primary particle, the energy, and the direction of the primary particle. The Cherenkov Telescope Array (CTA) [8] is the next-generation ground-based instrument for gamma-ray astronomy at very high energies. It will be made of several tens of IACTs located on both hemispheres, and it will cover an unprecedented energy range between 20 GeV to 300 TeV providing 5-10 times better flux sensitivity than the current generation of telescopes (such as MAGIC [9], HESS [10], VERITAS [11]). Although designed as a gamma-ray observatory, CTA will also detect air showers initiated by CRs due to their high flux compared with gamma rays and is expected to perform higher event statistics than the current systems. To evaluate CTA's potential for identifying CR events, we performed dedicated Monte Carlo simulations, which included the air shower development and telescope detection of proton and iron events.

Traditionally, the separation of CRs and gamma-ray events relies on the *Hillas parameters* [12], which characterize the elliptical shape of the shower image on the cameras. These parameters are used to reconstruct the properties of the incoming particle [13, 14]. Other methods, such as the ImPACT algorithm [15], use image templates from simulations to

reconstruct shower parameters. CNNs are supervised learning algorithms that can extract and learn essential features of images and determine which category they correspond to. The use of CNNs encompasses several fields of science, including physics and astroparticle physics [16, 17, 18, 19, 20, 21, 22, 23]. Currently, CNNs are used in IACT analysis for the gamma/cosmic-ray separation, energy, and shower direction reconstruction [24, 25, 26, 27, 28, 29, 30, 31]. The state of the art of CNNs includes algorithms such as VGG [32], AlexNet [33], GoogLeNet [34], and ResNet [35]. In particular, the VGG16 is based on a structure of blocks of 2D convolutional and fully connected layers that can extract features and classify the images.

In this work, we present a machine-learning approach that allows the identification of CRs nuclei based on the measurement of the Cherenkov light with ground-based Imaging Cherenkov Telescopes. We focused our study on the TeV energy range, where CR measurements can be compared with those of the current generation satellite experiments such as AMS-02, CALET and DAMPE. We trained our CNN on SSTs, and MSTs simulated images from proton-induced and iron-induced air showers where the algorithm can learn essential features of the images. SSTs and MSTs detect events in the TeV energy range were chosen because they cover the highest energy range up to 300 TeV. We aim to obtain iron efficiencies $>$ 90% while keeping the proton misidentification rate as low as possible using different inputs for training our CNN.

Our strategy was the following: First, we generated the telescopic images of air showers initiated by two cosmic ray species: iron and proton. Then, the images of each primary particle type are combined into a final image containing either one or multiple telescope detections. The shower images are simulated for MST and SST. We proposed different scenarios considering different inputs for the CNN training, combining the image pixel intensities, type of telescope, the true and reconstructed values of the shower maximum and primary particle energy of each event. We trained our CNN based on labelled images and tested the performance using the Receiver Operating Curve (ROC) and efficiency-vs-energy curves.

In section 5.2, we describe the details of the air shower simulation and the generation of the images. In section 5.3, we explain the architecture used. We also describe the metrics used to characterize the performance of our algorithm. In section 5.4, we present the input features and the performance of reconstructing the energy using the random forest algorithm. In addition, the shower maximum reconstruction is also described. In section 5.5, the results of our classifier are described for the different types of inputs and telescopes. The results are based on signal-

background separation distributions, the Receiver operating characteristic (ROC) and the energy dependence of the iron efficiency. In section 5.6, we summarise our findings and discuss some advantages and limitations of our method, applications and extensions.

5.2 Simulation Setup

One of the two CTA arrays will be located in Paranal (Chile) at 2147 m above sea level [36]. This array will contain two types of telescopes of interest for this work: the medium-size telescope (MST) and the small-size telescope (SST). The MST has a reflector dish of 11.5 m of primary diameter containing an effective mirror area of 90 m^2 [37]. The camera is placed at the dish's focal point, at a distance of 16 m, with respect to the primary mirror. The camera has 1764 hexagonal pixels organized in a hexagonal lattice. Each MST has a field of view of around 8°. In contrast, the SST has a reflector diameter of 4 m, representing an effective mirror area of 8 m^2. The camera has 2368 square pixels and is located at a focal distance of 2.15 m. The field of view of the SST is $\sim 9^\circ$ [38]. Both types of telescopes are aligned to point in the same direction (parallel pointing). IACTs are designed to capture the flash of Cherenkov light from the air shower and detect it through the camera pixels as photo-electron counts. As a result, camera images are recorded and saved in HDF files. The simulation and extraction of the shower images consist of two stages: air shower simulation and shower detection. We now describe our procedure for simulating shower images for CTA.

5.2.1 Air shower simulation

We use the version called *Prod5* from the CTA collaboration for the extensive air showers simulation. The Prod5b is based on *CORSIKA* (COsmic Ray SImulations for KAskade) [39] and *simtelarray* [40] packages. Among the several candidates of array configurations, we selected the *OMEGA* configuration in this study. In this configuration, the 25 MSTs and 70 SSTs are distributed as shown in Fig 5.1. The main inputs we have set are 1) the particle type, 2) the energy range, 3) the direction of the primary particle, 4) the angle cone for diffuse air showers, and 5) the area for shower impact.

We simulate air showers initiated by proton (p) and iron (Fe) cosmic rays. The choice of these nuclei is motivated by representing light and heavy components of cosmic rays. We generated around 20000 events

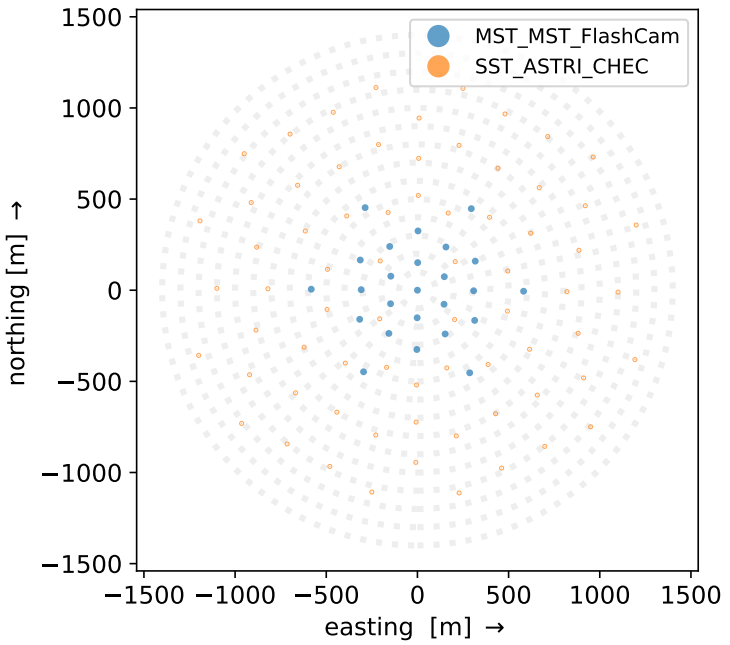

Figure 5.1: Array configuration used in the simulation. There are 25 MTSs and 70 small-size SSTs.

for each primary in the energy range from 1 TeV to 300 TeV. This energy coverage plays an important role in the origin and acceleration mechanism of Galactic cosmic ray particles, offering synergy for composition analysis with data from space experiments. The events are generated following a power law with a spectral index of -2.57. The detection level is 2147 m above sea level. The zenith angle of the primary particles is 20°, and the viewcone[1] is 10°. Table 5.1 summarises the configuration options we selected for our simulations.

5.2.2 Shower detection

Shower detection involves calibrating and extracting the camera images [41]. For the calibration of the images, we use the *ctapipe* package [42]. In this step, the images are cleaned to eliminate pixels that contain noise from the night sky background. The image-cleaning procedure involves selecting only pixels with a signal higher than the picture threshold and

[1]The *viewcone* is an option for diffuse simulation. It selects the primary to come from a cone around a fixed zenith, and azimuth angle

parameters	values
partID	5626 (Fe), 101 (p)
Energy range	1 TeV to 300 TeV
Zenith angle	20°
Azimuthal angle	pointing to the North
Viewcone angle	10°
Radius of thrown	1000 m

Table 5.1: Values used in the shower simulation.

all those above the boundary threshold that are neighbours of a picture pixel[2].After cleaning, the *Hillas parameters* are extracted for each image. The depth of the shower maximum is reconstructed geometrically using the Hillas parameters and assuming that the shower maximum lies at the brightest point of the camera image [42].

In order to provide readable square lattice images into our CNN, we performed transformations depending on the pixel shape. The SST images are already square-shaped. In this case, the image transformation consists only of filling each corner with zero values, as shown in Fig. 5.3. On the other hand, MST images are hexagonal-shaped. In order to transform an image with hexagonal pixels into a readable square-shaped image, we used the oversampling mapping method[3] [43] using the DL1-Data[4]-Handler (DL1DH) package [44]. This method divides every hexagonal pixel into n-by-n square pixels and assigns the photoelectrons of the new square pixel as n^{-2} of the original hexagonal pixel (for n=2). The final image can be seen on the right side of Fig. 5.2. The motivation to use the oversampling is based on superior performance over other methods [43].

In the final stage, we combined all CTA images of the same telescope and event by summing up individual pixel values and combining them into a single one. We acknowledge that this approach reduces the array performance, but it served to simplify our proof of concept work.

[2]For the ctapipe [42], the standard values of picture threshold is seven and boundary threshold is five.

[3]A mapping method transforms the input image into a square lattice image.

[4]DL1 data stands for calibrated data.

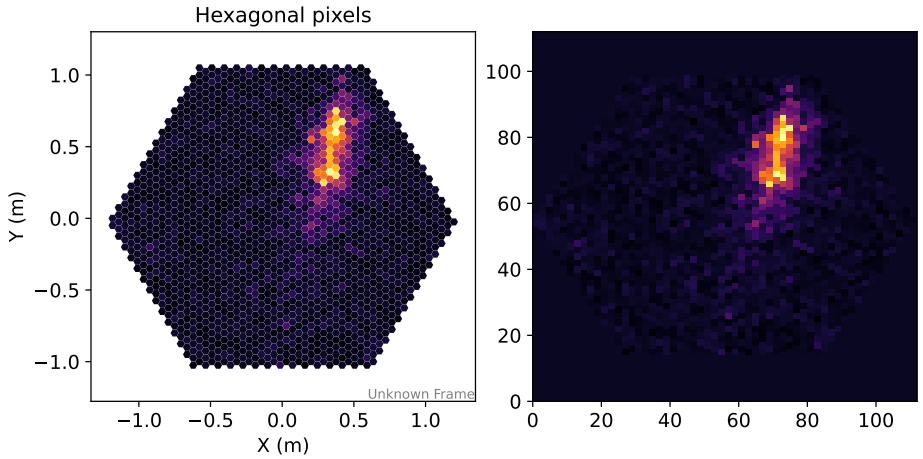

Figure 5.2: Left: MST camera detection of an iron event. The pixel arrangement is hexagonal-shaped. Right: Final image after transforming the same camera image into a square arrangement using the oversampling method.

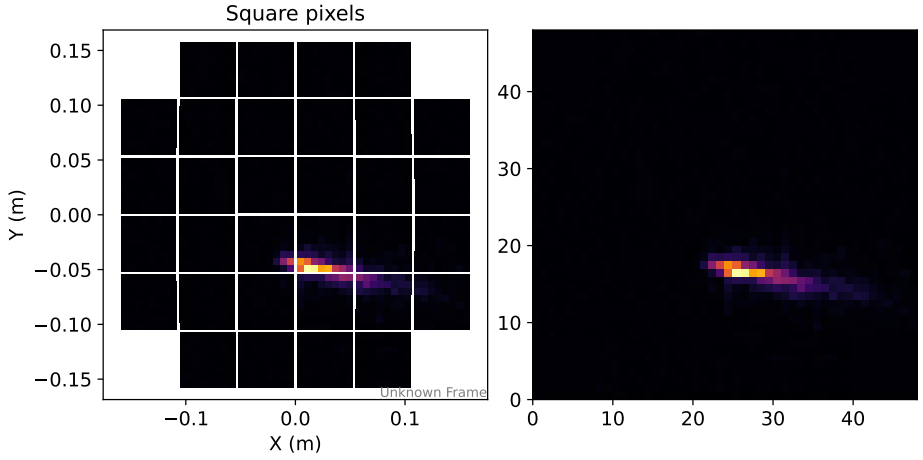

Figure 5.3: Left: SST camera detection of a proton event. The pixel arrangement is squared. Right: Final image after transformation of camera image into a square arrangement. The corners are filled with zero values.

5.3 Neural network architecture and performance metrics

In this section, we describe the details of the machine learning algorithms that we use to predict the species of the shower primary particle. The machine learning architecture was implemented using Keras [45] and Tensorflow [46] libraries. We used ADAptive Moment (ADAM) optimizer [47] with a batch size of 128, which is the number of processed samples before the CNN is updated. It was also considered an early stopping criterion of 10 iterations, which stops the training if no improvement is found. In the following, we will discuss the architecture of our neural network.

5.3.1 Binary classifier architecture

A CNN is a complex function that receives a set of images as input and predicts the classification class, that is, to what type of air shower the image belongs. We use supervised training, which means feeding the CNN using data with labels so that CNN can identify a specific class and classify it to that type. The main advantage of a CNN is to learn from the spatial relationship between pixels and learn the underlying features, such as edges or shapes, throughout each layer of the architecture. Our CNN corresponds to a modified VGG16 architecture as shown in Fig 5.4 and as detailed in Table 5.2. Six main layers define our architecture: input, convolutional, max pooling, flatten, dense, and output.

The **input layer** corresponds to the input image of dimension 48 x 48 for SST and 112 x 112 for MST. The dimensions of the input images are different to account for the differences between the SSTs and MSTs cameras. In particular, the 48 x 48 SST image comes from the number of square pixels in the camera. The 112 x 112 MST image comes from applying an oversampling method to the camera image that transforms a hexagonal lattice (hexagonal pixels in the flashCam) to a square lattice. The method divides each hexagonal pixel into four squared pixels and pads the corners with zero values. The **convolutional layers (Conv)** include the feature extraction from the input image. Our CNN model is motivated by VGG16 architecture, which uses a sequence of small filters grouped into blocks. The VGG16 baseline model contains around 15 million trainable parameters [32]. The CNN has 13 convolutional layers grouped in five blocks, as shown in Table 5.2. The first convolutional layer receives the input image and extracts a collection of feature maps (64 feature maps of dimension 112×112 for MST images). Each feature map

Figure 5.4: A sketch of our neural network architecture is shown. Image data from MST is sequenced into convolutional layers to extract the patterns and features. The result is flattened, concatenated with X_{max} and/or energy, and passed on to two fully connected layers that perform the classification task. The output layer is combined with the *softmax* function.

Modified VGG-16 for MST and SST images			
Layer	Description	Output shape: MST	Output shape: SST
Block 1	2xConv	**112** × **112** ×64	**48** × **48** × 64
	Max Pooling	56 × 56 × 64	24 × 24 × 64
Block 2	2xConv	56 × 56 × 128	24 × 24 × 128
	Max Pooling	28 × 28 × 128	12 × 12 × 128
Block 3	3xConv	28 × 28 × 256	12 × 12 × 256
	Max Pooling	14 × 14 × 256	6 × 6 × 256
Block 4	3xConv	14 × 14 × 512	6 × 6 × 512
	Max Pooling	7 × 7 × 512	3 × 3 × 512
Block 5	3xConv	7 × 7 × 512	3 × 3 × 512
	Max Pooling	3 × 3 × 512	1 × 1 × 512
–	Flattening	4608	512
–	Concatenating	4608 + (X_{max}, E)	512 + (X_{max}, E)
FC 1	Dense	512	512
FC 2	Dense	512	512
Output	Dense	2	2

Table 5.2: Description of the VGG-16 architecture for SST and MST image inputs. The baseline model (without adding X_{max} and energy parameters in the concatenation layer) for the SST and MST architecture has 15 239 874 and 17 337 026 trainable parameters, respectively. Adding either X_{max} or energy parameter in the concatenation increases 512 extra trainable parameters; adding both increases 1024 extra trainable parameters.

can be considered a new image where each pixel is a real number x. The activation function used for the output image is the REctifier Linear Unit (RELU) given by:

$$RELU(x) = \begin{cases} x & \text{for } x > 0 \\ 0 & \text{for } x < 0 \end{cases} \tag{5.1}$$

The next layer is the **max pooling** used to reduce the dimensionality of the output feature map (64 feature maps of dimension 56 × 56 for MST images). This process is repeated along the five blocks. As the image is passed from one block to the next, it generates more feature maps with reduced dimensions that would contain only essential features of the initial image.

At the end of block 5, we flatten all the output images and get a one-dimensional array of 4608 nodes (3 × 3 × 512 for MST images) that defines the **flatten layer**. The X_{max} and/or energy values associated with the image event are added after the flattening layer. We add one or two

extra nodes with these values in a concatenation layer. Adding either X_{max} or energy parameters in the concatenation layer increases 512 additional trainable parameters while adding both increases 1024 extra trainable parameters. The flattened layer is fully connected (FC) to two successive **dense layers** with 512 nodes each. We also use the RELU function for the FC layers. This part of the architecture is focused on the classification task and is based on the previous feature maps. The **output layer** is the final FC layer that encloses the number of labelled categories. In this case, for the binary classification, it has two nodes where each node is also a real number y_i. For this last layer, we used the *softmax* activation function given by:

$$\alpha_i = \frac{e^{y_i}}{\sum_{i}^{n_{categories}=2} e^{y_i}}, \tag{5.2}$$

where α_i is the output in $i-th$ node of the last layer. This function represents the probability distribution over the predicted output classes. Because we are training on labelled input data, the one-hot-encoding method passes the labels q_i as two-dimensional vectors. Therefore, the labels for iron and proton images are (1, 0) and (0,1), respectively. The architecture compares the α_i outputs with the labels using the *categorical cross-entropy* loss (L_{CCE}) function defined as:

$$L_{CCE} = -\sum_{i=1}^{n_{categories}=2} q_i \cdot \log \alpha_i. \tag{5.3}$$

The algorithm optimizes the trainable parameters during the training by minimizing the loss function averaged over all training input images using the *training data set*. For SST, the data set consisted of $\sim$ 20000 events equally distributed for iron and protons, with 11% corresponding to test and 89% for training and validation. For MST, the data set consisted of 32900 events with the same percentage for training and testing. Once the machine is trained, it uses an independent data set (*validation set*) to check if the machine is learning about the images by measuring the convergence of the loss function. We make the predictions on another independent *test data set* by choosing different threshold values of α_i.

5.3.2 Metrics to evaluate the performance of our classifier

To check the performance of the CNN, we use two classification metrics: the classification accuracy and the Receiver Operating Characteristic (ROC)

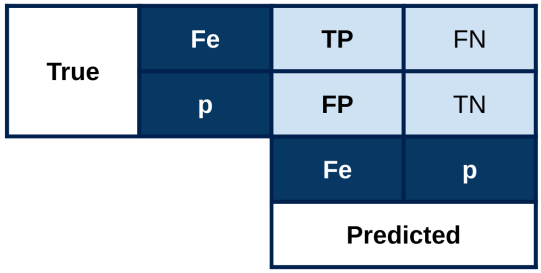

Figure 5.5: Confusion matrix for binary classification. The diagonal indicates the correct prediction of each category, while the off-diagonal boxes are miss-reconstructed predictions.

Term	Definition
True Positive (TP)	correctly classified iron events
True Negative (TN)	correctly classified proton events
False Positive (FP)	misclassified proton as iron events
False Negative (FN)	misclassified iron as proton events

Table 5.3: Definitions of event classifications for binary classification.

curve. The classification accuracy can be understood from the confusion matrix, which offers a detailed quantification of the performance of the model, as shown in Fig. 5.5. The columns indicate the predicted category, and the rows correspond to the true category. Then, the classification accuracy is defined as the number of correct classified predictions to the total number of predictions:

$$Accuracy = \frac{TP + TN}{TP + TN + FP + FN}, \tag{5.4}$$

where the definitions for the binary classifications are listed in Table 5.3. On the other hand, the ROC curve shows the performance of the classification task for different threshold values of s_i (equation 5.2). It shows the true positive rate as a function of the false positive rate for all possible threshold values, providing discrimination power at different thresholds. This plot provides the area under the curve (AUC) that is a metric in the range [0,1] and checks the performance of the CNN. The greater the AUC, the better the performance.

Term	Definition
Input 1	Image + true energy (E_{true})
Input 2	Image + true shower maximum (X_{max}^{true})
Input 3	Image + X_{max}^{true} + E_{true}
Input 4	Image + reconstructed energy (E_{rec})
Input 5	Image + reconstructed shower maximum (X_{max}^{rec})
Input 6	Image + X_{max}^{rec} + E_{rec}

Table 5.4: Definitions of inputs for the CNN.

5.4 Input features

We tested different combinations of inputs for training our CNN using the information of the image, the primary particle energy (E), expressed in TeV, and depth of shower maximum (X_{max})[5]. We used true and reconstructed values of the shower maximum and energy for testing the CNN. In addition, we used two types of images as input in the CNN: a) images from one telescope and b) images from multiple telescopes. In the first case, the image is taken from the first triggered telescope for each event. In the second case, we sum the images from all triggered telescopes into one image for each event, as shown in Fig. 5.6. Choosing the latter approach reduces the number of trainable parameters compared to using a true stereo mode. Finally, each input type is trained using the separated SST and MST images. The combinations of inputs for each type of telescope and approach are listed in Table 5.4.

5.4.1 Energy reconstruction

In this work, we use simulated DL1 data, i.e. calibrated images, which do not include energy nor the reconstructed shower maximum. Since the reconstructed energy is one of the features we plan to include in our algorithm, we use Random Forest (RF) to reconstruct the energy, as it is usually done in the field. We applied the same algorithm to train the RF on cosmic ray events. We evaluated the performance on the test-data set by comparing the reconstructed energy E_{rec} of the RF with the true energy E_{true} of the initial cosmic ray shower. Fig. 5.7 shows the energy 2D histogram of E_{rec} against E_{true} obtained from RF trained for train and predicted on the test data-set. The Pearson correlation coefficient (R^2)

[5] Atmospheric depth where the maximum number of secondary particles is reached in an air shower [g/cm^2]

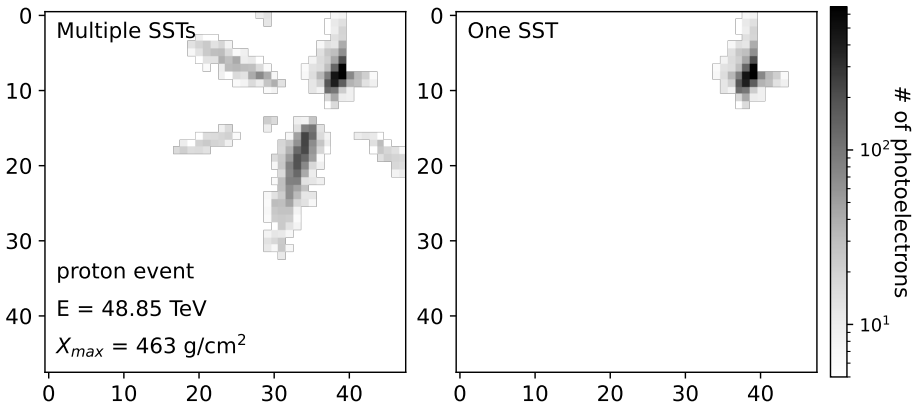

(a) Proton-induced shower.

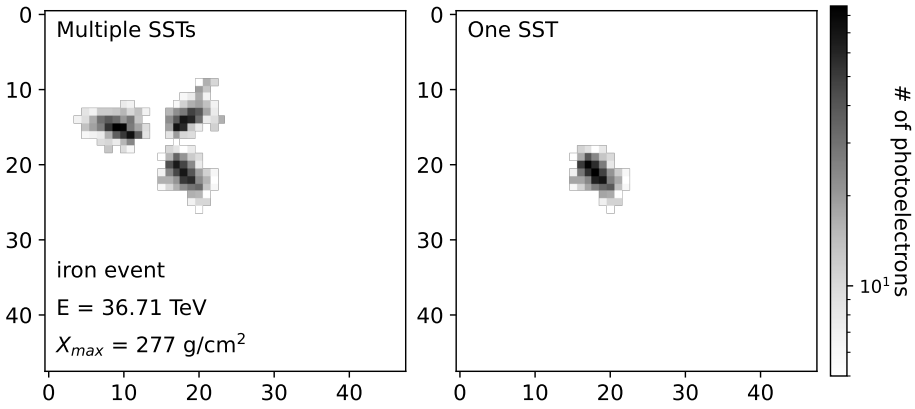

(b) Iron-induced shower.

Figure 5.6: Image of (a) proton-induced and (b) iron-induced shower detected by the camera of an SST. Left: Multiple triggered detections from an event grouped into a single image. Right: One triggered detection for the same event.

measures the strength of the linear correlation between the variables E_{rec} and E_{true} and goes from -1 to 1.

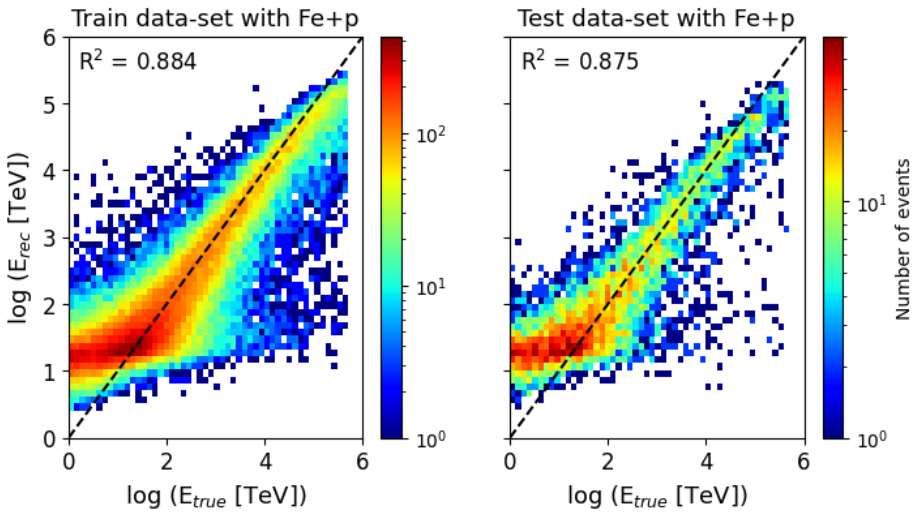

Figure 5.7: Example of the reconstructed energy against true energy obtained from an RF trained with Hillas parameters for the train (right) and test (left) data set.

The $R^2 = 1$ (or -1) describes a perfect linear correlation, while $R^2 = 0$ denotes no linear dependency. For $R^2 > 0.7$ already indicates a strong correlation. As shown in Fig. 5.7, the R^2 for training and test data sets are 0.884 and 0.875, a good indicator of the linear correlation. The typical R^2 for gamma-ray events is $\sim$ 0.96. The relative energy error given by $\Delta E/E_{true} = (E_{rec}$ - $E_{true})/E_{true}$ is computed for each event. The energy range between 1 TeV and 300 TeV is split into seven logarithmic bins, and each event is designated to an energy bin based on its true energy. We computed the distribution of the relative energy error $\Delta E/E_{true}$ for each energy bin and its mean and standard deviation. The mean of $\Delta E/E_{true}$ is called the *energy bias*. The smaller the energy bias and resolution, the higher the accuracy of the energy reconstruction. The *energy resolution* is defined by the standard deviation of $\Delta E/E_{true}$. The energy bias and resolution are shown in Fig. 5.8 for both the train and test data set. The energy resolution obtained for the train and test data set is fairly similar, reaching up to $\sim$ 25 % at the highest energy bin. In contrast, the energy resolution is deficient at the lowest energy bin. The energy bias ranges from -0.38 to 0.26, with a minimum at $\sim$ 10 TeV (except at the lowest energy bin, where the energy bias is around 1.45).

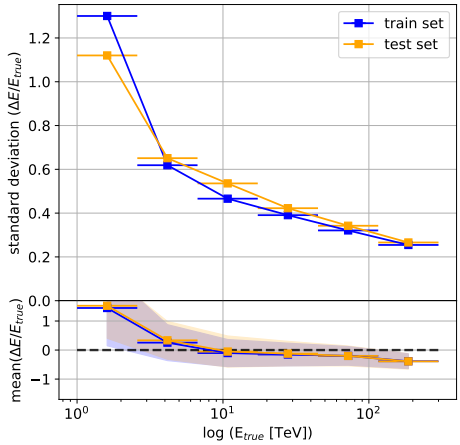

Figure 5.8: Energy resolution (standard deviation of $\Delta E/E_{true}$) on top and energy bias (mean of $\Delta E/E_{true}$) on bottom, against the true energy. The shaded region on the bottom represents one standard deviation.

5.4.2 Shower maximum reconstruction

The depth of the shower maximum, X_{max}, is reconstructed using the package ctapipe based on the Hillas parameters. The distribution of the true and reconstructed for all the events are shown on the upper plot in Fig 5.9. To filter the bad reconstructed values around $\sim$ 800 g/cm^2, we applied a cut in the relative error $\Delta X/X_{max}^{true} = (X_{max}^{reco} - X_{max}^{true})/X_{max}^{true}$ in order to be less than $\pm$ 0.5. The result of applying this cut can be seen on the bottom plot in Fig 5.9.

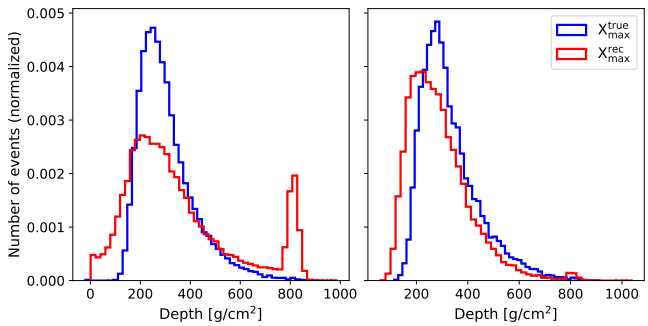

Figure 5.9: Example of the true and reconstructed shower maximum distribution with events considering images from MSTs, before (left) and after (right) applying cut.

5.5 Results

5.5.1 Signal-background separation

According to our CNN, the α_i defined by (5.2) can represent a marginal probability of an event being iron-like, i.e., the *ironness* or α_{Fe}. Therefore, each event can be labelled by its ironness, where an *ironness* = 1 corresponds to an iron event and an *ironness* = 0 corresponds to a proton event. Examples of the *ironness* distributions obtained from a single CNN trained for different kinds of inputs are shown in Fig 5.10 and 5.11 for SSTs and MSTs, respectively. The distributions are the results of using true parameters of shower maximum, energy, and SST/MST images from one or multiple telescopes as inputs for the training and prediction of the CNN.

For SSTs and MSTs (according to Fig 5.10 and 5.11), most iron events are classified with ironness equal to 1 and most proton events are classified with ironness equal to 0 in the case of the inputs: **Image** + $\mathbf{X}_{\max}^{\text{true}}$ + $\mathbf{E}_{\text{true}}$. However, when using the input **Image** + $\mathbf{E}_{\text{true}}$, the ironness distribution is irregular, and the CNN cannot make a good separation on the test data set for the SST case. On the other hand, this last scenario even produces an acceptable result in the case of the MST. The multiple-telescope images indicate a better capability for iron-proton separation in all scenarios with respect to the one-telescope image. Furthermore, in all cases, it is shown that increasing the number of input parameters helps to improve the separation capability.

The previous results were obtained from training and testing using true shower maximum and true energy values. The ironness results, differences aside, still show the same behaviour when using reconstructed parameters as input for training and testing our CNN (see appendix 5.A for ironness distribution using reconstructed parameters). We found that **Image** + $\mathbf{X}_{\max}^{\text{rec}}$ + $\mathbf{E}_{\text{rec}}$ is still the best scenario for both SST and MST using reconstructed inputs. In particular, the multiple SSTs also offer a good separation using only **Image** + $\mathbf{X}_{\max}^{\text{rec}}$. In addition, there is a better distinction in the ironness distributions for SST images than MST images, either using true or reconstructed parameters. On the other hand, the **Image** + $\mathbf{E}_{\text{rec}}$ case always shows irregular distributions independently of the telescope and type of input for reconstructed values. It is even possible to see this behaviour on the top plot in Fig. 5.10, where a significant fraction of true proton events are misclassified as iron events (with ironness close to 1). This suggests that the energy would not be a sufficient parameter for the separation.

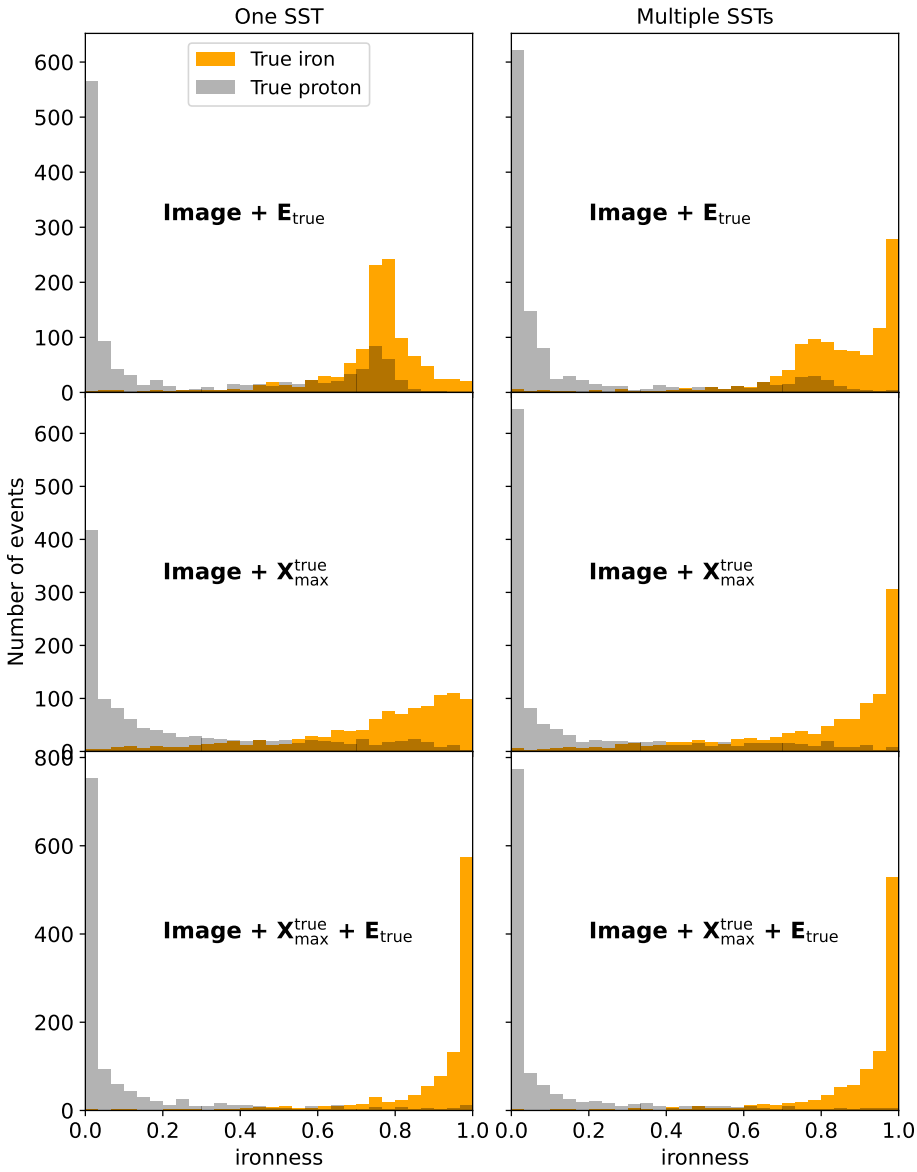

Figure 5.10: Example of the *ironness* distributions obtained from one trained CNN using the different types of inputs labelled on each plot. The plots on the left correspond to training with images from one SST, and the plots on the right to images using several SSTs. The inputs used are the true values.

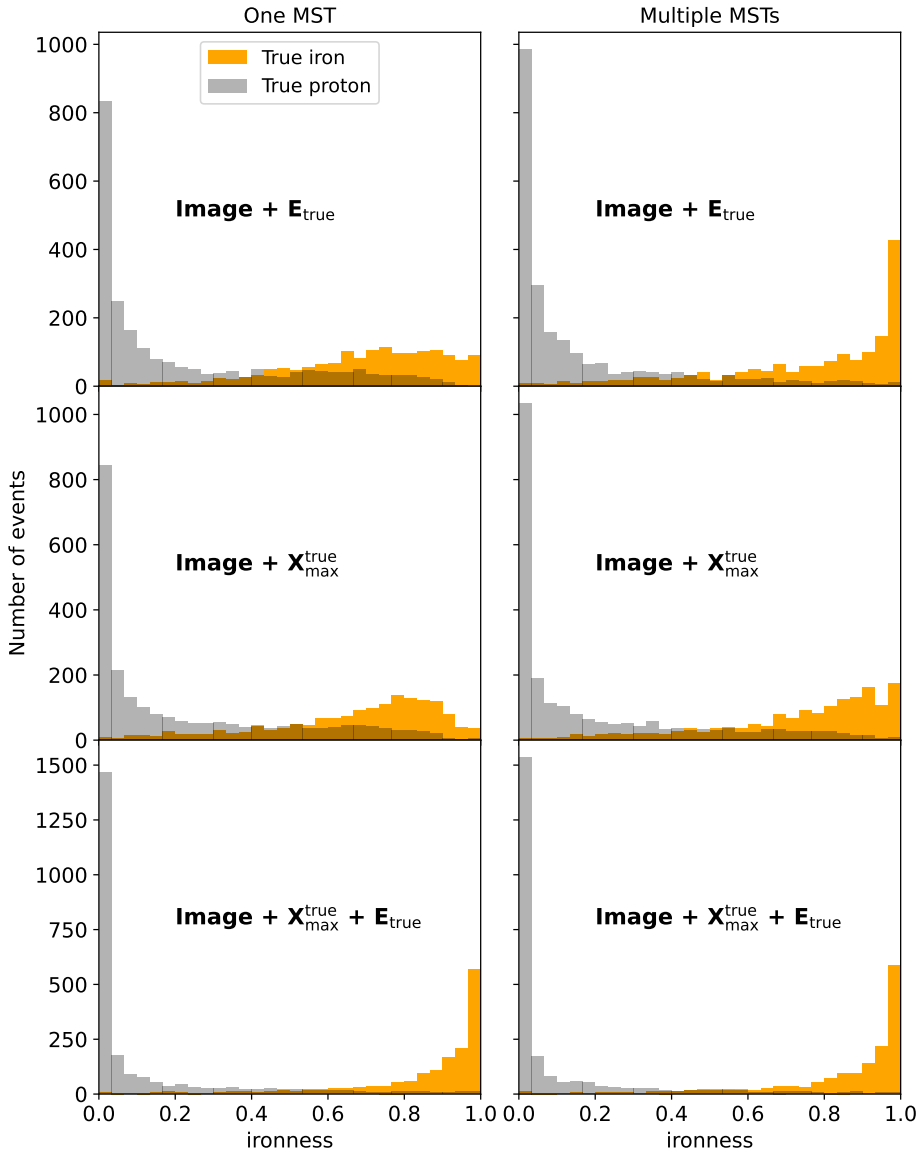

Figure 5.11: Example of the *ironness* distributions obtained from one trained CNN using the different types of inputs labelled on each plot. The plots on the left correspond to images from one MST, and the plots on the right to images using multiple MSTs. The inputs used are the true values.

We trained several independent CNNs with the same architecture to guarantee our results. Tables 5.5 and 5.6 show the average accuracy values obtained from five independently trained CNN architectures. These results correspond to predictions made on the testing set. From the accuracy scores listed in these tables, we can see that our CNNs can distinguish between categories of cosmic ray shower images very ably, with accuracy scores larger than 80% with small fluctuations in most cases.

We found that the accuracy scores were slightly better when we trained and tested the CNN using true parameters of shower maximum and energy instead of the reconstructed values. The accuracy results were also better when using multiple-telescope images than just one-telescope images for both SST and MST. In the case of SST images, the input **Image** + $\mathbf{X}_{\mathrm{max}}^{\mathrm{rec}}$ + $\mathbf{E}_{\mathrm{rec}}$ showed an improvement of around 2% in the average accuracy when using multiple-telescope images rather than just one-telescope. In the case of MST images, the gain was around 4% for the same input.

The **Image** + $\mathbf{X}_{\mathrm{max}}^{\mathrm{rec}}$ was also a good CNN input, offering an average accuracy of about 80 % and 82 % using one and multiple-telescope SST images, respectively. For MSTs, the same input showed a score of around 80 % only for multiple-telescope images. On the other hand, the input **Image** + $\mathbf{E}_{\mathrm{rec}}$ showed the lower accuracy scores ranging from 70 % to 78 % in all cases. The last result shows that the energy does not provide enough information to separate the iron proton events. A possible explanation is that proton-induced showers at higher energies produce a comparable quantity of photons to iron-induced showers of lower energies, resulting in similar images. As a result, there could be a misclassification of some images. This suggests that energy is not a sufficient parameter for separation. However, the energy information, in combination with the maximum shower parameter, helps to improve the iron-proton classification, as we will see in the following sections.

Inputs using SST Image	**Average accuracy (std dev)**	
	one	multiple
Image + E_{true}	0.837 (0.019)	0.884 (0.006)
Image + X_{max}^{true}	0.818 (0.004)	0.848 (0.001)
Image + X_{max}^{true} + E_{true}	0.925 (0.006)	0.939 (0.003)
Image + E_{rec}	0.734 (0.007)	0.780 (0.003)
Image + X_{max}^{rec}	0.802 (0.002)	0.829 (0.002)
Image + X_{max}^{rec} + E_{rec}	0.827 (0.003)	0.840 (0.005)

Table 5.5: Testing set average accuracy scores by training our CNN with different types of inputs and using a mixed set of iron and proton shower images from SSTs in the energy range from 1 TeV to 300 TeV. The values in parentheses correspond to one standard deviation.

Inputs using MST Image	**Average accuracy (std dev)**	
	one	multiple
Image + E_{true}	0.804 (0.003)	0.876 (0.005)
Image + X_{max}^{true}	0.805 (0.002)	0.837 (0.017)
Image + X_{max}^{true} + E_{true}	0.921 (0.002)	0.925 (0.002)
Image + E_{rec}	0.707 (0.002)	0.749 (0.050)
Image + X_{max}^{rec}	0.768 (0.001)	0.801 (0.005)
Image + X_{max}^{rec} + E_{rec}	0.785 (0.004)	0.820 (0.004)

Table 5.6: Testing set average accuracy scores by training our CNN with different types of inputs and using a mixed set of iron and proton shower images from MSTs in the energy range from 1 TeV to 300 TeV. The values in parentheses correspond to one standard deviation.

5.5.2 Determination of the optimal threshold value for iron identification

Studying the efficiency as a function of the ironness helps to determine the *optimal threshold value* for the ironness in order to maximize the separation of the categories. For a fixed threshold ironness α_{Fe}, the iron efficiency is defined as $n_{Fe} = \frac{TP}{TP+FN}$, i.e., the fraction of true iron events correctly classified as iron events with *ironness* $\geqslant \alpha_{Fe}$. Correspondingly, the proton efficiency is given by $n_p = \frac{FP}{FP+TN}$, i.e., the fraction of true iron events misclassified as proton events with *ironness* $< \alpha_{Fe}$. Examples of iron (solid line) and proton (dashed line) efficiencies as a function of the thresholds ironness α_{Fe} for one-telescope (red) and multiple-telescope images (blue) are shown in Fig. 5.12 and Fig. 5.13 for SSTs and MSTs, respectively. Each plot shows the results for a CNN trained with different types of inputs as labelled on them.

A good classifier is given by a high iron efficiency and a low proton efficiency for a fixed ironness threshold. The point of the maximum separation between the iron and proton efficiency curves determines the optimal threshold ironness, as can be seen in Fig 5.12. The bottom plots of both Fig 5.12 and 5.13 show efficiencies decreasing steadily when increasing the ironness value in contrast to the upper plot. The bottom plots also show similar behaviour with different optimal threshold values when using one and multiple telescopes. The summary of the optimal threshold values is listed in Table 5.7 for all input cases. We found there is no tendency for the optimal threshold value when using one or multiple telescopes for MST or SST. In order to outperform the best separation for each scenario, we use each of the best thresholds based on table 5.7.

CNN inputs	**SST**		**MST**	
	one	multiple	one	multiple
Img + E_{true}	0.47	0.53	0.37	0.44
Img + X^{true}_{max}	0.51	0.40	0.40	0.40
Img + X^{true}_{max} + E_{true}	0.44	0.58	0.47	0.39
Img + E_{rec}	0.51	0.48	0.44	0.43
Img + X^{rec}_{max}	0.50	0.45	0.41	0.41
Img + X^{rec}_{max} + E_{rec}	0.52	0.50	0.46	0.42

Table 5.7: Optimal threshold values obtained in a single CNN trained with different inputs. The optimal threshold values are separated by the telescope type and image.

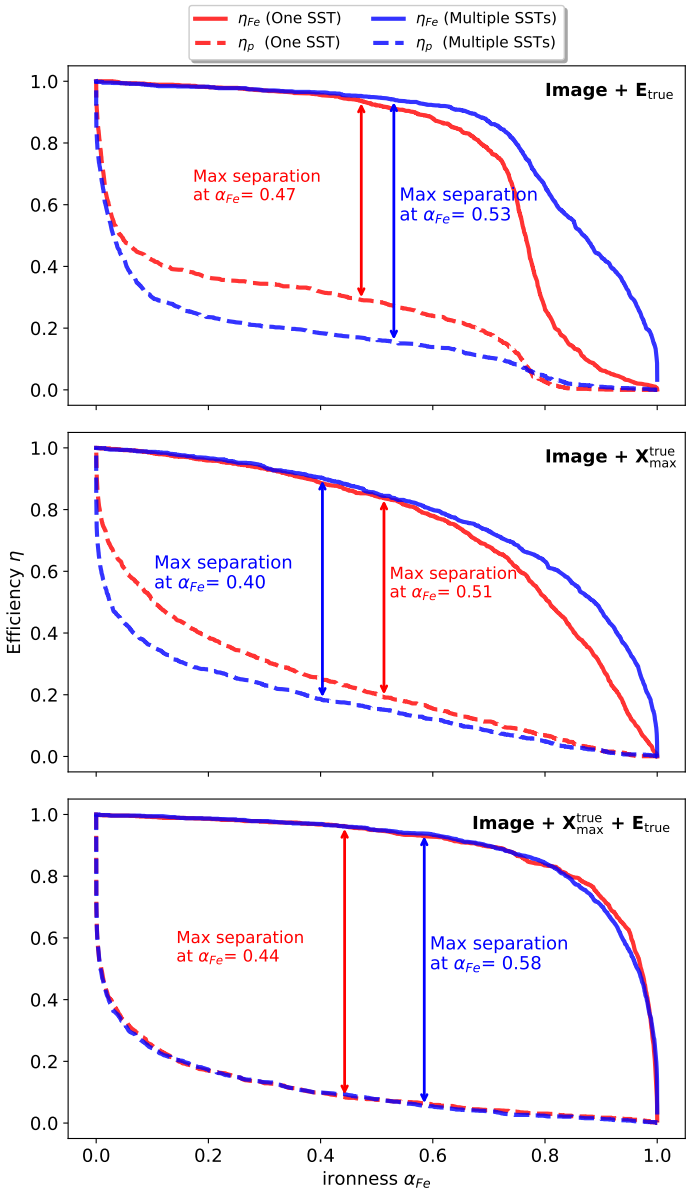

Figure 5.12: Iron efficiency η and proton efficiency as a function of the ironness thresholds α_{Fe} for the SSTs images. The CNN was trained using the different input types labelled on each plot. The inputs used are the true values.

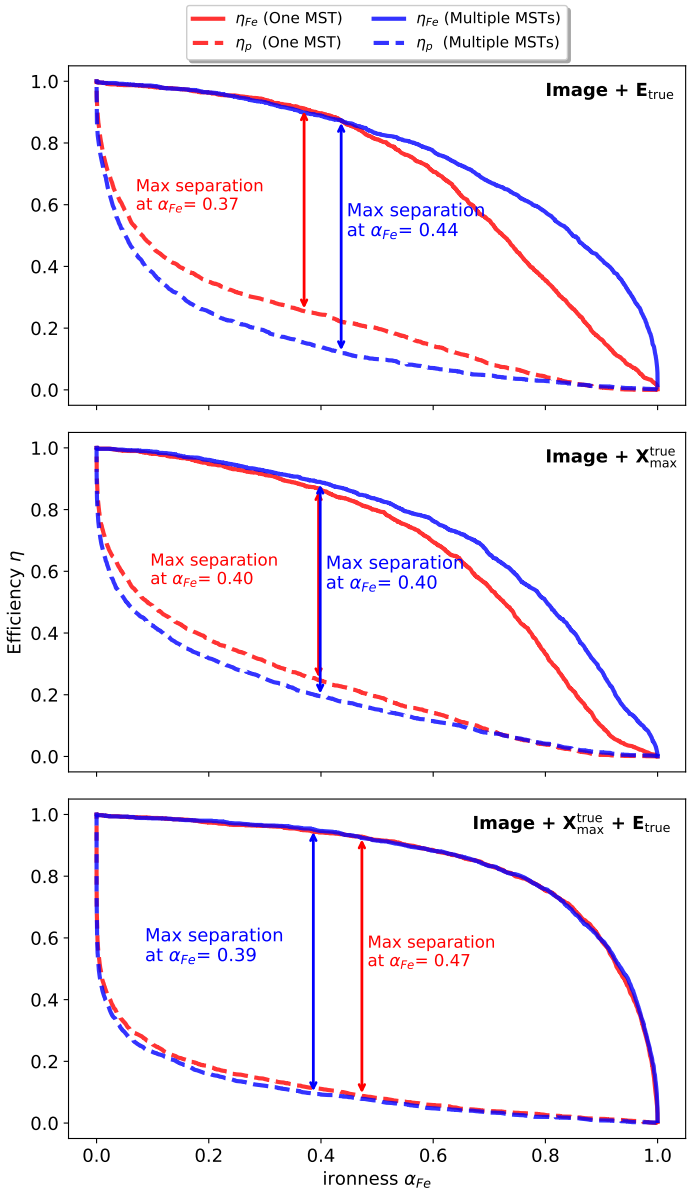

Figure 5.13: Iron efficiency η and proton efficiency as a function of the ironness thresholds α_{Fe} for the MSTs images. The CNN was trained using the different input types labelled on each plot. The inputs used are the true values.

5.5.3 ROC curve

The ROC curve also helps to evaluate the performance of the trained CNN on the test data set measuring the AUC scores. An example of the average ROC curve and AUC values obtained from five independently trained CNNs is shown in Fig 5.14 and 5.15. As a reference, the dashed black line represents an algorithm that makes random classifications. We can see that the ROC curves obtained from the input **Image** + $\mathbf{X}_{\mathrm{max}}^{\mathrm{true}}$ + $\mathbf{E}_{\mathrm{true}}$, either for SSTs or MSTs, are notably steeper than the other cases, indicating the best scenario as expected from the ironness distribution and the efficiency-vs-threshold results discussed previously.

For the input **Image** + $\mathbf{X}_{\mathrm{max}}^{\mathrm{true}}$ + $\mathbf{E}_{\mathrm{true}}$ and according to Fig. 5.14, the average AUC values of 0.977 and 0.984 for one-telescope and multiple-telescope SST images are significantly larger than in other cases. This means the CNN trained with this input, particularly with multiple-telescope images, provides a higher signal-background separation than just using the image plus another parameter. On the other hand, in the MST case, there is no difference in the AUC values ($\sim$ 0.97) between one-telescope and multiple-telescope (see bottom plot in Fig. 5.15).

When we compared the results using reconstructed parameters, the input **Image** + $\mathbf{X}_{\mathrm{max}}^{\mathrm{rec}}$ + $\mathbf{E}_{\mathrm{rec}}$ with multiple-telescope is still the best scenario but with less AUC values than using true parameters: 0.923 for SST and 0.901 for MST (see Fig. 5.24 and 5.25 in appendix 5.C). Interestingly, the input **Image** + $\mathbf{E}_{\mathrm{rec}}$ shows many fluctuations along the proton efficiency in multiple MST scenarios, which means a high variability in the predictions of the independently trained CNNs (see 5.C).

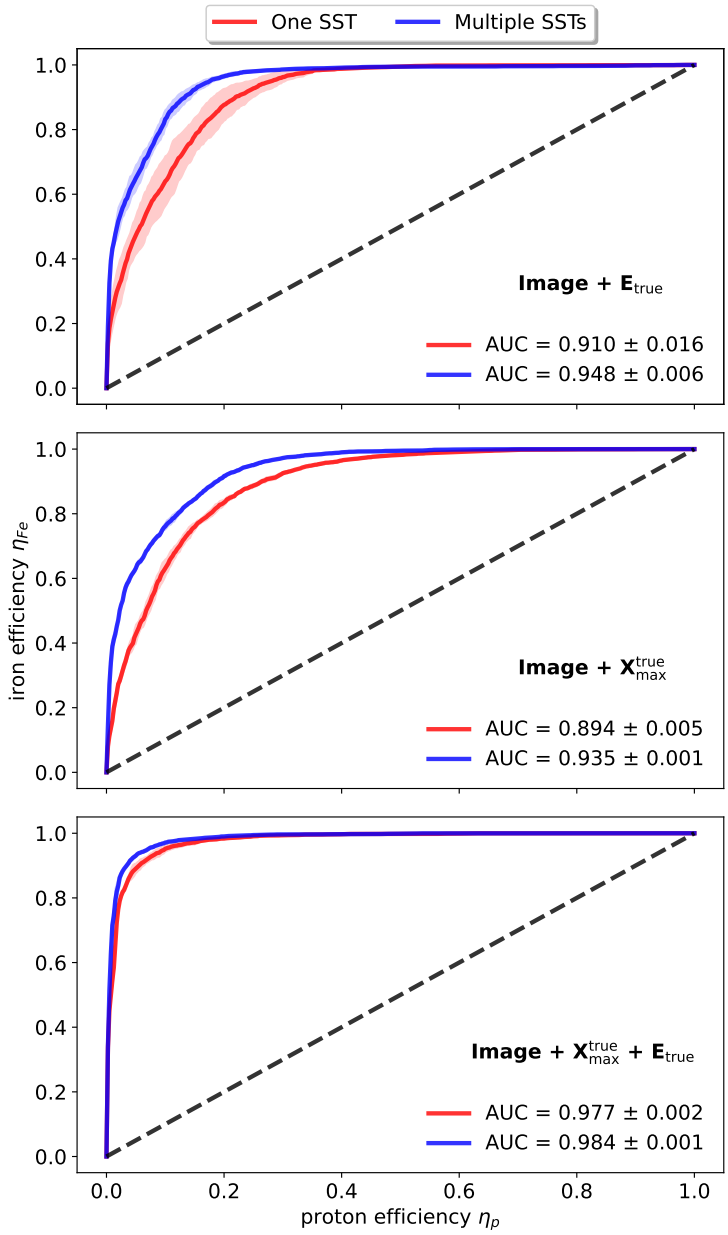

Figure 5.14: Average ROC curves and average AUC values obtained from 5 CNNs independently trained with images from one and multiple SSTs. The shaded region corresponds to one standard deviation. The dashed black line represents the curve from a CNN that makes a random classification.

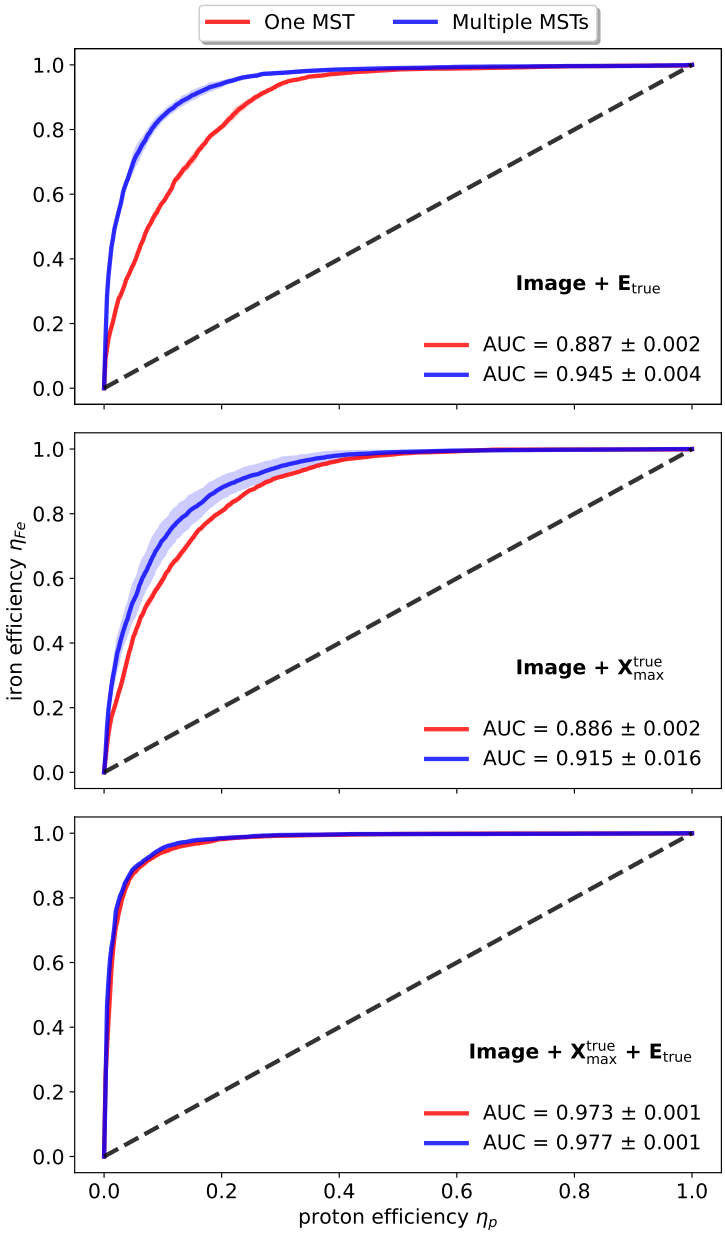

Figure 5.15: Average ROC curves and average AUC values obtained from 5 CNNs independently trained with images from one and multiple MSTs. The shaded region corresponds to one standard deviation. The dashed black line represents the curve from a CNN that makes a random classification.

5.5.4 Energy dependence of efficiency

To check the robustness of our CNN classifier, we also performed the efficiency for different energy bins (from 1 TeV to 300 TeV) using the optimal threshold ironness values[6]. Fig. 5.16 shows the average efficiency of iron and protons for the SST case as a function of the true energy for different inputs. Their corresponding values are listed in Table 5.8. In these plots, the best scenario corresponds to the case of the maximum separation between both curves, iron and proton efficiency. As expected, the bottom panel in Fig. 5.16 with **Image + $\mathbf{X}_{\max}^{\text{true}}$ + $\mathbf{E}_{\text{true}}$** gives the best scenario because the iron efficiency goes from 0.89 to 0.98 along the energy (except in the second energy bin, which is 0.72) and the proton efficiency increase from $\sim$ 0.01 to $\sim$ 0.13 for multiple telescopes (see Table 5.8).

Similarly, the middle panel of Fig. 5.16 with **Image + $\mathbf{X}_{\max}^{\text{true}}$** also provides a higher iron efficiency ($>$ 0.8) for all energies. In contrast, the proton efficiency decreases from 0.25 to 0.06 as a function of the energy for multiple SSTs. However, the top panel of Fig. 5.16 with **Image + $\mathbf{E}_{\text{true}}$** provides the worse case; despite having a higher iron efficiency, the proton efficiency is relatively higher ($>$ 0.5 for high energies) compare to the other cases.

Energy bin	Test-set **SST**		**Image** + $\mathbf{E}_{true}$		**Image** + $\mathbf{X}_{max}^{true}$		**Image** + $\mathbf{E}_{true}$ + $\mathbf{X}_{max}^{true}$	
[TeV]	# Fe / # p	Img	η_{Fe}	η_p	η_{Fe}	η_p	η_{Fe}	η_p
1.79	2/268	one	0.00	0.00	1.00	0.22	1.00	0.03
		mul	0.00	0.00	1.00	0.21	1.00	0.01
4.64	35/406	one	0.28	0.02	0.88	0.28	0.77	0.06
		mul	0.29	0.00	0.84	0.25	0.72	0.05
12.01	382/251	one	0.95	0.45	0.86	0.16	0.92	0.10
		mul	0.96	0.23	0.87	0.14	0.89	0.03
31.07	330/157	one	0.97	0.67	0.89	0.11	0.98	0.21
		mul	0.99	0.45	0.95	0.13	0.98	0.09
80.38	208/83	one	0.97	0.63	0.81	0.10	0.99	0.21
		mul	0.99	0.53	0.92	0.11	0.97	0.13
207.97	116/45	one	0.92	0.60	0.62	0.08	0.97	0.20
		mul	0.89	0.54	0.87	0.06	0.95	0.13

Table 5.8: Iron (η_{Fe}) and proton (η_p) efficiency values of Fig. 5.16 for each energy bin considering one, multiple SSTs and true parameters as inputs. The number of iron and proton events in the test data set per energy bin is also provided.

[6]Values taken from Table 5.7

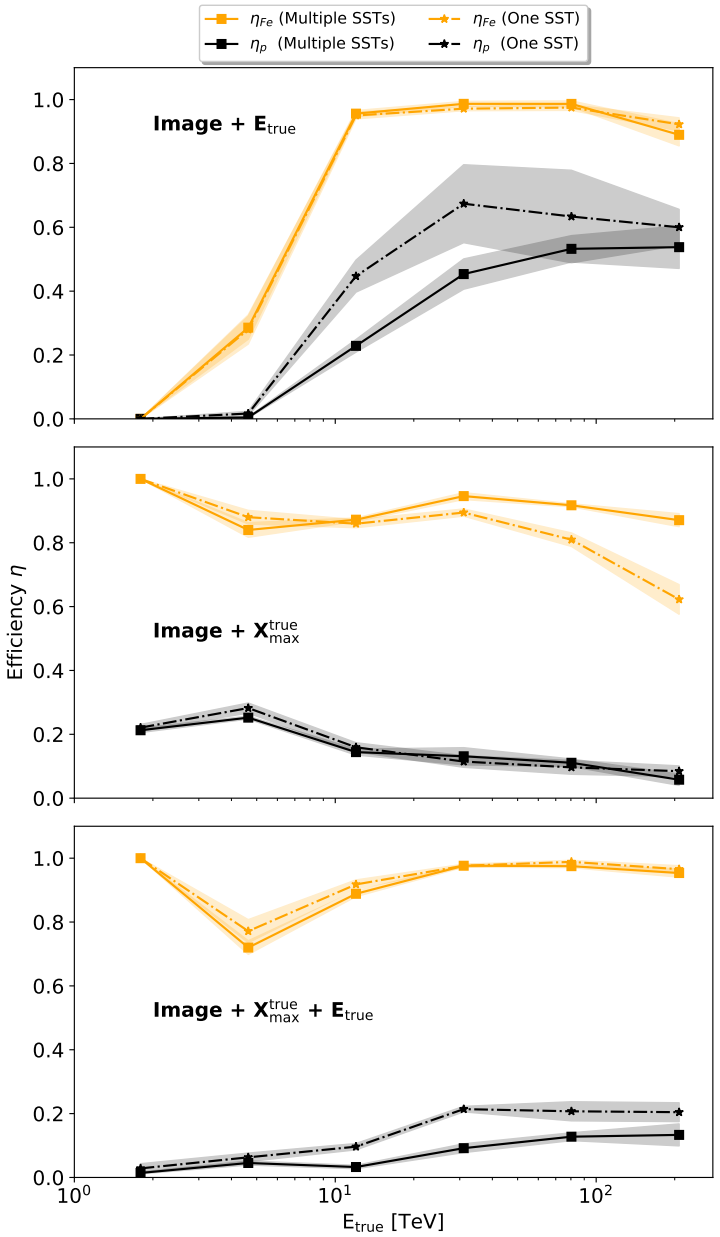

Figure 5.16: Average iron (orange) and proton (black) efficiency with *ironness* threshold fixed by Table 5.7 and obtained from 5 trained CNNs as a function of the true energy. CNNs were independently trained with images from one and multiple SSTs with different inputs.

From Table 5.8, we can also note that the number of events for the first energy bin is just two, resulting in an iron efficiency of 1.00 and 0.00 in some cases. However, the tendency for the rest of the bins is to increase with the energy as expected. Similar behaviour occurred when we trained the CNN with MST images. The bottom plot in Fig. 5.17 also shows the best scenario for MST with iron efficiency ranging from 0.93 to 0.98 along the energy bins. The proton efficiency is $\sim$ 0.10 in most of the bins for multiple telescopes (except at 207.97 TeV with 0.23).

Unlike the SST case, MST images with only X_{max}^{true} do not provide a good iron efficiency at higher energies, as seen in the middle panel of Fig. 5.17. On the other hand, despite having good iron efficiency in the scenario with the image and the energy, they do not produce a low proton efficiency as required.

Similar tendencies in the iron and proton efficiency occurred when we trained the CNN with the reconstructed shower maximum and reconstructed energy for SST and MST images as can be seen in Fig. 5.18 and 5.19, respectively[7]. The best case is still **Image + X_{max}^{rec} + E_{rec}** for either one or multiple telescopes. But in all cases, the efficiency worsens depending on the energy bin. For instance, iron efficiency decreases by 11% for multiple SST and MST at 31 TeV. The proton efficiency also worsens by about 1% at 31 TeV for multiple SSTs.

Energy bin	Test-set **MST**		**Image** + E_{true}		**Image** + X_{max}^{true}		**Image** + E_{true} + X_{max}^{true}	
[TeV]	# Fe / # p	Img	η_{Fe}	η_p	η_{Fe}	η_p	η_{Fe}	η_p
1.79	046/844	one	0.08	0.00	0.99	0.33	0.81	0.04
		mul	0.28	0.01	1.00	0.26	0.98	0.09
4.64	381/626	one	0.83	0.21	0.96	0.29	0.87	0.08
		mul	0.79	0.10	0.95	0.23	0.93	0.09
12.01	513/399	one	0.95	0.46	0.89	0.14	0.93	0.10
		mul	0.92	0.20	0.88	0.11	0.95	0.09
31.07	335/242	one	0.96	0.57	0.87	0.09	0.96	0.10
		mul	0.95	0.25	0.89	0.11	0.97	0.11
80.38	207/149	one	0.95	0.65	0.75	0.07	0.96	0.15
		mul	0.93	0.31	0.81	0.08	0.96	0.13
207.97	107/060	one	0.94	0.74	0.51	0.10	0.92	0.17
		mul	0.84	0.44	0.66	0.20	0.93	0.23

Table 5.9: Iron (η_{Fe}) and proton (η_p) efficiency values of Fig. 5.17 for each energy bin considering one, multiple MSTs and true parameters as inputs. The number of iron and proton events in the test data set per energy bin is also provided.

[7] see Tables 5.10 and 5.11 in the appendix 5.D for more information

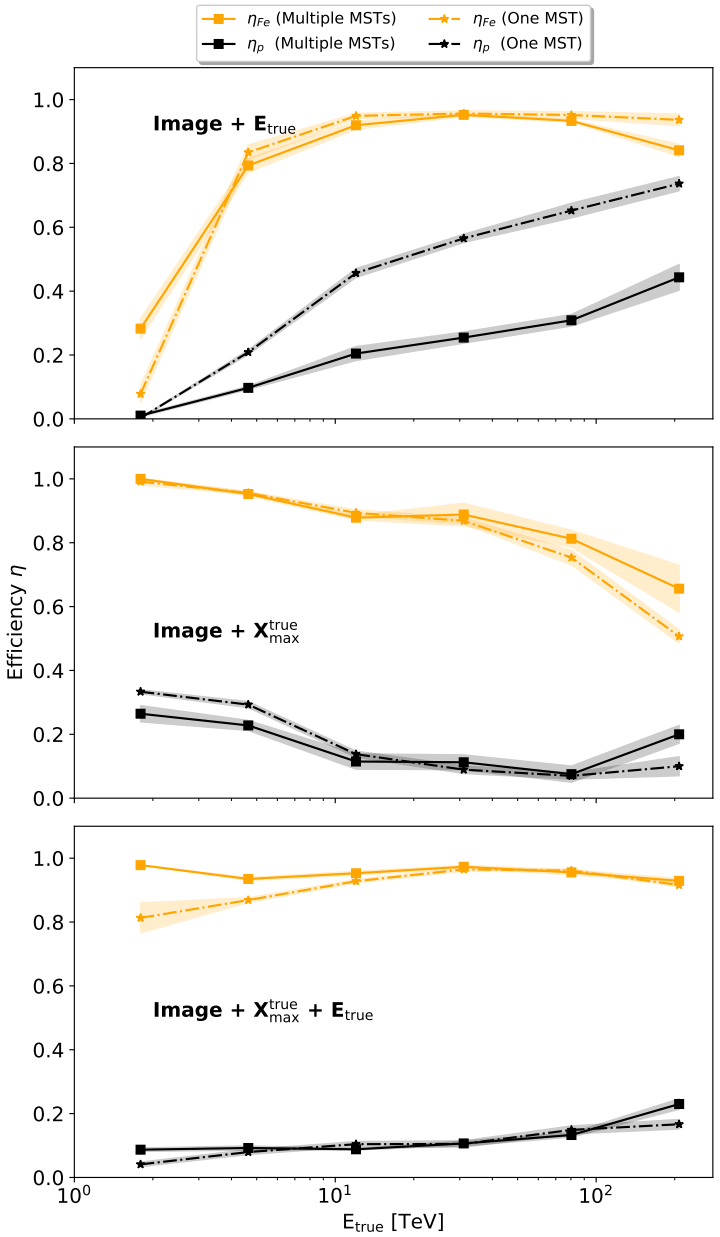

Figure 5.17: Average iron (orange) and proton (black) efficiency with *ironness* threshold fixed by Table 5.7 and obtained from 5 trained CNNs as a function of the true energy. CNNs were independently trained with images from one and multiple MSTs with different inputs.

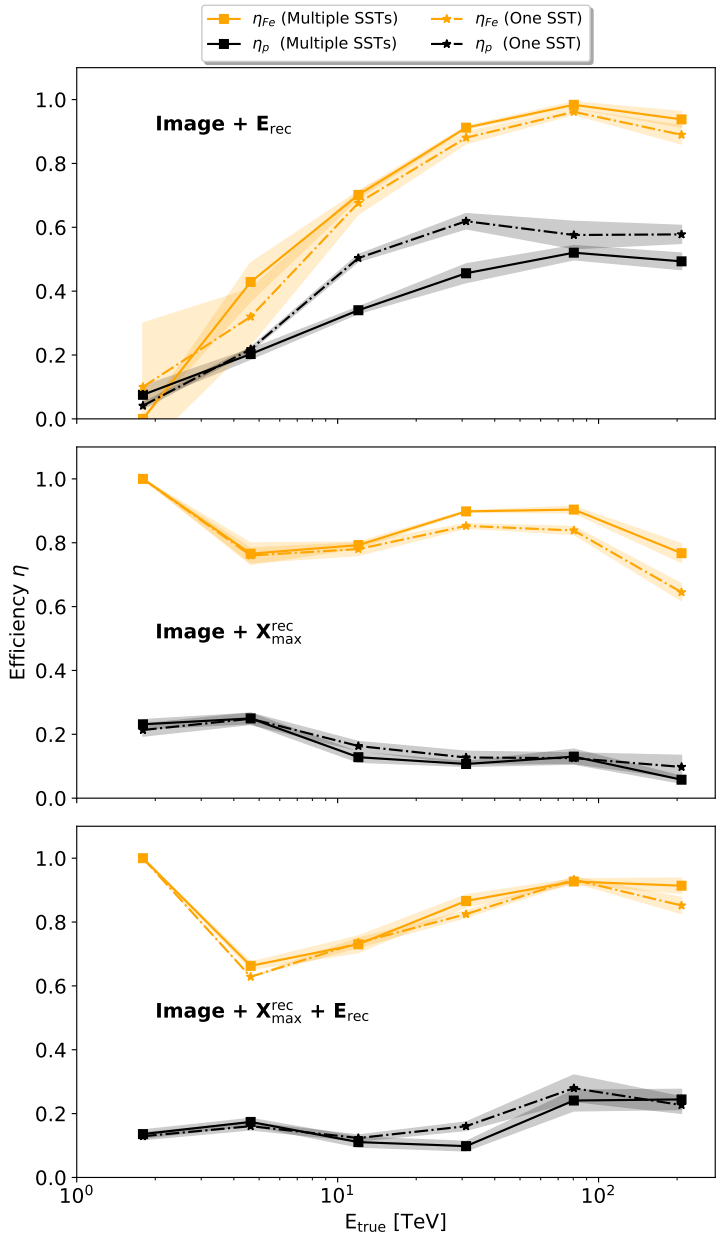

Figure 5.18: Average iron (orange) and proton (black) efficiency with *ironness* threshold fixed by Table 5.7 and obtained from 5 trained CNNs as a function of the true energy. CNNs were independently trained with images from one and multiple SSTs with different inputs.

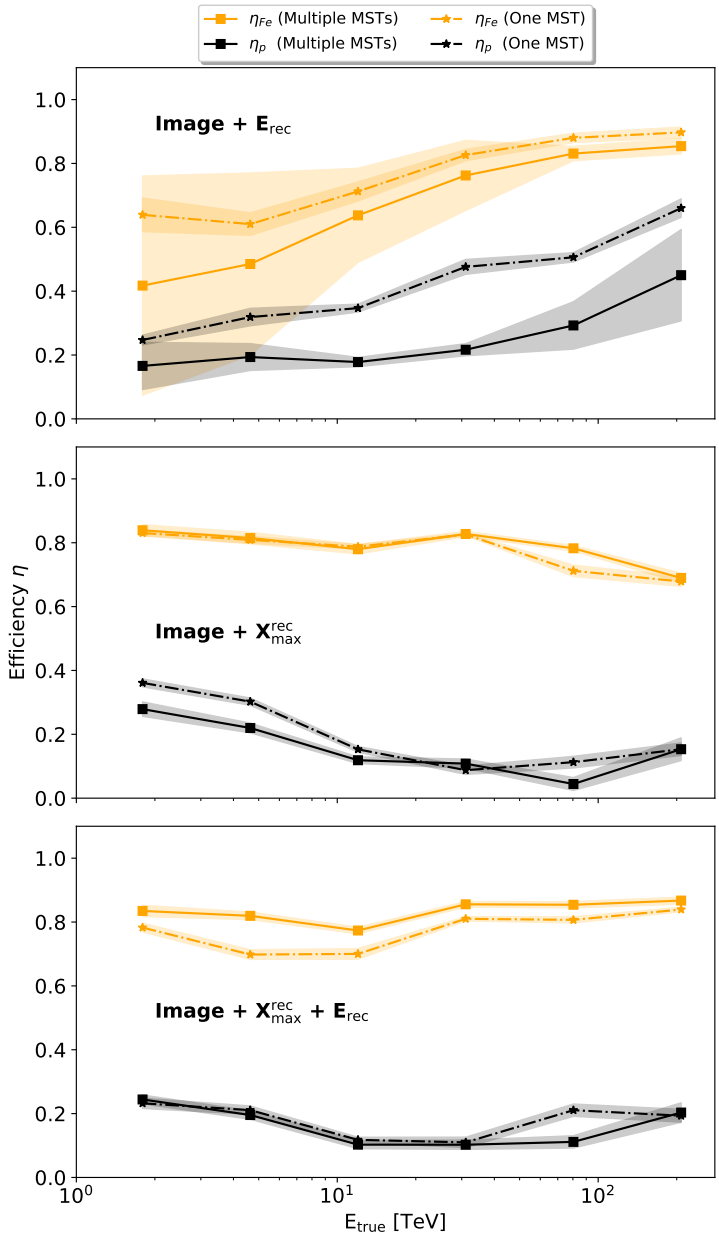

Figure 5.19: Average iron (orange) and proton (black) efficiency with *ironness* threshold fixed by Table 5.7 and obtained from 5 trained CNNs as a function of the true energy. CNNs were independently trained with images from one and multiple MSTs with different inputs.

5.6 Conclusion

We have developed a machine-learning approach for identifying cosmic-ray nuclei, mainly proton and iron nuclei, using simulated images from the upcoming Cherenkov Telescope Array (CTA). We addressed this problem using the approach of convolutional neural networks (CNNs), which are commonly used tools for image classification.

We trained our CNN with proton and iron shower images detected by the SSTs and MSTs, including two extra parameters: the shower energy (E) and the depth of the shower maximum (X_{max}). We used true and reconstructed values of these parameters for training the CNN. In addition, two types of images were used as input for the CNN: images recorded by one triggered telescope and images recorded by all triggered telescopes. In the latter case, this is not a proper stereo mode but a stacking of images on top of each other. As a result, we found that our CNN with images from SSTs can separate iron events from protons with $>$ 93 % accuracy when using true parameters as input and $>$ 84 % when using the reconstructed parameters as input. Also, MSTs can separate iron from protons with $>$ 92 % accuracy when using true parameters as input and $>$ 82 % when using the reconstructed parameters as input.

Our study also showed that predictions from trained CNN only using image and energy provided good iron efficiencies at high energies, either using MSTs or SSTs. However, in both MST and SST, the proton efficiency at high energies was larger than 40% along the energy, which means significant contamination according to our definition of proton efficiency (misclassified proton as iron events).

On the other hand, CNNs trained with the image, energy, and depth of shower maximum showed the best results for MST and SST images. For SSTs, the iron efficiency remained almost constant throughout the energy for the multiple telescopes, using **Image + $\mathbf{X}_{\mathrm{max}}$ + E** or even using simply **Image + $\mathbf{X}_{\mathrm{max}}$**, either with true or reconstructed values. The iron efficiency reached a maximum efficiency of 98 % at 31 TeV using true parameters as inputs. In addition, the proton efficiency was below 13 % for all energy bins. In the case of using reconstructed parameters as inputs, the iron efficiency is still higher than 87 % for energy bins greater than 31 TeV using multiple SSTs. Proton efficiency remains below 24 %.

For MSTs, the iron efficiency also remained almost constant throughout the energy for multiple telescopes, using **Image + $\mathbf{X}_{\mathrm{max}}$ + E** either with true or reconstructed values. The iron efficiency reached a maximum efficiency of 97 % at 31 TeV using true parameters as inputs. The proton efficiency was below 23 % for all energy bins. In the case of using reconstructed

parameters as inputs, the iron efficiency is higher than 85 % for energy bins greater than 31 TeV using multiple MSTs. Proton efficiency remains below 24 %.

In addition, the constant behaviour along the energy was supported by the mean ROC curve reaching a value of AUC = 0.984 and 0.977 for multiple SSTs and MSTs. We have shown that our CNN has the capability to detect the features of the IACT images and classify heavy from light cosmic-ray events.

Appendix 5.A Ironness distributions

5.A.1 For SSTs and reconstructed parameters

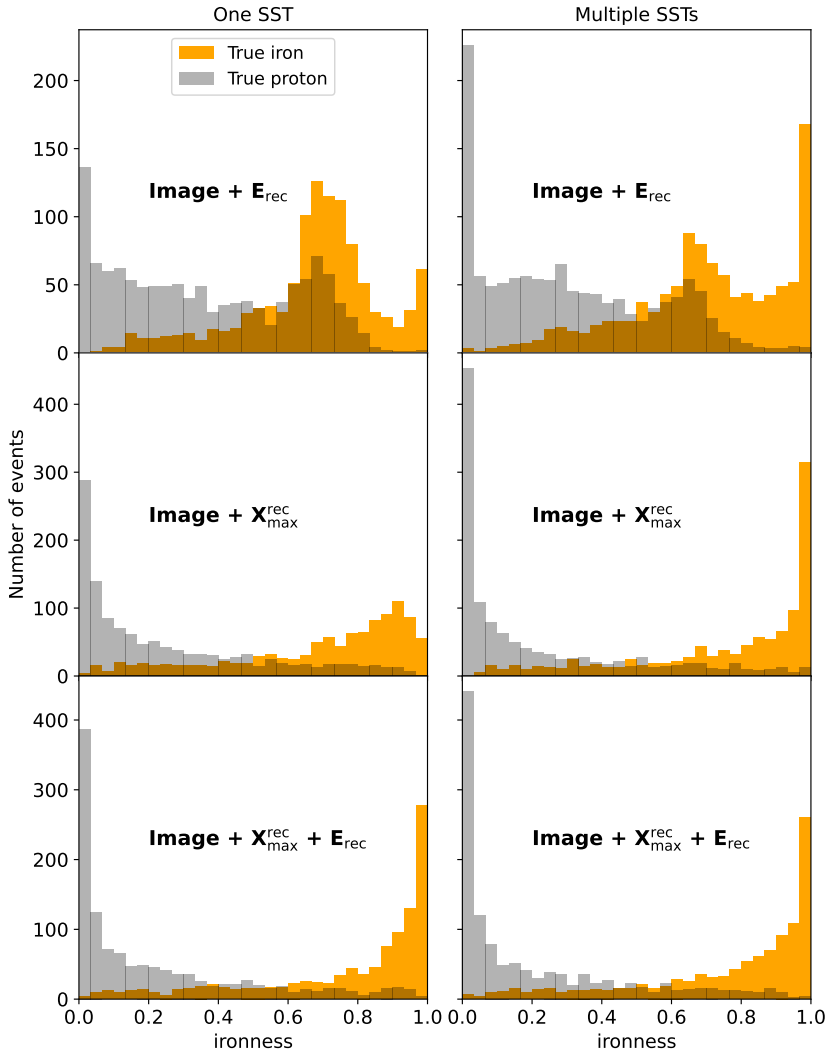

Figure 5.20: Example of the *ironness* distributions obtained from one trained CNN using the different types of inputs labelled on each plot. The plots on the left correspond to images from one SST, and the plots on the right to images using multiple SSTs. The inputs used are the reconstructed values.

5.A.2 For MSTs and reconstructed parameters

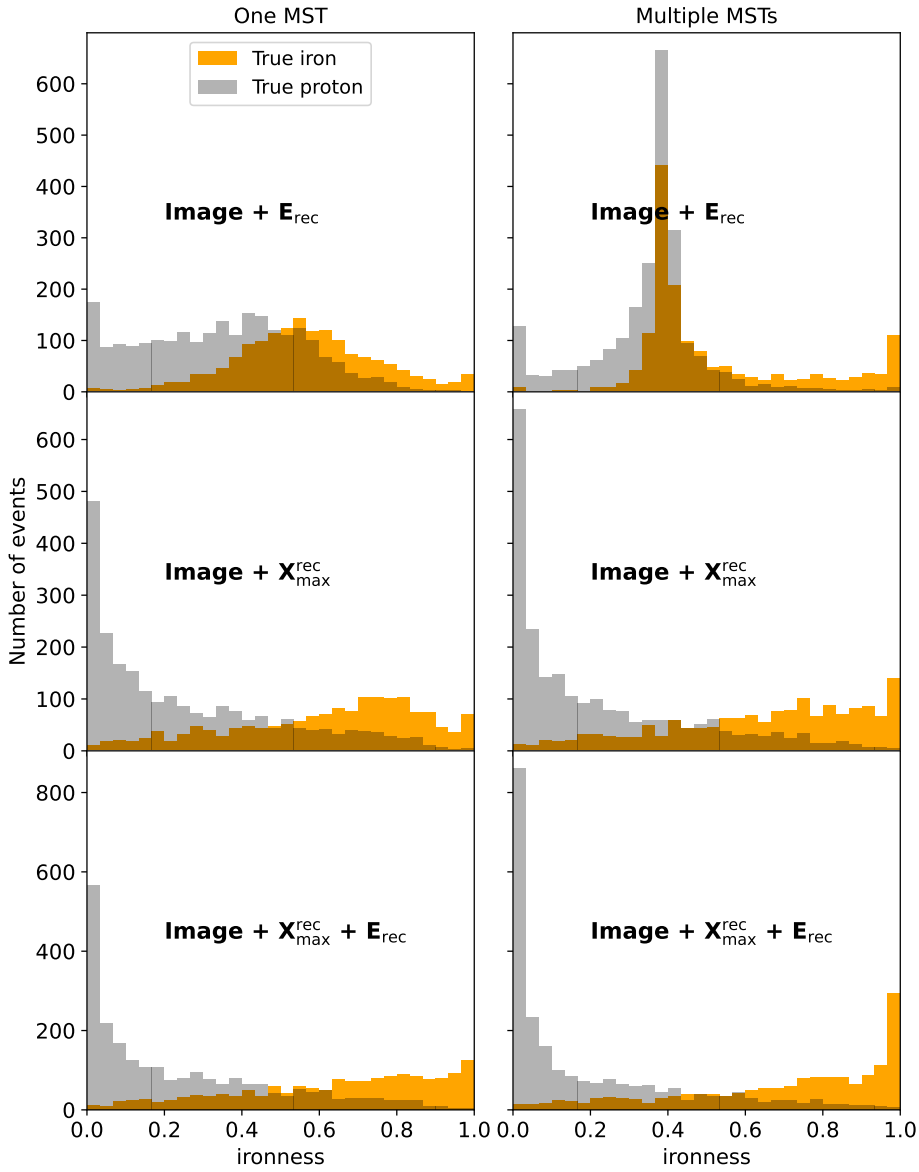

Figure 5.21: Example of the *ironness* distributions obtained from one trained CNN using the different types of inputs labelled on each plot. The plots on the left correspond to images from one MST, and the plots on the right to images using multiple MSTs. The inputs used are the reconstructed values.

Appendix 5.B Efficiency as a function of the ironness

5.B.1 For SSTs and reconstructed parameters

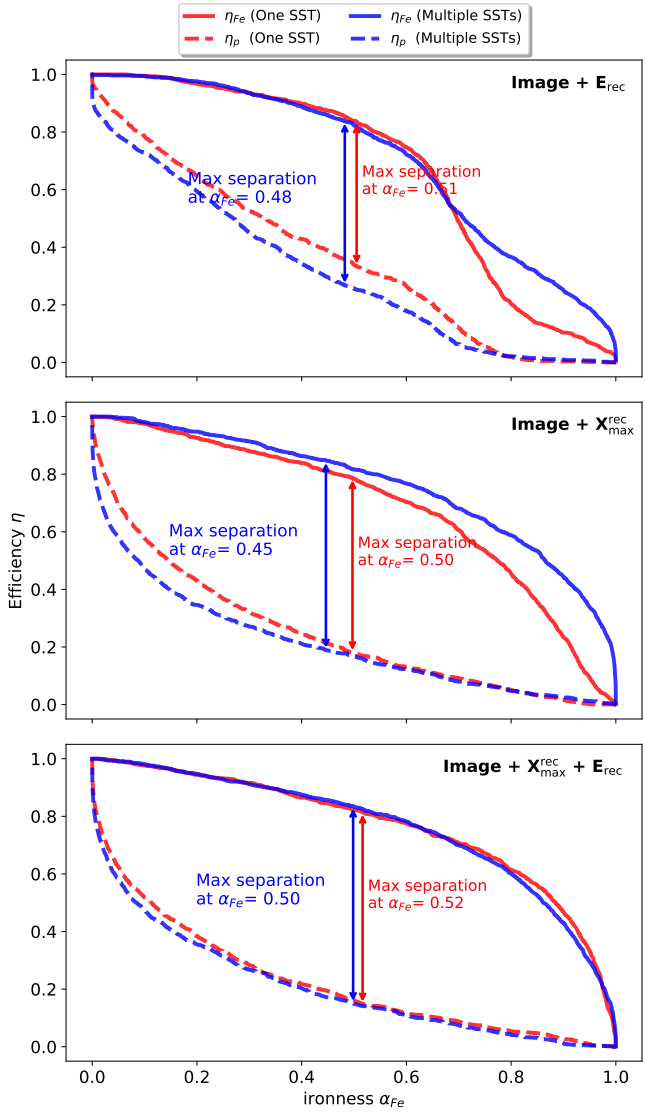

Figure 5.22: Iron efficiency η and proton efficiency as a function of the ironness thresholds α_{Fe} for the SSTs images. The CNN was trained using the different input types labelled on each plot. The inputs used are the reconstructed values.

5.B.2 For MSTs and reconstructed parameters

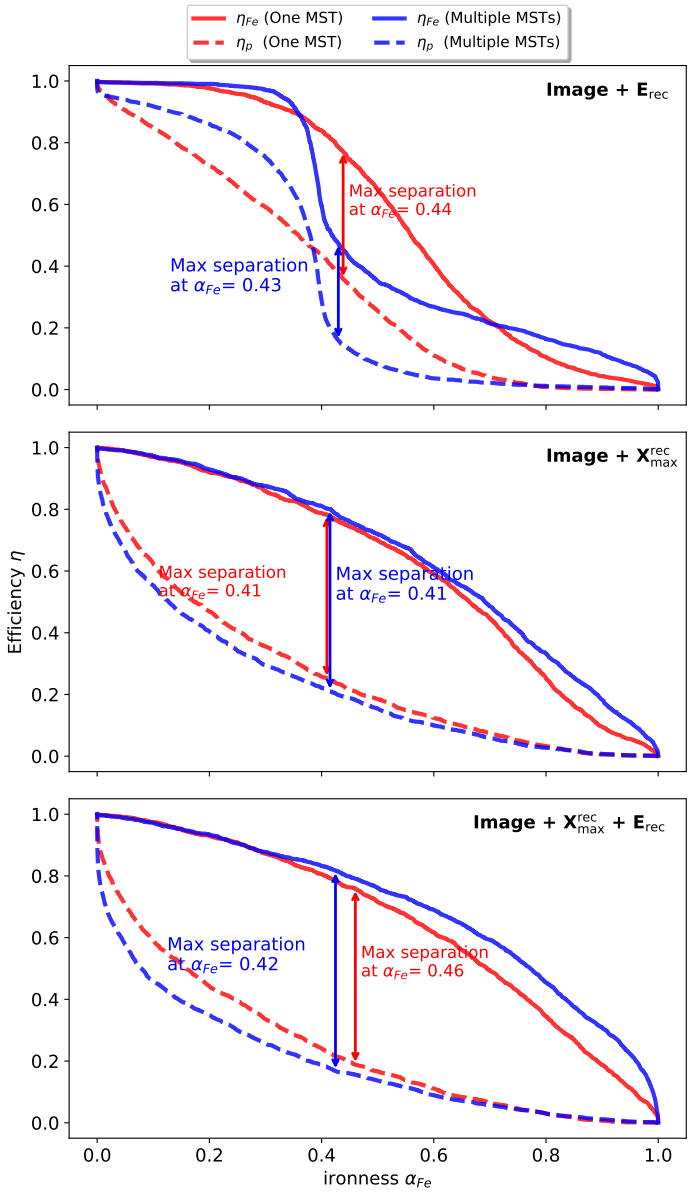

Figure 5.23: Iron efficiency η and proton efficiency as a function of the ironness thresholds α_{Fe} for the MSTs images. The CNN was trained using the different input types labelled on each plot. The inputs used are the reconstructed values.

Appendix 5.C Mean ROC curves

5.C.1 For SSTs and reconstructed parameters

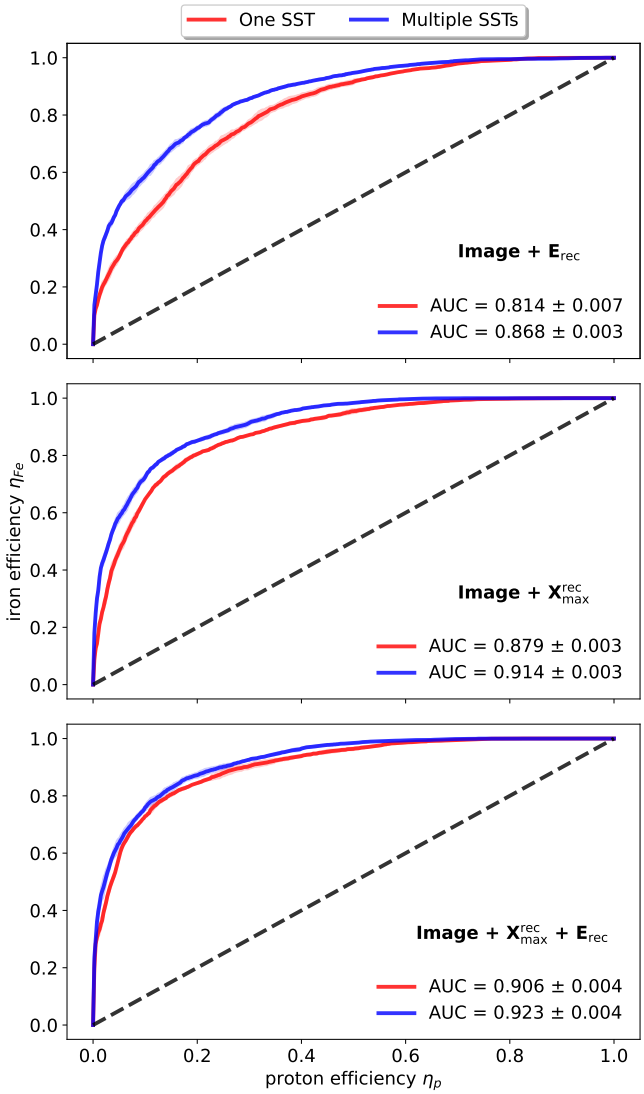

Figure 5.24: Average ROC curves and average AUC values obtained from 5 CNNs independently trained with images from one and multiple SSTs. The shaded region corresponds to one standard deviation. The dashed black line represents the curve from a CNN that makes a random classification.

5.C.2 For MSTs and reconstructed parameters

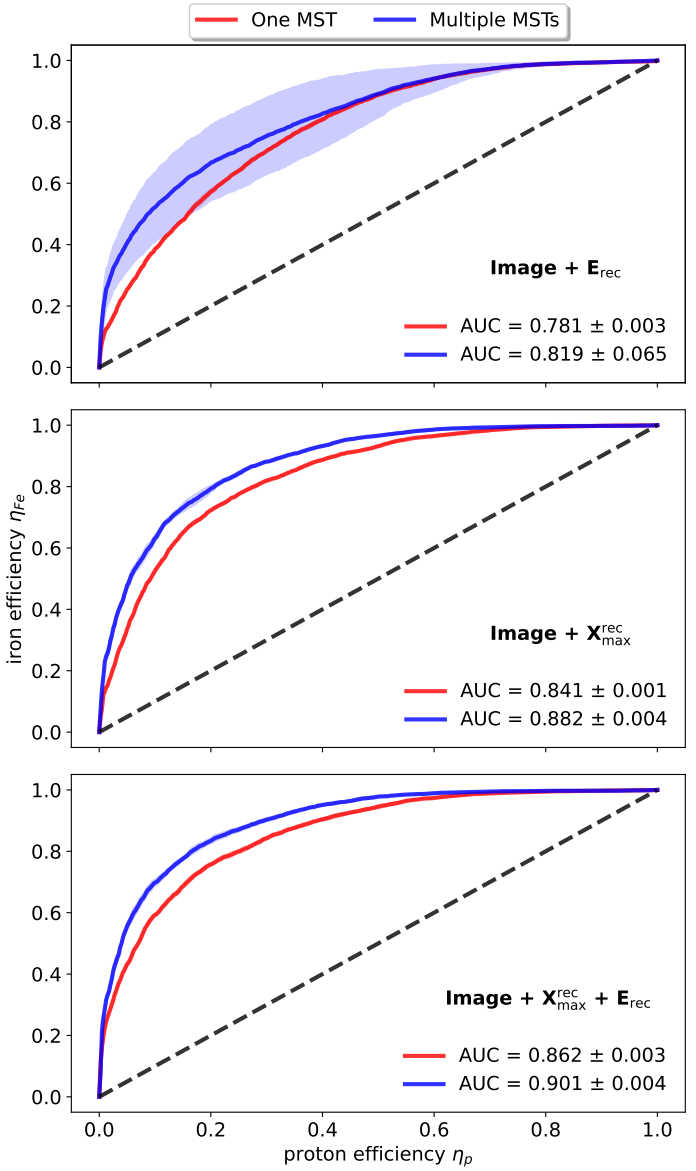

Figure 5.25: Average ROC curves and average AUC values obtained from 5 CNNs independently trained with images from one and multiple MSTs. The shaded region corresponds to one standard deviation. The dashed black line represents the curve from a CNN that makes a random classification.

Appendix 5.D Mean efficiency vs. energy

5.D.1 For SSTs and reconstructed parameters

Energy bin	Test-set **SST**		**Image + $\mathbf{E}_{rec}$**		**Image + $\mathbf{X}_{max}^{rec}$**		**Image + $\mathbf{E}_{rec}$ + $\mathbf{X}_{max}^{rec}$**	
[TeV]	# Fe / # p	Img	η_{Fe}	η_p	η_{Fe}	η_p	η_{Fe}	η_p
1.79	002/268	one	0.10	0.04	1.00	0.21	1.00	0.13
		mul	0.00	0.08	1.00	0.23	1.00	0.14
4.64	035/406	one	0.32	0.22	0.76	0.25	0.63	0.16
		mul	0.43	0.20	0.77	0.25	0.66	0.17
12.01	382/251	one	0.68	0.50	0.78	0.16	0.74	0.12
		mul	0.70	0.34	0.79	0.13	0.73	0.11
31.07	330/157	one	0.88	0.62	0.85	0.13	0.82	0.16
		mul	0.91	0.46	0.90	0.11	0.87	0.10
80.38	208/083	one	0.96	0.58	0.84	0.13	0.93	0.28
		mul	0.98	0.52	0.90	0.13	0.93	0.24
207.97	116/045	one	0.89	0.58	0.64	0.10	0.85	0.23
		mul	0.94	0.49	0.77	0.06	0.91	0.24

Table 5.10: Iron (η_{Fe}) and proton (η_p) efficiency values of Fig. 5.18 for each energy bin considering one, multiple SSTs and reconstructed parameters as inputs. The number of iron and proton events in the test data set per energy bin is also provided.

5.D.2 For MSTs and reconstructed parameters

Energy bin	Test-set **MST**		**Image + $\mathbf{E}_{rec}$**		**Image + $\mathbf{X}_{max}^{rec}$**		**Image + $\mathbf{E}_{rec}$ + $\mathbf{X}_{max}^{rec}$**	
[TeV]	# Fe / # p	Img	η_{Fe}	η_p	η_{Fe}	η_p	η_{Fe}	η_p
1.79	046/844	one	0.64	0.25	0.83	0.36	0.78	0.23
		mul	0.42	0.17	0.84	0.28	0.83	0.24
4.64	381/626	one	0.61	0.32	0.81	0.30	0.70	0.21
		mul	0.49	0.19	0.81	0.22	0.82	0.20
12.01	513/399	one	0.71	0.35	0.79	0.15	0.70	0.12
		mul	0.64	0.18	0.78	0.12	0.77	0.10
31.07	335/242	one	0.83	0.48	0.83	0.09	0.81	0.11
		mul	0.76	0.22	0.83	0.11	0.86	0.10
80.38	207/149	one	0.88	0.51	0.71	0.11	0.81	0.21
		mul	0.83	0.29	0.78	0.04	0.85	0.11
207.97	107/060	one	0.90	0.66	0.68	0.15	0.84	0.19
		mul	0.85	0.45	0.69	0.15	0.87	0.20

Table 5.11: Iron (η_{Fe}) and proton (η_p) efficiency values of Fig. 5.19 for each energy bin considering one, multiple MSTs and reconstructed parameters as inputs. The number of iron and proton events in the test data set per energy bin is also provided.

Bibliography

[1] E. Lorenz and R. Wagner. Very-high energy gamma-ray astronomy. A 23-year success story in high-energy astroparticle physics. *European Physical Journal H*, 37(3):459–513, August 2012. doi: 10.1140/epjh/e2012-30016-x.

[2] Malcolm S. Longair. *High energy astrophysics*. Cambridge University Press, 3rd ed. Cambridge, 2011.

[3] A. M. Bykov, D. C. Ellison, A. Marcowith, and S. M. Osipov. Cosmic ray production in supernovae. *Space Sci. Rev.*, 214(1):41, 2018. doi: 10.1007/s11214-018-0479-4.

[4] Paolo Lipari and Silvia Vernetto. The shape of the cosmic ray proton spectrum. *Astroparticle Physics*, 120:102441, 2020. ISSN 0927-6505. doi: https://doi.org/10.1016/j.astropartphys.2020.102441. URL https://www.sciencedirect.com/science/article/pii/S0927650520300141.

[5] Vincent Tatischeff, John C Raymond, Jean Duprat, et al. The origin of Galactic cosmic rays as revealed by their composition. *Monthly Notices of the Royal Astronomical Society*, 508(1):1321–1345, 10 2021. ISSN 0035-8711. doi: 10.1093/mnras/stab2533. URL https://doi.org/10.1093/mnras/stab2533.

[6] Pierre Cristofari. The Hunt for Pevatrons: The Case of Supernova Remnants. *Universe*, 7(9):324, 2021. doi: 10.3390/universe7090324.

[7] Pierre Auger, P. Ehrenfest, R. Maze, et al. Extensive cosmic-ray showers. *Rev. Mod. Phys.*, 11:288–291, Jul 1939. doi: 10.1103/RevModPhys.11.288. URL https://link.aps.org/doi/10.1103/RevModPhys.11.288.

[8] B. S. Acharya et al. *Science with the Cherenkov Telescope Array*. WSP, 11 2018. ISBN 978-981-327-008-4. doi: 10.1142/10986.

[9] Julian Sitarek et al. Physics performance of the upgraded MAGIC telescopes obtained with Crab Nebula data. In *33rd International Cosmic Ray Conference*, page 0074, 8 2013.

[10] Georges Vasileiadis. The h.e.s.s experimental project. *Nuclear Instruments and Methods in Physics Research Section A: Accelerators, Spectrometers, Detectors and Associated Equipment*, 553(1):268–273, 2005. ISSN 0168-9002. doi: https://doi.org/10.1016/j.nima.2005.08.056. URL https://www.sciencedirect.com/science/article/pii/S0168900205016086. Proceedings of the fifth International Workshop on Ring Imaging Detectors.

[11] N. Park and VERITAS Collaboration. Performance of the VERITAS experiment. In *34th International Cosmic Ray Conference (ICRC2015)*,

volume 34 of *International Cosmic Ray Conference*, page 771, July 2015. doi: 10.22323/1.236.0771.

[12] A. M. Hillas. Cerenkov Light Images of EAS Produced by Primary Gamma Rays and by Nuclei. In *19th International Cosmic Ray Conference (ICRC19), Volume 3*, volume 3 of *International Cosmic Ray Conference*, page 445, August 1985.

[13] M. de Naurois, J. Guy, A. Djannati-Atai, et al. Application of an Analysis Method Based on a Semi-Analytical Shower Model to the First H.E.S.S. Telescope. In *International Cosmic Ray Conference*, volume 5 of *International Cosmic Ray Conference*, page 2907, July 2003.

[14] M. Lemoine-Goumard, B. Degrange, and M. Tluczykont. Selection and 3D-Reconstruction of Gamma-Ray-induced Air Showers with a Stereoscopic System of Atmospheric Cherenkov Telescopes. *Astropart. Phys.*, 25:195–211, 2006. doi: 10.1016/j.astropartphys.2006.01.005.

[15] Robert Parsons, Michael Gajdus, and Thomas Murach. HESS II Data Analysis with ImPACT. *PoS*, ICRC2015:826, 2016. doi: 10.22323/1.236.0826.

[16] Michelle Torres and Francisco Cantú. Learning to see: Convolutional neural networks for the analysis of social science data. *Political Analysis*, 30(1):113–131, 2022. doi: 10.1017/pan.2021.9.

[17] Tianmei Guo, Jiwen Dong, Henjian Li, and Yunxing Gao. Simple convolutional neural network on image classification. In *2017 IEEE 2nd International Conference on Big Data Analysis (ICBDA)*, pages 721–724, 2017. doi: 10.1109/ICBDA.2017.8078730.

[18] C Yao, Y Zhang, and H Liu. Application of convolutional neural network in classification of high resolution agricultural remote sensing images. *The international archives of the photogrammetry, remote sensing and spatial information sciences*, 42:989–992, 2017.

[19] Yunjie Liu, Evan Racah, Prabhat, et al. Application of Deep Convolutional Neural Networks for Detecting Extreme Weather in Climate Datasets. *arXiv e-prints*, art. arXiv:1605.01156, May 2016. doi: 10.48550/arXiv.1605.01156.

[20] Dalya Baron. Machine Learning in Astronomy: a practical overview. *arXiv e-prints*, art. arXiv:1904.07248, April 2019. doi: 10.48550/arXiv.1904.07248.

[21] Edward J. Kim and Robert J. Brunner. Star-galaxy classification using deep convolutional neural networks. MNRAS, 464(4):4463–4475, February 2017. doi: 10.1093/mnras/stw2672.

[22] Christina Hillig. *Analyzing The Cosmic Ray Spectrum Based On Imaging Atmospheric Cherenkov Telescope Data Using Deep Learning*

Methods. URL https://ecap.nat.fau.de/wp-content/uploads/2019/04/2019_Hillig_Master.pdf.

[23] Songshaptak De, Writasree Maitra, Vikram Rentala, and Arun M. Thalapillil. Deep learning techniques for imaging air Cherenkov telescopes. *Phys. Rev. D*, 107(8):083026, 2023. doi: 10.1103/PhysRevD.107.083026.

[24] D. Nieto, A. Brill, B. Kim, and T. B. Humensky. Exploring deep learning as an event classification method for the Cherenkov Telescope Array. *arXiv e-prints*, art. arXiv:1709.05889, September 2017. doi: 10.48550/arXiv.1709.05889.

[25] S. Spencer, T. Armstrong, J. Watson, et al. Deep learning with photosensor timing information as a background rejection method for the Cherenkov Telescope Array. *Astroparticle Physics*, 129:102579, May 2021. doi: 10.1016/j.astropartphys.2021.102579.

[26] T. Miener, D. Nieto, R. López-Coto, et al. The performance of the MAGIC telescopes using deep convolutional neural networks with CTLearn. *arXiv e-prints*, art. arXiv:2211.16009, November 2022. doi: 10.48550/arXiv.2211.16009.

[27] D. Nieto, T. Miener, A. Brill, et al. Reconstruction of IACT Events Using Deep Learning Techniques with CTLearn. In Jose Enrique Ruiz, Francesco Pierfedereci, and Peter Teuben, editors, *Astronomical Society of the Pacific Conference Series*, volume 532 of *Astronomical Society of the Pacific Conference Series*, page 191, July 2022.

[28] Pietro Grespan, Mikael Jacquemont, Rubèn López-Coto, et al. Deep-learning-driven event reconstruction applied to simulated data from a single Large-Sized Telescope of CTA. *arXiv e-prints*, art. arXiv:2109.14262, September 2021. doi: 10.48550/arXiv.2109.14262.

[29] R. D. Parsons and S. Ohm. Background rejection in atmospheric Cherenkov telescopes using recurrent convolutional neural networks. *European Physical Journal C*, 80(5):363, May 2020. doi: 10.1140/epjc/s10052-020-7953-3.

[30] T. Miener, R. López-Coto, J. L. Contreras, et al. IACT event analysis with the MAGIC telescopes using deep convolutional neural networks with CTLearn. *arXiv e-prints*, art. arXiv:2112.01828, December 2021. doi: 10.48550/arXiv.2112.01828.

[31] Jacob Bieker. Using Deep Learning for Gamma Ray Source Detection at the First G-APD Cherenkov Telescope (FACT). In *American Astronomical Society Meeting Abstracts #232*, volume 232 of *American Astronomical Society Meeting Abstracts*, page 220.03, June 2018.

[32] Karen Simonyan and Andrew Zisserman. Very Deep Convolutional Networks for Large-Scale Image Recognition. *arXiv e-prints*, art. arXiv:1409.1556, September 2014. doi: 10.48550/arXiv.1409.1556.

[33] Alex Krizhevsky, Ilya Sutskever, and Geoffrey E Hinton. Imagenet classification with deep convolutional neural networks. In F. Pereira, C.J. Burges, L. Bottou, and K.Q. Weinberger, editors, *Advances in Neural Information Processing Systems*, volume 25. Curran Associates, Inc., 2012. URL https://proceedings.neurips.cc/paper_files/paper/2012/file/c399862d3b9d6b76c8436e924a68c45b-Paper.pdf.

[34] Christian Szegedy, Wei Liu, Yangqing Jia, et al. Going Deeper with Convolutions. *arXiv e-prints*, art. arXiv:1409.4842, September 2014. doi: 10.48550/arXiv.1409.4842.

[35] Kaiming He, Xiangyu Zhang, Shaoqing Ren, and Jian Sun. Deep Residual Learning for Image Recognition. *arXiv e-prints*, art. arXiv:1512.03385, December 2015. doi: 10.48550/arXiv.1512.03385.

[36] The Cherenkov Telescope Array Consortium, :, B. S. Acharya, et al. Science with the Cherenkov Telescope Array. *arXiv e-prints*, art. arXiv:1709.07997, September 2017. doi: 10.48550/arXiv.1709.07997.

[37] J.A. Barrio. Status of the large size telescopes and medium size telescopes for the cherenkov telescope array observatory. *Nuclear Instruments and Methods in Physics Research Section A: Accelerators, Spectrometers, Detectors and Associated Equipment*, 952:161588, 2020. ISSN 0168-9002. doi: https://doi.org/10.1016/j.nima.2018.11.047. URL https://www.sciencedirect.com/science/article/pii/S016890021831622X. 10th International Workshop on Ring Imaging Cherenkov Detectors (RICH 2018).

[38] G. Tagliaferri, A. Antonelli, T. Arnesen, et al. The small-sized telescope of CTAO. In Heather K. Marshall, Jason Spyromilio, and Tomonori Usuda, editors, *Ground-based and Airborne Telescopes IX*, volume 12182, page 121820K. International Society for Optics and Photonics, SPIE, 2022. doi: 10.1117/12.2627956. URL https://doi.org/10.1117/12.2627956.

[39] Capdevielle J. et al Heck D., Knapp J. *Corsika a monte-carlo code to simulate extensive air showers*. 1998. URL https://web.ikp.kit.edu/corsika/physics_description/corsika_phys.pdf.

[40] Konrad Bernlohr. Simulation of Imaging Atmospheric Cherenkov Telescopes with CORSIKA and sim_telarray. *Astropart. Phys.*, 30: 149–158, 2008. doi: 10.1016/j.astropartphys.2008.07.009.

[41] Karl Kosack, Michele Peresano, and on behalf of the CTA Consortium. ctapipe: A Low-level Data Processing Framework for the Cherenkov Telescope Array. *PoS*, ICRC2019:717, 2020. doi: 10.22323/1.358.0717.

[42] Karl Kosack, Maximilian Linhoff, Jason Watson, et al. cta-observatory/ctapipe: v0.18.1 – 2023-03-17, March 2023. URL `https://doi.org/10.5281/zenodo.7744259`.

[43] Daniel Nieto Castao, Ari Brill, Qi Feng, et al. Studying deep convolutional neural networks with hexagonal lattices for imaging atmospheric Cherenkov telescope event reconstruction. *PoS*, ICRC2019:753, 2021. doi: 10.22323/1.358.0753.

[44] Bryan Kim, Ari Brill, Tjark Miener, et al. DL1-Data-Handler: DL1 HDF5 writer, reader, and processor for IACT data, January 2023. URL `https://doi.org/10.5281/zenodo.7544496`.

[45] François Chollet et al. Keras. `https://keras.io`, 2015.

[46] Martín Abadi, Ashish Agarwal, Paul Barham, et al. TensorFlow: Large-scale machine learning on heterogeneous systems, 2015. URL `https://www.tensorflow.org/`. Software available from tensorflow.org.

[47] Diederik P. Kingma and Jimmy Ba. Adam: A Method for Stochastic Optimization. *arXiv e-prints*, art. arXiv:1412.6980, December 2014. doi: 10.48550/arXiv.1412.6980.

6. Summary and conclusions

During the last three decades, the first and second generations of Imaging Atmospheric Cherenkov Telescopes (IACTs), such as Whipple Observatory, VERITAS, HESS and MAGIC, have provided measurements of several TeV gamma-ray sources. Experiments like the Cherenkov Telescope Array (CTA) will be the next-generation IACTs in the southern and northern hemispheres, offering better sensitivity, angular resolution, and larger collection area than the current generation. One of the CTA's aims is to make significant progress in detecting high-energy cosmic rays, providing insight into cosmic ray propagation and acceleration. The work done in this thesis is twofold. The first part proposes two methods to measure a mass-sensitive parameter of nuclei-initiated air showers: the depth of the shower maximum X_{max}. The second part corresponds to the analysis of CTA simulations to separate iron-initiated from proton-initiated showers. This chapter will give a brief overview of all the results, ending with the conclusions of this thesis.

Novel methods for air shower detection using Cherenkov light

In **chapter 2**, we studied reconstructing an apparent shower maximum parameter to use as a mass-sensitive discriminator. The first step involved projecting the Cherenkov photons reaching the observation level into a plane containing the air shower, producing a bi-dimensional photon profile. The next part was to investigate whether different kinds of air showers would yield different results in the bi-dimensional profiles. The results showed a difference in the longitudinal development of gamma, proton and iron showers for lateral distances greater than 150 m with respect to the shower impact, which motivated the definition of a new observable called $X_{max}^{apparent}$, leading to the correlation with the depth of the shower maximum X_{max}. The new observable was used to reconstruct the value of the X_{max} by a fitting between them for each energy simulated. The results show that the X_{max} reconstruction quality is good enough compared to

other techniques and that the nuclei-initiated air shower classification is possible using an apparent shower maximum. This result was published in the peer-reviewed Astroparticle Physics Journal in January 2021.

In **chapter 3**, we explored the possibility of reconstructing the complete longitudinal shower profile using IACTs. We recall that the Cherenkov photons in air showers are produced mainly by relativistic electrons (and positrons) passing through the atmosphere. Therefore, the angular distribution of the Cherenkov light that reaches the ground results from a convolution between the particle's and the photon emission's angles. We exploited this characteristic to reconstruct the electron shower profile by using a parameterized function of the angular distribution for air Cherenkov photons given in the literature. Our method reconstructs the shower profile using all telescope detections simultaneously and adjusting the value of the X_{max} in an iterative process. In addition, the possibility of reconstructing the primary particle's energy was also investigated by using the maximum number of photons at X_{max}. For the first time, we have proposed a method to reconstruct the complete electron shower profile using all IACTs triggered. Moreover, these results showed open the possibility of cosmic ray measurements in terms of discrimination by the shower profile and the X_{max}. This result was published in the peer-reviewed Astroparticle Physics Journal in June 2023.

Iron-proton separation for air showers simulations with the Cherenkov Telescope Array

The analysis of cosmic ray measurements with full detector simulations from CTA software started in **Chapter 4**, where we discussed separating iron events from proton showers. First, it was shown that the shower profile and X_{max} reconstruction for CTA work by applying our proposed method in chapters 2 and 3. The selection criteria to improve this reconstruction was able to clean the noisy measurements significantly, making the final profile peaks sharper and, thus, easing the identification of the X_{max}. We tested our method using proton and iron simulations for Medium-Sized Telescope (MST) detections showing resolution values around ~ 35 g/cm^2 for both species in the energy range from 10 TeV to 300 TeV. The resolution and bias in the X_{max} reconstruction as a function of primary energy were also obtained. In addition, based on the distribution of the reconstructed shower maximum X_{max}^{rec}, a cut in the distribution to separate iron events from proton showers was proposed.

Chapter 5 addressed the challenge of making a binary classification of iron and proton events using deep learning algorithms. A convolutional neural network (CNN) was built, motivated by state-of-the-art image classification with neural networks. Initially, to accept only images as inputs, this CNN architecture was modified by adding two extra parameters as inputs: the depth of the shower maximum related to the primary mass and the primary energy related to the number of photons produced in the air shower. We used two image approaches: one from one telescope or all detections. The iron and proton efficiency was calculated for each input type and plotted as an energy function. The best performance for the binary classification was given in the scenario of inputs: image + X_{max} + energy. In this scenario, we achieved iron identification efficiency better than 90%.

Conclusion and outlook

In the following years, CTA will collect data, allowing us to probe different aspects of cosmic rays and air shower physics.

The analysis methods and pipeline produced in this thesis can be readily adjusted to studying the separation of cosmic-ray air showers. The significant flux of cosmic-ray nuclei detected by IACTs, 1000 times greater than gamma-ray events, can be used to reconstruct the X_{max} and identify nuclei of the primary in an air shower. The techniques developed here are general and can be applied to any nuclei-initiated shower. Studying the $X_{max}^{apparent}$ along the lateral distance for telescopes located at distances $\geqslant$ 150 m with respect to the shower impact provides an excellent starting point for a mass-sensitive parameter search. The second procedure of reconstructing the electron profile allows us to estimate the shower maximum and make a separation using a cut in its distribution. The third procedure is focused on using CNNs that include images plus mass-sensitive parameters as inputs. We recall that the iron efficiency corresponds to true events classified as iron events, and in contrast, proton efficiency corresponds to proton events miss-reconstructed as iron events. It was shown that by maximizing the separation between the iron (signal) and proton (background) efficiency curves, the input image plus X_{max} provided the best scenario with an iron efficiency better than 90% and a proton efficiency lower than 10%.

Keywords: Air Shower. Imaging Atmospheric Cherenkov Telescope. Shower Maximum. Convolutional Neural Network. Machine Learning.

7. Samenvatting en conclusies

In de afgelopen drie decennia hebben de eerste en tweede generatie Imaging Atmospheric Cherenkov Telescopes (IACT's), zoals Whipple Observatory, VERITAS, HESS en MAGIC, metingen gedaan aan verschillende TeV-gammastralingsbronnen. Experimenten zoals de Cherenkov Telescope Array (CTA) zullen de volgende generatie IACT's zijn op het zuidelijk en noordelijk halfrond, met een betere gevoeligheid, hoekresolutie en een groter verzamelgebied dan de huidige generatie. Een van de doelstellingen van de CTA is om aanzienlijke vooruitgang te boeken bij het detecteren van hoogenergetische kosmische straling, wat inzicht zal verschaffen in de voortplanting en versnelling van kosmische straling. Het onderzoekin dit proefschrift is tweeledig. Het eerste deel draagt twee methoden aan voor het meten van een massagevoelige parameter voordoor kernen veroorzaakte luchtbuien: de diepte van de bui, die maximaal Xmax is. Het tweede deel gaat over de analyse van CTA-simulaties om buien te onderscheiden die door ijzer danwel protonen veroorzaakt zijn. Dit hoofdstuk geeft een kort overzicht van alle resultaten en eindigt met de conclusies van dit proefschrift.

Nieuwe methoden voor detectie van luchtbuien met Cherenkov licht

In **Hoofdstuk 2** hebben we de reconstructie van een parameter voor het schijnbare maximum van een een bui bestudeerd om deze te gebruiken als massagevoelige onderscheidingsparameter. De eerste stap bestond uit het projecteren van de gedetecteerde Cherenkov-fotonen die het observatieniveau bereikten op een vlak met daarin de luchtbui, waardoor een tweedimensionaal fotonenprofiel ontstond. Het volgende deel was om te onderzoeken of verschillende soorten luchtbuien verschillende resultaten zouden opleveren in de tweedimensionale profielen. De resultaten toonden een verschil aan in de longitudinale ontwikkeling van gamma-, protonen- en ijzerbuien voor laterale afstanden groter dan 150 m met betrekking tot de impact van de buidouche. Dit motiveerde de definitie van een nieuwe

waarneembare parameter genaamd Xmax-app, wat leidde tot de correlatie met de diepte van de douche maximaal Xmax. De nieuwe waarneembare parameter werd gebruikt om de waarde van Xmax te reconstrueren door voor elke gesimuleerde energie tussen de twee te fitten. De resultaten laten zien dat de Xmax-reconstructiekwaliteit afdoende is vergeleken met andere technieken en dat door kernen veroorzaakte luchtbuiclassificatie mogelijk is met behulp van een schijnbaar buimaximum. Dit resultaat werd in januari 2021 gepubliceerd in het peer-reviewed Astroarticle Physics Journal.

In **Hoofdstuk 3** hebben we mogelijkhedenonderzocht om het volledige longitudinale buienprofiel te reconstrueren met behulp van IACT's, zelfs op een grotere afstand dan 150 m van het inslagpunt van de bui. We herinneren de lezer eraandat de Cherenkov-fotonen in luchtbuien voornamelijk worden geproduceerd door relativistische elektronen (en positronen) die door de atmosfeer heen bewegen. Daarom is de hoekverdeling van het Cherenkov-licht dat de grond bereikt het gevolg van een convolutie tussen de emissiehoeken van het deeltje en het foton. We hebben deze eigenschap benut om het elektronenbuienprofiel te reconstrueren door gebruik te maken van een geparametriseerde functie van de hoekverdeling voor lucht-Cherenkov-fotonen uit de literatuur. Onze methode reconstrueert het buienprofiel door alle telescoopdetecties tegelijkertijd te gebruiken en de waarde van de Xmax iteratief aan te passen. Daarnaast werd ook de mogelijkheid onderzocht om de energie van het primaire deeltje te reconstrueren door het maximale aantal fotonen bij Xmax te gebruiken. We hebben de eerste methode voorgesteld om het volledige elektronenbuienprofiel te reconstrueren met behulp van alle getriggerde IACT's. Bovendien toonden deze resultaten de mogelijkheid tot kosmische stralingsmetingen in termen van onderscheid door het buienprofiel en Xmax. Dit resultaat werd in juni 2023 gepubliceerd in het peer-reviewed Astroparticle Physics Journal.

IJzer-protonscheiding voor simulaties van luchtbuien met de Cherenkov Telescope Array

De analyse van kosmische stralingsmetingen met volledige detectorsimulaties van CTA-software begon in **hoofdstuk 4**, waar we het onderscheiden van ijzergebeurtenissen en protonenbuien bespraken. Ten eerste werd aangetoond dat de buienprofiel-reconstructie en de Xmax-reconstructie voor CTA werken door het toepassen van de door ons voorgestelde methode, die werd besproken in de hoofdstukken 2 en 3. De selectiecriteria

om deze reconstructie te verbeteren waren in staat om de ruis in de metingen aanzienlijk op te schonen, waardoor de uiteindelijke profielpieken scherper werden en dus de identificatie van Xmax werd vergemakkelijkt. We hebben onze methode getest met behulp van proton- en ijzersimulaties voor detecties met middelgrote telescoop (MST), en deze lieten resolutiewaarden rond ~ 35 g/cm^2 voor beide soorten zien in het energiebereik van 10 TeV tot 300 TeV. De resolutie en bias in de Xmax-reconstructie als functie van de primaire energie werden ook verkregen. Bovendien werd op basis van de distributievan het gereconstrueerde buienmaximum $X_{\mathrm{max}}^{\mathrm{rec}}$ een splitsing van de distributievoorgesteld om ijzergebeurtenissen te scheiden van protonenbuien.

Hoofdstuk 5 ging in op de uitdaging van het maken van een binaire classificatie van ijzer- en protongebeurtenissen met behulp van deep learning-algoritmen. Er werd een convolutioneel neuraal netwerk (CNN) gebouwd, gemotiveerd door de modernste beeldclassificatie-technieken met neurale netwerken. Aanvankelijk, zodat alleen beelden als invoer werden geaccepteerd, werd deze CNN-architectuur aangepast door twee extra parameters als invoer toe te voegen: de diepte van het maximum van de bui gerelateerd aan de primaire massa en de primaire energie gerelateerd aan het aantal fotonen geproduceerd in de luchtbui. We gebruikten twee beeld-benaderingen: één van één telescoop of alle detecties. Voor elk type invoer werd de ijzer- en protonefficiëntie berekend en geplot als een functie van energie. De beste prestatie voor de binaire classificatie werd bereikt met de invoercombinatie bestaande uit een afbeelding, Xmax waarde en energie. In dit scenario bereikten we een ijzeridentificatie-efficiëntie van meer dan 90%.

Conclusie en vooruitzichten

In de komende jaren zal CTA gegevens verzamelen waarmee we verschillende aspecten van de fysica van kosmische straling en luchtbuien kunnen onderzoeken. De analysemethoden en pipelinedie in dit proefschrift zijn geproduceerd kunnen gemakkelijk worden aangepast om de scheiding van kosmische-straling luchtbuien te bestuderen. De aanzienlijke stroom kosmische stralingskernen die door IACT's wordt gedetecteerd, 1000 keer meerdan het aantal gammastralingsgebeurtenissen, kan worden gebruikt om de Xmax te reconstrueren en om de kernen van de primaire kernen in een luchtbui te identificeren. De hier ontwikkelde technieken zijn algemeen en kunnen worden toegepast op elke door kernen geïnitieerde buie. Het bestuderen van de $X_{\mathrm{max}}^{\mathrm{apparent}}$ langs de laterale afstand voor

telescopen die op afstanden $>$ 150 m ten opzichte van de inslag van de buistaan, biedt een uitstekend startpunt voor een massagevoelige parameterzoektocht. De tweede procedure voor het reconstrueren van het elektronenprofiel stelt ons in staat het maximum van de buiin te schatten en een scheiding te maken door een splitsingin de distributieervan te maken. De derde procedure is gericht op het gebruik van CNN's die afbeeldingen plus massagevoelige parameters als invoer bevatten. We wijzen eropdat de ijzerefficiëntie overeenkomt met echte gebeurtenissen die zijn geclassificeerd als ijzergebeurtenissen, en dat de protonefficiëntie daarentegen overeenkomt met protongebeurtenissen die verkeerd zijn gereconstrueerd als ijzergebeurtenissen. Er werd aangetoond dat, door het maximaliseren van de scheiding tussen de ijzer- en protonefficiëntiecurven, een invoer bestaande uit de afbeelding, Xmax en energie de beste prestatie opleverde met een ijzer(signaal)efficiëntie beter dan 90% en een proton(achtergrond)efficiëntie lager dan 10%.

Trefwoorden: Luchtbuien. Imaging Atmospheric Cherenkov Telescoop. Diepte van de Douche Maximaal. Convolutioneel Neuraal Netwerk. Machine Learning.

8. Resumo e conclusões

Nas últimas três décadas, as gerações de Imaging Atmospheric Cherenkov Telescopes (IACTs), como o Observatório Whipple, VERITAS, HESS e MAGIC, têm fornecido medições de diversas fontes de raios gama de TeV. Experimentos como o Cherenkov Telescope Array (CTA) terão IACTs de próxima geração nos hemisférios sul e norte, oferecendo melhor sensibilidade, resolução angular e uma área de coleta maior do que a geração atual. Um dos objetivos do CTA é fazer avanços significativos na detecção de raios cósmicos de alta energia, fornecendo informações sobre a propagação e aceleração desses raios cósmicos. O trabalho realizado nesta tese foi dividido em duas partes. A primeira parte propõe dois métodos para medir um parâmetro sensível à massa dos núcleos que iniciam os chuveiros atmosféricos: a profundidade de máximo do chuveiro X_{max}. A segunda parte corresponde à análise de simulações do CTA para separar chuveiros iniciados por ferro de chuveiros iniciados por prótons. Este capítulo fornecerá uma breve visão geral de todos os resultados, encerrando com as conclusões desta tese.

Novos métodos para detecção de chuveiros atmosféricos usando luz Cherenkov

No **capítulo 2**, estudamos a reconstrução de um parâmetro aparente do máximo do chuveiro para usar como um discriminador sensível à massa. O primeiro passo envolveu a projeção dos fótons Cherenkov que alcançam o nível de observação em um plano contendo o chuveiro atmosférico, o que fornece um perfil bidimensional de fótons. A próxima parte foi investigar se diferentes tipos de chuveiros atmosféricos resultariam em diferentes perfis bidimensionais. Os resultados mostraram uma diferença no desenvolvimento longitudinal de chuveiros gama, próton e ferro para distâncias laterais maiores que 150 m em relação ao impacto do chuveiro, o que motivou a definição de um novo observável chamado $X_{max}^{apparent}$, correlacionando-o com a profundidade do máximo do chuveiro X_{max}. O novo observável foi usado para reconstruir o valor do X_{max} por meio de

um ajuste linear para cada energia simulada. Os resultados mostram que a qualidade da reconstrução do X_{max} é suficientemente boa em comparação com outras técnicas, e a classificação de chuveiros atmosféricos iniciados por núcleos é possível usando um máximo aparente do chuveiro. Esse resultado foi publicado no Journal of Astroparticle Physics em janeiro de 2021.

No **capítulo 3**, exploramos a possibilidade de reconstruir o perfil longitudinal completo do chuveiro usando IACTs. Ressaltamos que os fótons de Cherenkov em chuveiros atmosféricos são produzidos principalmente por elétrons (e pósitrons) relativísticos que passam pela atmosfera. Portanto, a distribuição angular da luz de Cherenkov que atinge o solo resulta de uma convolução entre os ângulos de emissão da partícula e dos fótons. Exploramos essa característica para reconstruir o perfil do chuveiro de elétrons usando uma função parametrizada da distribuição angular para fótons Cherenkov atmosféricos encontrada na literatura. Nosso método reconstrói o perfil do chuveiro usando todas as detecções do telescópio simultaneamente e ajustando o valor do X_{max} em um processo iterativo. Além disso, investigou-se a possibilidade de reconstruir a energia da partícula primária usando o número máximo de fótons em X_{max}. Pela primeira vez, propusemos um método para reconstruir o perfil de elétrons do chuveiro usando todos os IACTs acionados. Além disso, esses resultados mostraram a possibilidade de medições de raios cósmicos em termos de discriminação pelo perfil do chuveiro e X_{max}. Esse resultado foi publicado no Journal of Astroparticle Physics em junho de 2023.

Separação ferro-próton para simulações de chuveiros atmosféricos com o Cherenkov Telescope Array

A análise de medições de raios cósmicos com simulações completas dos telescópios a partir do software CTA é feita no **Capítulo 4**, onde discutimos a separação entre chuveiros iniciados por prótons e núcleos de ferro. Primeiramente, mostrou-se que o perfil do chuveiro e a reconstrução do X_{max} para o CTA funcionam aplicando nosso método proposto nos capítulos 2 e 3. Os critérios de seleção para melhorar essa reconstrução foram capazes de limpar significativamente as medições ruidosas, tornando os picos finais do perfil mais nítidos e, assim, facilitando a identificação do X_{max}. Testamos nosso método usando simulações de prótons e núcleos de ferro para detecções do Medium-Sized Telescope (MST), mostrando valores de resolução em torno de ~ 35 g/cm^2 para ambas as espécies na

faixa de energia de 10 TeV a 300 TeV. A resolução e o viés na reconstrução do X_{max} em função da energia primária também foram obtidos. Além disso, com base na distribuição do X_{max}^{rec} reconstruído, foi proposto um corte na distribuição para separar eventos de ferro de chuveiros de prótons.

O **Capítulo 5** abordou o desafio de fazer uma classificação binária de eventos de ferro e próton usando algoritmos de aprendizado de máquina. Uma rede neural convolucional (CNN) foi construída, motivada pela classificação de imagens de ponta com redes neurais. A arquitetura de CNN foi modificada para aceitar imagens e parâmetros do chuveiro como entradas. Neste caso os dois parâmetros foram a profundidade do máximo do chuveiro relacionada à massa primária e a energia primária relacionada ao número de fótons produzidos no chuveiro atmosférico. Usamos dois modos de imagem: imagem formada por a detecção de um telescópio e imagem contendo todas as detecções dos telescópios acionados para o mesmo evento. A eficiência de identificação de ferro e próton foi calculada para cada tipo de entrada e plotada como uma função de energia. O melhor desempenho para a classificação binária foi dado no cenário de entradas: imagem + X_{max} + energia. Nesse cenário, alcançamos uma eficiência de identificação de ferro melhor que 90%.

Conclusão e Perspectivas

Nos próximos anos, o CTA irá coletar dados, permitindo-nos explorar diferentes aspectos dos raios cósmicos e da física dos chuveiros atmosféricos.

Os métodos de análise e o *pipeline* produzidos nesta tese podem ser facilmente ajustados para estudar a separação de chuveiros atmosféricos de raios cósmicos. O significativo fluxo de núcleos de raios cósmicos detectados por IACTs, mil vezes maior do que eventos de raios gama, pode ser usado para reconstruir o X_{max} e identificar núcleos primários em um chuveiro atmosférico. As técnicas desenvolvidas aqui são gerais e podem ser aplicadas a qualquer chuveiro iniciado por núcleos. Estudar o $X_{max}^{apparent}$ ao longo da distância lateral para telescópios localizados a distâncias $\geqslant$ 150 m em relação ao impacto do chuveiro fornece um excelente ponto de partida para uma busca sensível à massa. O segundo procedimento de reconstrução do perfil de elétrons nos permite estimar o máximo do chuveiro e realizar uma separação usando um corte em sua distribuição. O terceiro procedimento é focado no uso de CNNs que incluem imagens mais parâmetros sensíveis à massa como entradas. Ressaltamos que a eficiência de ferro corresponde a eventos verdadeiros classificados como eventos de ferro, e, em contraste, a eficiência de prótons corresponde a

eventos de prótons reconstruídos erroneamente como eventos de ferro. Foi demonstrado que maximizando a separação entre as curvas de eficiência de ferro (sinal) e próton (fundo), a combinação entre entrada de imagem com o X_{max} forneceu um cenário com uma eficiência de ferro superior a 90% e uma eficiência de prótons inferior a 10%.

Palavras-chave: Chuveiro Atmosférico. Imaging Atmospheric Cherenkov Telescope. Profundidade do Máximo do Chuveiro. Rede Neural Convolucional. Aprendizado de Máquina.

9. Acknowledgements

I want to thank everyone who made this possible. In the first place, my girlfriend **Michelle**, who was my right hand and always was there to make me feel better and give me the support I needed. In second place to my mom **Sonia** and father **Gabriel**, who always offered me unconditional help without any doubts. To my sister **Gabriela**, brother-in-law **Gene**, and nephews, **Gia** and **Gene Gabriel**, for always giving me their support.

I especially want to thank my advisors, **Vitor** and **Manuela**, for their critical input, contributions and patience. It wouldn't be possible to get here without their guidance. Especially to Vitor because he accepted me as a master's student and then as a PhD student. Thanks for the suggestions, advice, and corrections that helped me to become a better scientist over these years. Also, thank Manuela because she allowed me to stay in the Netherlands for one year and taught me to be a better researcher. Without her help, this work would not have been possible.

To **Luan**, who helped me with my work through fruitful talks and helped me become a better programmer. To **Jann**, for the inputs and suggestions about the last chapter of my thesis. I want to thank all the friends and researchers I made at the IFSC and Kapteyn during my studies and for their input and keen interest.

This study was financed in part by the Coordenação de Aperfeiçoamento de Pessoal de Nível Superior – Brasil (CAPES) – Finance Code 001. Therefore, I also want to thank CAPES, FAPESP Proc. 2021/01089-1, the University of Sao Paulo and the **Brazilian people** who financed my scholarship through taxes and offer foreign people the opportunity to study in their country. I would also like to thank the University of Groningen and the Kapteyn Institute for the opportunity of the double degree program.